On the ubiquity of movement

Document status and date:
Published: 01/01/2024

DOI:
10.26481/dis.20240305mo

Document Version:
Publisher's PDF, also known as Version of record

Please check the document version of this publication:

• A submitted manuscript is the version of the article upon submission and before peer-review. There can be important differences between the submitted version and the official published version of record. People interested in the research are advised to contact the author for the final version of the publication, or visit the DOI to the publisher's website.
• The final author version and the galley proof are versions of the publication after peer review.
• The final published version features the final layout of the paper including the volume, issue and page numbers.

Link to publication

Download date: 15 May. 2024

Doctoral thesis

ON THE UBIQUITY OF MOVEMENT

Maarten C. Ottenhoff

2024

ON THE UBIQUITY OF MOVEMENT
A decoding perspective on widespread motor-related neural activity.

THESIS

to obtain the degree of Doctor at Maastricht University,
on the authority of the Rector Magnificus, Prof.Dr. Pamela Habibović,
in accordance with the decision of the Board of Deans,
to be defended in public on
Tuesday 5 March 2024at 13:00hrs.

by

Maarten Christiaan Ottenhoff

Promotor
　Prof. Dr. Yasin Temel

Copromotores
　Dr. Christian Herff
　Dr. Pieter Kubben

Assessment Committee
　Prof. Dr. Werner Mess (Chair)
　Dr. Jennifer Collinger, University of Pittsburgh
　Dr. Mariska van Steensel, Utrecht University
　Prof. Dr. Peter de Weerd

Contents

1
Introduction

Ubiquity: presence everywhere or in many places especially simultaneously.

Nearly every choice you make eventually leads to a movement. If you want a cup of coffee in morning, you need to get up and brew one. Want to improve your health? Get up and go for a run. Have not seen a friend for a while? Grab your phone and call them. Maybe you happen to have a thesis deadline, then you need to start writing. Whatever it is, a motor action is required to act on your decision and without it, decisions will have little effect.

1.1 When movement becomes a challenge

Unfortunately, for some people, movement is or becomes a challenge. People with severe motor disabilities (e.g. tetraplegia), or progressive motor diseases (e.g. Amyotrophic Lateral Sclerosis, ALS) have (increasingly) limited options to perform action to interact and communicate with their surroundings. The most affected individuals are limited to just facial or eye movements, diagnosed as near locked-in syndrome. Or in worse cases, patients are in a complete locked-in state. In that case,

no voluntary movement is possible, while the patients' cognitive capacity is intact. Depending on the severity, patients have little options left to interact with their surroundings, forcing them to depend on their caregivers increasingly more.

In the Netherlands between 1998 and 2017, there is an average annual incidence of 2.64 per 100.000 person-years and a prevalence of 9.6 per 100.000 persons of motor neuron disease [1], an umbrella term for ALS, primary lateral sclerosis and progressive muscular atrophy. Additionally, in 2011, 415.000 people had a severe motor disability, which amounts to 2.5% of the Dutch population in that year [2]. Given the decreased options to interact, these people depend on their caregivers, family and friends to function in their daily life. This is a burden for both affected individual and the caregivers. Studies on life satisfaction after spinal cord injury identified pain and functional independence as main predictors for high life satisfaction [3]. Not only does motor disability pose a burden on the patients, it does so on the caregivers as well. Caregiving can negatively affect the life of the caregiver: it may lead to a higher risk of mortality, psychosomatic, depressive, or anxious symptoms, and an overall lower quality of life [4]. Important to note is that positive effects are being recognized as well, including a sense of fulfillment, accomplishment and self-esteem [4]. For spinal-cord injured patients, the main predictor of life satisfaction is access to the environment [5], when accounting for all other independent measures.

Increasing access to the environment and functional independence will improve the quality of life for both the patient and their (caregiving) surroundings. It is therefore essential to provide new and intuitive tools to this patient group to interact with the environment.

1.2 Building a bridge between intention and movement

The core problem in most of these motor diseases is that a physical dysfunction caused a broken link between intention and motor output. There are many personalized and practical solutions to bridge this gap. One example is the famous cosmologist Stephen Hawking, who was able
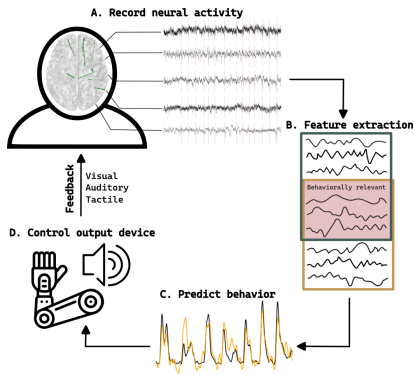
Figure 1.1: An overview of a basic closed-loop BCI pipeline. **A)** The user (attempts) to perform some behavior, such as (imagined) hand movement or speech. At the same time, neural data is continuously recorded from the user. **B)** From the recorded neural data, features are extracted that are related to the behavior. **C)** Using these features, the intended behavior of the user is continuously being predicted, which is then used to **D)** control an output device. This can be a robotic arm or a speaker to product speech. As an output is continuously being generated, the user receives direct feedback by observing or listening the generated output. The user can then adjust the strategy for the behavior, adapt to the system and learn how to increase control the BCI.

to control several communication devices, first with residual hand movements, followed by cheek muscles. Although it allowed him to communicate again, using the device was slow. The system used a switch to select from a library of 2500 to 3000 phrases, resulting in word rates of about one word per minute. Overall, many pragmatic and creative solutions exist that are very personalized. However, the residual movement determines the degrees of freedom of control. Moreover, in progressive diseases the residual movement might degrade, requiring new solutions over time.

To circumvent dependence on residual movement, the gap between intention and action can be bridged by directly recording neural activity and translating it into a control signal for an assistive device (Figure 1.1). This direct strategy removes the need for a secondary control signals. In the example above, a mapping needs to be learned from an existing behavior to the control output, i.e. hand or cheek movement, to control a switch of the speech computer. Although effective for the situation, the mapping from speech intention to cheek movement to word selection to audio output is much less intuitive than translating the intention to speak into audible speech directly. Strategies that are able to perform a direct translation from intention to output may provide the most natural solution to restoring part of the users' functional independence.

While the idea is simple, the execution is not. Defining and capturing

'intention' with sufficient spatial and temporal resolution is an ongoing challenge. Many different so-called neural decoders or brain-computer interfaces (BCIs) exist, targeting restoration or support of different functions. These include spelling computers [6], speech decoding [7–9], pain [10], decision-making decoders [11], neuropsychiatric state decoders [12–14], visual decoder [15] and motor decoders [16–18]. The latter, motor decoders can control a variety of devices, including devices like (motorized) wheelchairs, mouse pointers for click-and-select or robotic arms restoring a reach and grasp function.

1.3 Capturing motor-related neural activity

A fundamental requirement to translate neural activity into movement is to capture the right signal. The main target to record neural activity for motor decoding is the primary motor cortex. Anatomically, the primary motor cortex has direct descending pathways to the spinal cord [19], locating it relatively close to the downstream output. The anterior gyrus of the central sulcus has therefore been of great interest for motor related research since Penfield and Boldrey described the Homunculus in 1937 [20]. The Homunculus is a famous representation of a segregated map of the human body within the motor cortex, although it has undergone some updates recently [21, 22]. One well-known kinematic encoded within spiking activity recorded in the motor cortex is direction. Georgopoulos et al. discovered that a weighted sum of the firing of populations of neurons encoded the direction of movement. Each neuron is variably tuned towards a preferred direction in 2D [23] and 3D [24]. This representation is called directional tuning, and led to early demonstrations of 3D robot arm control in primates [25]. The signal was sufficient to achieve 8 degrees of freedom in an executed and imagined 3D center out paradigm. In humans, the first demonstration showed cursor control with 4 degrees of freedom using an imagined movement paradigm [26]. Since then, multiple high-performing decoders have been presented that successfully decode motor processes from the motor cortex [7, 16–18].

The motor cortex is clearly an essential brain area for motor control, but it is one component within a larger motor system. The importance

and ubiquity of movement in daily life may be reflected in the scale of involved brain areas; most neural processes may facilitate an eventual downstream motor output [27]. The motor cortex may not contain all behaviorally relevant neural information (e.g. higher order processes such as planning or sequencing movements), and many other brain areas contribute to unique outputs to the periphery as well [28]. To prevent hitting a performance ceiling in motor BCIs, the integration of multiple areas can increase the available information into a more complete representation, ultimately improving the performance of neural motor decoders.

However, to investigate high quality neural signals from other areas of the motor cortex, different recording methods are required. Particularly, stereotactic encephalography (sEEG) electrodes provide a unique opportunity on distributed and brain-wide recordings [29].

1.4 Stereotactic encephalography electrodes for motor brain-computer interfaces

SEEG electrode are long, rod-like electrodes used to record electrophysiological neural activity, and are commonly implanted during the treatment of medication-resistant epilepsy. Because medication has not been effective to reduce seizures and increase quality of life sufficiently, the patients are treated by resecting or lesioning the onset zone of the epilepsy seizures. To determine the location of the onset zone, the patients are implanted with multiple sEEG electrodes (Figure 1.2a). Each electrode is inserted in the brain through a small burr hole and penetrates deep into the brain (Figure 1.2b). Then, the patients undergo a monitoring period of two to three weeks in a specialized clinical center, where they are constantly observed for seizures. Once the patient had enough seizures to determine the onset zone, the electrodes are explanted. If the onset zone does not overlap with eloquent cortex and it is safe enough, the zone is resected of lesioned.

The unique aspect of sEEG electrodes is that they provide a sparse brain-wide coverage. The combined locations of multiple electrodes configurations cover nearly the complete brain (Figure 1.1a and Figure 1.3) Each electrode is a cylindrical shaft with 8 to 18 contacts. Each contact

Figure 1.2: General overview of sEEG implantation. **A**) Planning of implantation trajectories. **B**) Electrodes are implanted using stereotactic frame through small burr holes. *Adapted from [29] with permission.* **C**) After surgery, the patients stay in a monitoring center for 2 to 3 weeks. This period defines the recording window for BCI and other neuroscientific experiments. Patients are not confined to their bed and can freely move around within the center. The image is an example of one participant performing one of our experiments. The experiment is shown on screen, and neural data is streamed in real-time from the amplifier to the laptop via the yellow cable.

can record neural data, 2mm in length and 1mm in diameter, resulting in a surface areas of 6.3mm^2. The contacts have an inter-contact distance of 1.5 to 3.5mm. For clarity on the nomenclature throughout this thesis: the electrodes are the full rods implanted, and each electrode has several contacts, the physical location where neural activity is recorded. Once recorded and digitized, they are referred to as channels. The small size of each contact and the placement directly into the neural tissue gives sEEG a high spatial resolution. Additionally, the electrophysiological signal recorded has a high temporal resolution as well, providing access to high frequency components like high-gamma ($> 70Hz$). The long electrodes penetrate into deep brain areas and provide access to subcortical structures that are otherwise hard to reach with other electrophysiological recording methods. The millivoltage recorded on each electrodes measures the local field potential (LFP), which is an aggregation of electrical activity in the extracellular space. Compared with the fast action potentials, the LFP reflects a slower accumulation of many different sources and many different neurons close to the contact. Buzsáki et al. (2012) [30] identified up to 10 different contributors to the extracellular voltage, of which the synchrony of current sources and the cellular-synaptic architectural organization of the network are the most promi-

nent contributors. As the LFP is an aggregation of all these sources, it is impossible to disentangle them into separate sources. Nonetheless, the major component is synchronized firing, which is a reliable measure of neuronal activity that can be related to behavior.

As mentioned, sEEG electrodes are implanted in epilepsy patients who undergo a presurgical monitoring period. This monitoring period provides a recording window for all types of (neuroscientific) research. The implantation trajectories are solely determined by the clinical need of the patient, and therefore vary drastically person-to-person. Nonetheless, the unique sparse, brain-wide coverage of both cortical and subcortical structures provides an excellent research vehicle for a variety of decoding studies. For example, in our lab we have a variety of decoding studies, including speech synthesis [9], decision-making [31], and navigation [32].

In the context of motor decoding, sEEG enables investigation of brainwide motor-related activity, as the combined coverage of multiple participants includes the whole brain (Figure 1.3). To this end, many areas have been identified by decoding studies to be involved in motor behavior, including the ventral premotor cortex [33], somatosensory cortex [34], posterior parietal cortex [35–37], supramarginal gyrus [34, 36, 38], fusiform and middle temporal gyrus [39], hippocampus [36, 39] and insula [36, 38]. Moreover, the basal ganglia constitute a subcortical system that is essential for motor control. Pathologies involving the basal ganglia [40], such as Parkinson's Disease (PD), severely limit the patients ability to move. Treatments like deep brain stimulation show great improvement in motor behavior, emphasizing the essential role of areas outside of the motor cortex in motor control.

As a matter of fact, studies using large scale neuropixel recordings report that areas in nearly the whole brain of zebra-fish [41] and mice [42–45] correlate with movement. The international brain lab consortium even report "Neural responses correlated with motor action almost everywhere in the brain." [27]. The major focus of the motor decoding field has been on the motor cortex, but this contemporary perspective of global distributed activity leaves valuable opportunities to uncover behaviorally relevant neural information for future motor decoders.

Figure 1.3: Anatomical locations covered by the electrode configurations of 16 participants (from chapter 5). The bar graph insets at the bottom of the figure show the contacts labeled as white matter or unknown. Note that most of the electrodes are in these areas. The brain insets show the corresponding electrode configurations warped onto an average brain.

1.5 Finding the hidden neural structure

Using sEEG as recording modality comes with a few challenges as well. First, the different electrode configurations per participant limit consistent coverage of a most brain areas (Figure 1.3), making it harder to draw conclusions across participants. Secondly, different types of tissues are sampled simultaneously. Both grey and white matter contain behaviorally relevant information [46, 47], but at different signal strengths. Finally, all contacts contain a different ratio of behaviorally relevant and behaviorally irrelevant neural activity, and noise. On the other hand, the sparse but brain-wide coverage might sample similar large-scale networks at different locations. In order to find the common structure among the different sources of neural information, we may look at the relationship between sources instead of the activity itself. One example where this is effective is the earlier mentioned directional tuning in the motor cortex [23]: While the single neurons in the population are variably tuned to direction, the linear relationship within the neural population describes a reliable population vector (i.e. a stable representation) of the direction of movement. Although multi-unit recordings are not directly comparable with the sEEG recordings here, the idea is applicable in both. The question then is how do we extract these neural relationships?

For this purpose, dimensionality reduction or manifold learning techniques may be excellent tools to extract hidden neural structures [48, 49]. The underlying premise it that the neural data in each recorded location contains a mix of behaviorally relevant activity, behaviorally irrelevant activity and noise. These techniques transform the neural data into a lower-dimensional representation, constructed by a (non-)linear combination of the neural activity in each contact. Hence, it captures the relationship of neural activity between contacts. These neural dynamics exhibit more predictable trajectories within the lower-dimensional representation [50]. Regularly used methods to extract a low-dimensional representation are principal component analysis or canonical correlation analysis. Dimensionality reduction techniques apply a transformation that maximized a metric. In the case of principal component analysis,

the axes are rotated as such that the axes, or principal components, are ordered by explained variance. In essence, the transformation combines the neural information in each channel related to the same variance into one or more principal components, whereas the unrelated variance and noise are excluded.

These manifold or neural dynamics approaches appear to be effective methods to extract hidden neural patterns with predictable trajectories of multiple behaviors [51–53]. For example, Natraj et al. (2021) [52] show a stable multi-area manifold capturing all movements, where more specific movements (e.g. finger flexion or pinching) are represented as sub-manifolds within this manifold. Manifold studies have in common that they extract a manifold based on the relationship between all recorded neurons (or in our case, contacts), and demonstrate that different behaviors exhibit predictable trajectories on this manifold. However, most neural manifold studies so far are based on trial-based paradigms in monkeys with microelectrode arrays (MEAs) or humans with ECoG. Although these methods can be applied to any time series data, they have not been applied to the LFPs from sEEG. Given the distributed characteristics of electrode configurations in sEEG, these methods may be particularly effective to extract the underlying neural structure of brainwide activity, and apply it to brain-computer interface applications.

1.6 Problem statement and outline of this thesis

SEEG-based motor decoding has much under explored potential for BCI development. Thus, this thesis describes multiple research endeavors on both practical and theoretical aspects of motor decoding using sEEG. In chapter 2, we started by developing a simple decoder that continuously predicts left and right hand movements using linear discriminant analysis. We demonstrated that the decoder was able to do so using beta and high-gamma power. Based on this encouraging result, we wanted to look deeper into the predictive power of non-motor brain areas. In chapter 3, we trained a Riemannian decoder, while we specifically removed all contacts that were located in or around the central sulcus. A Riemannian decoder has been applied successfully in surface EEG, and makes predic-

tions based on trial and class covariance matrices. We demonstrate that our decoder was able to predict movement significantly above chance, regardless of electrode placement. Subsequently, in chapter 4, we were interested whether this brain-wide movement-related neural activity can be described by a low-dimensional representation. We show that there indeed exists a manifold that describes movement-related neural activity. This manifold remains stable under loss of channels, and is predictive across tasks and even across participants with non-overlapping electrodes configurations. The movement task used was a simple move/no-move task, raising the question whether movements that are more complex are represented as well. Therefore, we developed a gamified experiment that captured continuous 3D hand-movements, described in chapter 5, and evaluated a wide range of movement kinematics. We show that non-directional movement speed and acceleration are represented throughout the brain, while their directional counterparts did not seem to be represented. During the experiments described in these chapters, our lab grew with more colleagues and therefore more experiments. Initially, all experiments were set up and run manually, which was prone errors with many manual actions and different processes to keep track of. To handle the increased number of experiments, we had to simplify our experimental pipeline, reduce errors and increase time spent on recording instead up setup. Therefore, we developed a system called T-Rex that handles all processes and shows everything in a simple user interface. In chapter 6, we describe the system and development of T-Rex. T-Rex has simplified our recordings and is currently in use in multiple hospitals.

The attentive reader might have noticed that chapter 7 is not about motor decoding. As COVID-19 spread around the world, our daily lives were severely affected as well. Our own hospital was on the verge of having insufficient beds on the intensive care to house the large numbers of incoming severely affected COVID-19 patients. To aid hospital decision-making in the case that clinicians needed to choose whom to give a bed among the incoming patients (ominously called code black), I decided to redirect my time and resources to provide support where needed. With a large consortium of 11 different hospitals in the Netherlands, we developed an algorithm (chapter 7) that could aid the clinical

decision-making in case of a bed-shortage. While we were happy with the result, we were mostly happy that we never had to use the algorithm.

References

[1]   Adriaan D. de Jongh et al. "Incidence, Prevalence, and Geographical Clustering of Motor Neuron Disease in the Netherlands". en. In: *Neurology* 96.8 (Feb. 2021). Publisher: Wolters Kluwer Health, Inc. on behalf of the American Academy of Neurology Section: Article, e1227–e1236. DOI: 10.1212/WNL.0000000000011467.

[2]   M de Klerk et al. *Factsheet: Mensen met een lichamelijke of verstandelijke beperking*. Dutch. 2012.

[3]   Christel M. van Leeuwen et al. "Trajectories in the Course of Life Satisfaction After Spinal Cord Injury: Identification and Predictors". en. In: *Archives of Physical Medicine and Rehabilitation* 92.2 (Feb. 2011), pp. 207–213. DOI: 10.1016/j.apmr.2010.10.011.

[4]   Marie-Christine Rousseau et al. "Evaluation of quality of life in individuals with severe chronic motor disability: A major challenge". In: *Intractable & Rare Diseases Research* 5.2 (May 2016), pp. 83–89. DOI: 10.5582/irdr.2016.01017.

[5]   J. Scott Richards et al. "Access to the environment and life satisfaction after spinal cord injury". en. In: *Archives of Physical Medicine and Rehabilitation*. Spinal Cord Injury 80.11 (Nov. 1999), pp. 1501–1506. DOI: 10.1016/S0003-9993(99)90264-2.

[6]   Aya Rezeika et al. "Brain–Computer Interface Spellers: A Review". en. In: *Brain Sciences* 8.4 (Apr. 2018). Number: 4 Publisher: Multidisciplinary Digital Publishing Institute, p. 57. DOI: 10.3390/brainsci8040057.

[7]   Francis R. Willett et al. "A high-performance speech neuroprosthesis". en. In: *Nature* (Aug. 2023). Publisher: Nature Publishing Group, pp. 1–6. DOI: 10.1038/s41586-023-06377-x.

[8]   Sean L. Metzger et al. "A high-performance neuroprosthesis for speech decoding and avatar control". en. In: *Nature* (Aug. 2023). Publisher: Nature Publishing Group, pp. 1–10. DOI: 10.1038/s41586-023-06443-4.

[9]   Miguel Angrick et al. "Real-time synthesis of imagined speech processes from minimally invasive recordings of neural activity". en. In: *Communications Biology* 4.1 (Sept. 2021). Bandiera_abtest: a Cc_license_type: cc_by Cg_type: Nature Research Journals Number: 1 Primary_atype: Research Publisher: Nature Publishing Group Subject_term: Brain–machine interface;Neural decoding Subject_term_id: brain-machine-interface;neural-decoding, pp. 1–10. DOI: 10.1038/s42003-021-02578-0.

[10] Qiaosheng Zhang et al. "A prototype closed-loop brain–machine interface for the study and treatment of pain". en. In: *Nature Biomedical Engineering* 7.4 (Apr. 2023). Number: 4 Publisher: Nature Publishing Group, pp. 533–545. DOI: 10.1038/s41551-021-00736-7.

[11] Erin L. Rich and Jonathan D. Wallis. "Decoding subjective decisions from orbitofrontal cortex". en. In: *Nature Neuroscience* 19.7 (July 2016). Bandiera_abtest: a Cg_type: Nature Research Journals Number: 7 Primary_atype: Research Publisher: Nature Publishing Group Subject_term: Neural decoding;Reward Subject_term_id: neural-decoding;reward, pp. 973–980. DOI: 10.1038/nn.4320.

[12] Katherine W. Scangos et al. "Closed-loop neuromodulation in an individual with treatment-resistant depression". en. In: *Nature Medicine* (Oct. 2021). Bandiera_abtest: a Cg_type: Nature Research Journals Primary_atype: Research Publisher: Nature Publishing Group Subject_term: Depression;Limbic system;Predictive markers Subject_term_id: depression;limbic-system;predictive-markers, pp. 1–5. DOI: `10.1038/s41591-021-01480-w`.

[13] Maryam M. Shanechi. "Brain–machine interfaces from motor to mood". en. In: *Nature Neuroscience* 22.10 (Oct. 2019). Number: 10 Publisher: Nature Publishing Group, pp. 1554–1564. DOI: `10.1038/s41593-019-0488-y`.

[14] Omid G. Sani et al. "Mood variations decoded from multi-site intracranial human brain activity". eng. In: *Nature Biotechnology* 36.10 (Nov. 2018), pp. 954–961. DOI: `10.1038/nbt.4200`.

[15] Soroush Niketeghad and Nader Pouratian. "Brain Machine Interfaces for Vision Restoration: The Current State of Cortical Visual Prosthetics". In: *Neurotherapeutics* 16.1 (Jan. 2019), pp. 134–143. DOI: `10.1007/s13311-018-0660-1`.

[16] Francis R. Willett et al. "High-performance brain-to-text communication via handwriting". en. In: *Nature* 593.7858 (May 2021). Number: 7858 Publisher: Nature Publishing Group, pp. 249–254. DOI: `10.1038/s41586-021-03506-2`.

[17] Sharlene N. Flesher et al. "A brain-computer interface that evokes tactile sensations improves robotic arm control". In: *Science* 372.6544 (May 2021). Publisher: American Association for the Advancement of Science, pp. 831–836. DOI: `10.1126/science.abd0380`.

[18] Mariska J. Vansteensel et al. "Fully Implanted Brain–Computer Interface in a Locked-In Patient with ALS". In: *New England Journal of Medicine* 375.21 (Nov. 2016). Publisher: Massachusetts Medical Society _eprint: https://doi.org/10.1056/NEJMoa1608085, pp. 2060–2066. DOI: `10.1056/NEJMoa1608085`.

[19] Peter L. Strick, Richard P. Dum, and Jean-Alban Rathelot. "The Cortical Motor Areas and the Emergence of Motor Skills: A Neuroanatomical Perspective". eng. In: *Annual Review of Neuroscience* 44 (July 2021), pp. 425–447. DOI: `10.1146/annurev-neuro-070918-050216`.

[20] Wilder Penfield and Edwin Boldrey. "SOMATIC MOTOR AND SENSORY REPRESENTATION IN THE CEREBRAL CORTEX OF MAN AS STUDIED BY ELECTRICAL STIMULATION". en. In: *Brain* 60.4 (1937), pp. 389–443. DOI: `10.1093/brain/60.4.389`.

[21] Evan M. Gordon et al. "A somato-cognitive action network alternates with effector regions in motor cortex". en. In: *Nature* 617.7960 (May 2023). Number: 7960 Publisher: Nature Publishing Group, pp. 351–359. DOI: `10.1038/s41586-023-05964-2`.

[22] Francis R. Willett et al. "Hand Knob Area of Premotor Cortex Represents the Whole Body in a Compositional Way". en. In: *Cell* 181.2 (Apr. 2020), 396–409.e26. DOI: `10.1016/j.cell.2020.02.043`.

[23] A. P. Georgopoulos et al. "On the relations between the direction of two-dimensional arm movements and cell discharge in primate motor cortex". en. In: *Journal of Neuroscience* 2.11 (Nov. 1982). Publisher: Society for Neuroscience Section: Articles, pp. 1527–1537. DOI: `10.1523/JNEUROSCI.02-11-01527.1982`.

[24]   Apostolos P. Georgopoulos, Andrew B. Schwartz, and Ronald E. Kettner. "Neuronal Population Coding of Movement Direction". In: *Science* 233.4771 (Sept. 1986). Publisher: American Association for the Advancement of Science, pp. 1416–1419. DOI: 10.1126/science.3749885.

[25]   Dawn M. Taylor, Stephen I. Helms Tillery, and Andrew B. Schwartz. "Direct Cortical Control of 3D Neuroprosthetic Devices". In: *Science* 296.5574 (June 2002). Publisher: American Association for the Advancement of Science, pp. 1829–1832. DOI: 10.1126/science.1070291.

[26]   Leigh R. Hochberg et al. "Neuronal ensemble control of prosthetic devices by a human with tetraplegia". In: *Nature* 442.7099 (2006), pp. 164–171. DOI: 10.1038/nature04970.

[27]   International Brain Lab et al. *A Brain-Wide Map of Neural Activity during Complex Behaviour.* en. Pages: 2023.07.04.547681 Section: New Results. July 2023. DOI: 10.1101/2023.07.04.547681.

[28]   Juan A. Gallego, Tamar R. Makin, and Samuel D. McDougle. "Going beyond primary motor cortex to improve brain–computer interfaces". English. In: *Trends in Neurosciences* 45.3 (Mar. 2022). Publisher: Elsevier, pp. 176–183. DOI: 10.1016/j.tins.2021.12.006.

[29]   Christian Herff, Dean J. Krusienski, and Pieter Kubben. "The Potential of Stereotactic-EEG for Brain-Computer Interfaces: Current Progress and Future Directions". English. In: *Frontiers in Neuroscience* 14 (2020). Publisher: Frontiers. DOI: 10.3389/fnins.2020.00123.

[30]   György Buzsáki, Costas A. Anastassiou, and Christof Koch. "The origin of extracellular fields and currents-EEG, ECoG, LFP and spikes". In: *Nature Reviews Neuroscience* 13.6 (2012). Publisher: Nature Publishing Group, pp. 407–420. DOI: 10.1038/nrn3241.

[31]   Laura Marras et al. *Decoding Arbitrary and Informed Decisions from Intracranial Recordings in Humans.* en. Pages: 2023.06.01.543070 Section: New Results. June 2023. DOI: 10.1101/2023.06.01.543070.

[32]   Jeremy Saal et al. "Towards hippocampal navigation for brain–computer interfaces". en. In: *Scientific Reports* 13.1 (Aug. 2023). Number: 1 Publisher: Nature Publishing Group, p. 14021. DOI: 10.1038/s41598-023-40282-7.

[33]   Alexander P. Rockhill et al. "Stereo-EEG recordings extend known distributions of canonical movement-related oscillations". en. In: *Journal of Neural Engineering* 20.1 (Jan. 2023). Publisher: IOP Publishing, p. 016007. DOI: 10.1088/1741-2552/acae0a.

[34]   Sarah K. Wandelt et al. "Decoding grasp and speech signals from the cortical grasp circuit in a tetraplegic human". en. In: *Neuron* (Mar. 2022). DOI: 10.1016/j.neuron.2022.03.009.

[35]   Richard A. Andersen, Tyson Aflalo, and Spencer Kellis. "From thought to action: The brain–machine interface in posterior parietal cortex". In: *Proceedings of the National Academy of Sciences* 116.52 (Dec. 2019). Publisher: Proceedings of the National Academy of Sciences, pp. 26274–26279. DOI: 10.1073/pnas.1902276116.

[36]   Guangye Li et al. "Assessing differential representation of hand movements in multiple domains using stereo-electroencephalographic recordings". en. In: *NeuroImage* 250 (Apr. 2022), p. 118969. DOI: 10.1016/j.neuroimage.2022.118969.

[37]   Meng Wang et al. "Enhancing gesture decoding performance using signals from posterior parietal cortex: a stereo-electroencephalograhy (SEEG) study". en. In: *Journal of Neural Engineering* 17.4 (Sept. 2020). Publisher: IOP Publishing, p. 046043. DOI: `10.1088/1741-2552/ab9987`.

[38]   Macauley Smith Breault et al. "Neural Correlates of Internal States that Capture Movement Variability". In: *2019 41st Annual International Conference of the IEEE Engineering in Medicine and Biology Society (EMBC)*. ISSN: 1558-4615. July 2019, pp. 534–537. DOI: `10.1109/EMBC.2019.8856778`.

[39]   MacAuley Smith Breault et al. "Non-motor Brain Regions in Non-dominant Hemisphere Are Influential in Decoding Movement Speed". In: *Frontiers in Neuroscience* 13.JUL (July 2019), pp. 1–13. DOI: `10.3389/fnins.2019.00715`.

[40]   Gerry Leisman and Robert Melillo. "The basal ganglia: motor and cognitive relationships in a clinical neurobehavioral context". en. In: *Reviews in the Neurosciences* 24.1 (Feb. 2013). Publisher: De Gruyter, pp. 9–25. DOI: `10.1515/revneuro-2012-0067`.

[41]   Misha B. Ahrens et al. "Brain-wide neuronal dynamics during motor adaptation in zebrafish". en. In: *Nature* 485.7399 (May 2012). Number: 7399 Publisher: Nature Publishing Group, pp. 471–477. DOI: `10.1038/nature11057`.

[42]   Nicholas A. Steinmetz et al. "Distributed coding of choice, action and engagement across the mouse brain". en. In: *Nature* 576.7786 (Dec. 2019). Number: 7786 Publisher: Nature Publishing Group, pp. 266–273. DOI: `10.1038/s41586-019-1787-x`.

[43]   Carsen Stringer et al. "Spontaneous Behaviors Drive Multidimensional, Brain-wide Activity". In: *Science* 364.6437 (Apr. 2019), p. 255. DOI: `10.1126/science.aav7893`.

[44]   Peter Zatka-Haas et al. "Sensory coding and the causal impact of mouse cortex in a visual decision". In: *eLife* 10 (July 2021). Ed. by Martin Vinck, Joshua I Gold, and Karel Svoboda. Publisher: eLife Sciences Publications, Ltd, e63163. DOI: `10.7554/eLife.63163`.

[45]   Simon Musall et al. "Single-trial neural dynamics are dominated by richly varied movements". en. In: *Nature Neuroscience* 22.10 (Oct. 2019). Number: 10 Publisher: Nature Publishing Group, pp. 1677–1686. DOI: `10.1038/s41593-019-0502-4`.

[46]   Brian A. Murphy et al. "Contributions of subsurface cortical modulations to discrimination of executed and imagined grasp forces through stereoelectroencephalography". In: *PLoS ONE* 11.3 (2016), pp. 1–21. DOI: `10.1371/journal.pone.0150359`.

[47]   Chad Bouton et al. "Decoding Neural Activity in Sulcal and White Matter Areas of the Brain to Accurately Predict Individual Finger Movement and Tactile Stimuli of the Human Hand". In: *Frontiers in Neuroscience* 15 (2021).

[48]   Juan A. Gallego et al. "Neural Manifolds for the Control of Movement". en. In: *Neuron* 94.5 (June 2017), pp. 978–984. DOI: `10.1016/j.neuron.2017.05.025`.

[49]   Krishna V. Shenoy and Jonathan C. Kao. "Measurement, manipulation and modeling of brain-wide neural population dynamics". en. In: *Nature Communications* 12.1 (Jan. 2021). Number: 1 Publisher: Nature Publishing Group, p. 633. DOI: `10.1038/s41467-020-20371-1`.

[50]   Mark M. Churchland et al. "Neural population dynamics during reaching". en. In: *Nature* 487.7405 (July 2012). Bandiera_abtest: a Cg_type: Nature Research Journals Number: 7405 Primary_atype: Research Publisher: Nature Publishing Group Subject_term: Motor cortex;Neuronal physiology;Population dynamics Subject_term_id: motor-cortex;neuronal-physiology;population-dynamics, pp. 51–56. DOI: 10.1038/nature11129.

[51]   Juan A. Gallego et al. "Cortical population activity within a preserved neural manifold underlies multiple motor behaviors". en. In: *Nature Communications* 9.1 (Oct. 2018). Number: 1 Publisher: Nature Publishing Group, p. 4233. DOI: 10.1038/s41467-018-06560-z.

[52]   Nikhilesh Natraj et al. "Compartmentalized dynamics within a common multi-area mesoscale manifold represent a repertoire of human hand movements". en. In: *Neuron* (Oct. 2021). DOI: 10.1016/j.neuron.2021.10.002.

[53]   Mostafa Safaie et al. *Preserved neural population dynamics across animals performing similar behaviour*. en. Pages: 2022.09.26.509498 Section: New Results. Sept. 2022. DOI: 10.1101/2022.09.26.509498.
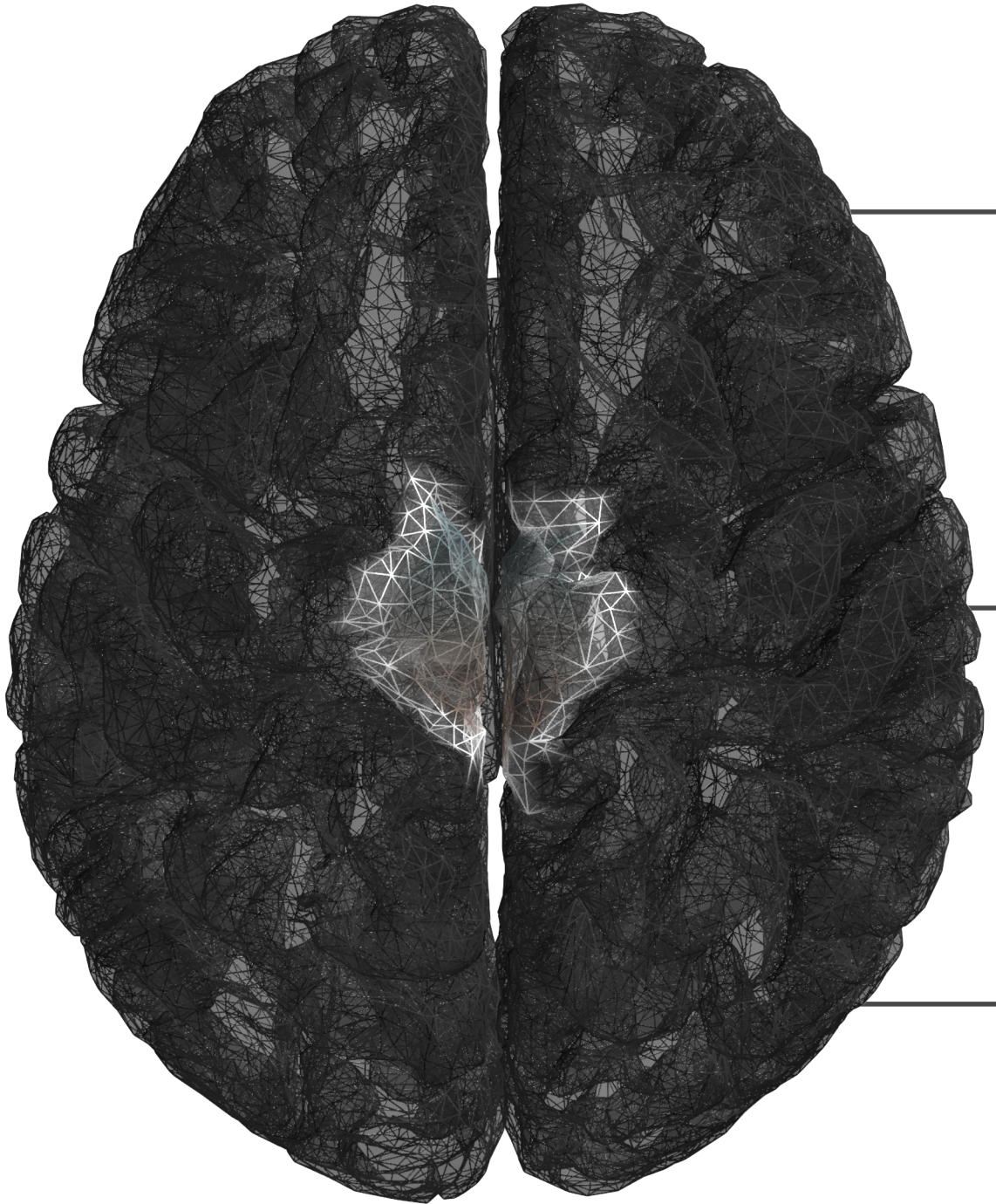
2

Continuously Decoding Grasping Movements using Stereotactic Depth Electrodes

2021

M.C. Ottenhoff, S. Goulis, L. Wagner, S. Tousseyn, A. Colon, P. Kubben and C. Herff

Abstract

Brain-Computer Interfaces (BCIs) that decode a patient's movement intention to control a prosthetic device could restore some independence to paralyzed patients. An important step on the road towards naturalistic prosthetic control is to decode movement continuously with low-latency. BCIs based on intracortical micro-arrays provide continuous control of robotic arms, but require a minor craniotomy. Surface recordings of neural activity using EEG have made great advances over the last years, but suffer from high noise levels and large intra-session variance. Here, we investigate the use of minimally invasive recordings using stereotactically implanted EEG (sEEG). These electrodes provide a sparse sampling across many brain regions. So far, promising decoding results have been presented using data measured from the subthalamic nucleus or trial-to-trial based methods using depth electrodes. In this work, we demonstrate that grasping movements can continuously be decoded using sEEG electrodes, as well. Beta and high-gamma activity was extracted from eight participants performing a grasping task. We demonstrate above chance level decoding of *movement vs rest* and *left vs right*, from both frequency bands with accuracies up to 0.94 AUC. The vastly different electrode locations between participants lead to large variability. In the future, we hope that sEEG recordings will provide additional information for the decoding process in neuroprostheses.

2.1 Introduction

Continuously decoding movement from neural signals is an important step towards naturalistic prosthetic control. Promising advances have been made using non-invasive electro-encephalographic (EEG) [1] or invasive cortical methods, e.g. microelectrode arrays [2]. However, brain-computer interfaces (BCIs) using stereotactic or sEEG electrodes, capturing neural activity from subcortical structures, are relatively unexplored, while holding potential to contribute to higher performing decoding algorithms [3]. These electrodes cover a wide variety of areas across the brain and provide access to harder to reach structures, such as the basal ganglia, insula or hippocampus. Additionally, the electrodes

provide simultaneous access to local high frequency oscillations in multiple areas, which could be used as control signal for BCIs. Exploiting these high frequency signals can decrease the decoder's response latency to the users' intended action, contributing to naturalistic prosthetic control. Additionally, activity from subcortical structures might uncover additional control signals for adaptive deep brain stimulation [4].

2.2 Background | Related Work

So far, several studies have presented decoding results using local field potentials (LFPs) measured with depth electrodes. All depth electrode implantations are based solely on clinical needs, which results in two main patient populations: Parkinson's disease (PD) patients with deep brain stimulation electrodes and medication-resistant epilepsy patients implanted for presurgical focus localization. The electrodes in PD patients cover the globus pallidus interna (GPi) and the subthalamic nucleus (STN), and thus decoding efforts utilize activity from these areas. Loukas and Brown [5] were able to predict the onset of voluntary hand movement with 95% sensitivity and 77% specificity on a trial-to-trial basis. Mamun et al. [6] improved on these results by showing $91.5 \pm 2.3\%$ accuracy on movement detection and $74.0 \pm 6.4\%$ accuracy on laterality detection, also on trial-to-trial basis and averaged over patients with STN and GPi electrodes. Further efforts on decoding movements using DBS electrodes aimed to decode gripping force from the STN [7, 8]. Recently, Shah et al. [9] decoded gripping force with a correlation up to 0.76 between decoded and actual gripping force, and were able to do so continuously.

Opposed to the specific and consistently targeted regions in PD patients, areas covered in epilepsy patients are spread throughout the brain, which makes comparisons between patients and studies significantly more complicated. Above chance gesture decoding has been demonstrated in several studies [10, 11]. Breault et al. [12] decoded movement speed with a correlation of 0.38 ± 0.03, and $70\% \pm 3\%$ when decoding three speed levels.

The studies discussed so far mostly utilize the beta frequency band

(12-30 Hz) and (high-)gamma band (30-55 and 55-90 Hz). Beta activity, especially in the STN, but also (sensori-)motor cortex, is decreased during movement. An increase in beta power is consequently associated with the inhibition of (imagined) movement [13, 14]. Gamma or high-gamma activity is considered to hold localized information of movement [15] and is known to increase during movement. Khawaldeh et al. [14] showed that high-gamma activity was predictive of intended contralateral and ipsilateral limb movements, supported by a decoding performance of 0.79 to 0.80 area under the receiver operator curve (AUC).

Up to now, most movement decoding efforts are targeting a trial-to-trial prediction. However, an important step towards naturally controlled closed-loop BCIs is to decode intention continuously. The work by Shah et al. [9] already showed promising results on continuous force decoding using STN activity, but it has not yet been demonstrated in other brain areas using depth electrodes. In this work, we demonstrate that it is possible to decode grasping movements continuously and detect laterality using sEEG electrodes. Due to the large variability in covered cortical and white matter regions in each patient, results varied drastically and highlight the importance of target selection.

2.3 Methods

Participants

Eight patients (mean age 39.5 ± 15.8, 4 male, 4 female) with medication-resistant epilepsy participated in our study, while being under presurgical assessment to identify epileptogenic zones. Written informed consent was provided by all participants, and all agreed to participate voluntarily during the monitoring period. The experiments were conducted under the supervision of experienced healthcare staff in a clinical environment, and were approved by the IRB of Maastricht University and Epilepsy Center Kempenhaeghe (METC 2018-0451).

Experimental paradigm

Participants were asked to execute opening and closing their left or right hand continuously when a 3-second instruction was shown on a screen.
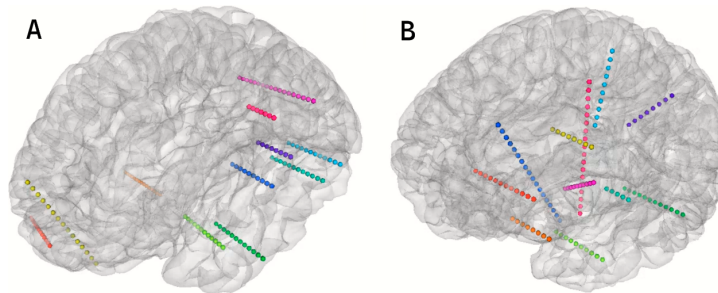
Figure 2.1: Electrode placements of two participants. Electrodes cover a wide variety of (sub-)cortical areas across both hemispheres.

There was a 3-second rest period in between trials. The task was repeated 30 times per hand in random order, resulting in a total of 60 trials.

Electrode Locations

Electrode locations were solely based on clinical needs. Co-registration of a pre-operative T1-weighted MRI and a post-operative CT scan were used to determine the electrode locations. FREESURFER [16] and `img_-pipe` [17] were used for both co-registration and anatomical labeling of the electrodes. A 3D view of the electrode placement of two of the participants is shown in Figure 2.1. The sparse coverage of many different brain regions, including temporal gyri, frontal gyri, hippocampus and amygdala (Figure 2.1a), provides a variety of cortical and white matter signals.

Data Acquisition

The implanted sEEG-electrodes (Microdeep intracerebral electrodes; Dixi Medical, Beçanson, France) had a diameter of 0.8mm and contained 5 to 18 contacts. Electrode contacts were 2mm long and the inter-contact distance was 1.5mm. The recordings were common ground referenced. Neural data were acquired at 1024 Hz using a 128-channel Micromed SD LTM amplifier (Micromed S.p.A, Treviso, Italy). Incoming data were synchronized to the experimental timings using LabStreamingLayer [18].

Signal Processing

Data were first detrended and high-pass filtered using a finite impulse response filter with a cutoff frequency of 0.5 Hz. Then, beta or high-gamma activity were extracted by applying two band pass infinite impulse response filters (12 - 30 Hz for beta and 55 - 90 Hz for high-gamma) and a notch filter of 48 - 52 Hz to attenuate line noise of 50 Hz. Next, the envelop of the frequency bands was calculated by applying a Hilbert transform. The resulting signal was windowed using 1s windows with 100ms frame shift and the average was calculated for each window. These windowing settings were considered to include enough data to capture the neural dynamics reliably, while also facilitating a low-latency prediction. The same windowing algorithm was applied to the trial labels, but the mode was used as aggregation method. The resulting matrix was of form $[NWindows \times Nchannels]$. All analyses are implemented using Python 3.7.5, filters were applied using the MNE package (v0.21.0) [19]. The learning algorithms described in the next section were implemented using Sci-kit learn (v0.22) [20]. Source code is available at `github.com` `/mottenhoff/continuous-grasp-decoding`.

Model Development & Validation

A linear discriminant analysis (LDA) classifier using singular value decomposition as solver was trained and validated on either beta or high-gamma band activity from all channels. The LDA was fitted on a 3-class problem (rest, left hand movement and right hand movement) using 10-fold non-shuffled cross-validation. Performance was evaluated by calculating the average area under the receiver operator curve (AUC) over all folds. The label distribution in the data was 900 left hand, 900 right hand and 1800 rest labels.

Results

Both beta and high-gamma-based models performed well above chance in most participants. Figure 2.2 shows the results per participant and frequency band. Chance level is 0.5. In move vs rest predictions, the trained models reached a performance of up to 0.80 AUC (0.77 to 0.83;
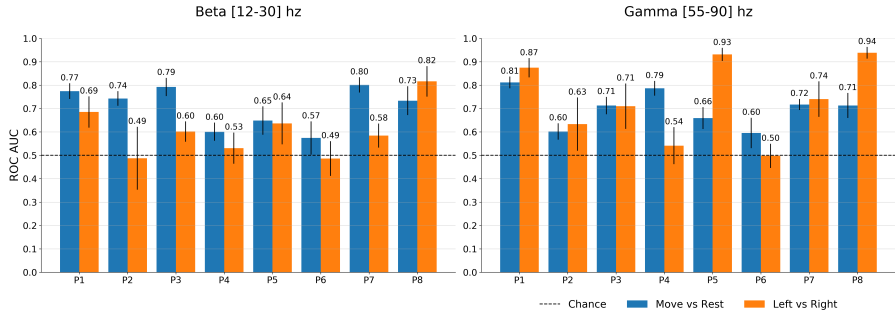
Figure 2.2: Overall results of LDA models trained on beta and high-gamma. High performance is seen in both models, notably in laterality detection using high-gamma activity. However, there is large variability between and within participants. *ROC AUC: Area under the receiver operator curve*

95% confidence interval) when trained on beta activity and 0.81 (0.79 to 0.84) using high-gamma activity. When considering laterality detection, the maximum performance was comparable to grasping movement detection with an AUC of 0.82 (0.75 to 0.88) using beta activity. The maximum performance of the high-gamma models predicting laterality was excellent with 0.94 (0.91 to 0.96) AUC. However, the results show high variation in performance between and within participants. For example, models trained on $P2_{gamma}$, $P4_{beta}$ and P6 only reached an AUC at chance level or slightly above for all comparisons, whereas $P5_{gamma}$ shows excellent performance on laterality discrimination (0.93, 0.90 to 0.96) but performance just above chance level on detecting movement vs rest (0.66, 0.62 to 0.70).

2.4 Discussion

We showed that LFP measured with sEEG electrodes contain enough information to accurately decode grasping movements and movement laterality in a continuous way. We improved on previous work that decoded on a trial-to-trial basis using sEEG electrodes [10, 11], and put a step forward towards closed-loop movement decoding systems from depth electrodes. Additionally, we expand on the results of Shah et al. [9],

by showing that accurate movement predictions can also be made from a sparse brain-wide coverage of the brain using depth electrodes.

However, our results show high variability in performance within and between participants, which we attribute to the wide variety of covered brain areas. It is plausible that the low performing models simply did not have access to the areas encoding movement related activity. Moreover, if one only considers the high performing models, it remains challenging to identify informative areas. Based on fMRI studies in (non-)human primates and humans, reach and grasp related neural activity is seen in dorso-medial and dorso-lateral pathways between the parietal cortex and fronto-medial areas [21]. However, within the many covered areas, only few overlap and there is too few data to identify systematically involved areas; electrodes of the eight included participants cover > 50 areas with > 600 contacts. Note that bilateral locations are aggregated as single unique area and that the labels are based on the definitions by the FREESURFER software. Additionally, a significant proportion of these contacts are located in white matter ($n = 270$) or unknown areas ($n = 69$). Unknown areas were labeled as such because they could not be defined during anatomical labeling. Both white matter and unknown areas are included in the models, as they could hold important information. However, interpretation of white matter signals is an unsolved challenge and requires an in-depth multi-site analysis [22]. Initial investigations into the identification of important areas showed highly variable results and indicated that a more in-depth analysis was required, which was outside the scope of this work.

Both the beta and high-gamma envelopes were extracted, as both frequencies are identified to modulate movement [13, 15] and successfully implemented in decoding models [9]. Our results strengthen these findings as both the beta and high-gamma model perform well above chance, where the highest performance was seen using high-gamma activity. However, the high-gamma models also show larger variability in performance, which might be caused by the higher spatial localization of high-gamma. High-gamma spreads less far in a volume than the lower beta frequency, thus making it less likely that the relevant signal is captured from a specific area. Despite this, our results indicate that in

the current implementation, the high-gamma local field potential holds enough information to achieve excellent performance. Many other frequencies, such as alpha or theta, might also be important, especially in areas within the broad coverage of sEEG electrodes. We did not include more frequency bands, as it would increase the complexity of the models and potentially decrease the reliability of the models. Even within the included frequency bands, the information that the oscillation encodes may differ per area. One example is that beta activity in STN is suggested to suppress the basal ganglia to encode relevant information of intended actions [14], while beta activity in the sensorimotor cortex is associated with movement planning and response errors [23]. In this work, we chose the same frequencies as used in Shah et al. [9] to increase comparability. With carefully implemented machine learning approaches to avoid overfitting, it is not necessarily required to know what information the signal encodes. However, to improve BCI reliability, especially in the varying coverage of sEEG electrodes, it is important to be able to identify which specific areas are used in the decoding models. In short-term, this can guide experimental paradigms based on the implanted locations, and in the long-term, it can increase performance and reliability between participants and experiments.

Limitations
Participants suffering from epilepsy performed the experiments. It is unknown if and how the signal is modulated by epilepsy. Furthermore, the used experimental design did not allow for investigation of additional promising factors such as speed.

2.5 Conclusion

In conclusion, we show that movement related activity can be decoded continuously using sEEG electrodes in various brain areas with excellent performance in some participants. However, the sparse covering of the brain also results in large variability in performance within and between participants. The current work is a next step towards naturally controlled

BCIs, but future research should focus on identification of important areas covered by sEEG electrodes.

References

[1] B. J. Edelman et al. "Noninvasive neuroimaging enhances continuous neural tracking for robotic device control". In: *Science Robotics* 4.31 (2019). DOI: `10.1126/scirobotics.aaw6844`.

[2] Leigh R. Hochberg et al. "Reach and grasp by people with tetraplegia using a neurally controlled robotic arm". In: *Nature* 485.7398 (2012). Publisher: Nature Publishing Group, pp. 372–375. DOI: `10.1038/nature11076`.

[3] Christian Herff, Dean J. Krusienski, and Pieter Kubben. "The Potential of Stereotactic-EEG for Brain-Computer Interfaces: Current Progress and Future Directions". English. In: *Frontiers in Neuroscience* 14 (2020). Publisher: Frontiers. DOI: `10.3389/fnins.2020.00123`.

[4] Jeroen G.V. Habets et al. "An update on adaptive deep brain stimulation in Parkinson's disease". In: *Movement Disorders* 33.12 (2018), pp. 1834–1843. DOI: `10.1002/mds.115`.

[5] Constantinos Loukas and Peter Brown. "Online prediction of self-paced hand-movements from subthalamic activity using neural networks in Parkinson's disease". en. In: *Journal of Neuroscience Methods* 137.2 (Aug. 2004), pp. 193–205. DOI: `10.1016/j.jneumeth.2004.02.017`.

[6] K. A. Mamun et al. "Movement decoding using neural synchronization and inter-hemispheric connectivity from deep brain local field potentials". In: *Journal of Neural Engineering* 12.5 (2015). Publisher: IOP Publishing. DOI: `10.1088/1741-2560/12/5/056011`.

[7] Huiling Tan et al. "Decoding gripping force based on local field potentials recorded from subthalamic nucleus in humans". In: *eLife* 5.November (2016), pp. 1–24. DOI: `10.7554/eLife.19089`.

[8] Petra Fischer et al. "Subthalamic nucleus beta and gamma activity is modulated depending on the level of imagined grip force". In: *Experimental Neurology* 293 (2017). Publisher: The Authors, pp. 53–61. DOI: `10.1016/j.expneurol.2017.03.015`.

[9] Syed Ahmar Shah et al. "Towards Real-Time, Continuous Decoding of Gripping Force from Deep Brain Local Field Potentials". In: *IEEE Transactions on Neural Systems and Rehabilitation Engineering* 26.7 (2018). Publisher: IEEE, pp. 1460–1468. DOI: `10.1109/TNSRE.2018.2837500`.

[10] Brian A. Murphy et al. "Contributions of subsurface cortical modulations to discrimination of executed and imagined grasp forces through stereoelectroencephalography". In: *PLoS ONE* 11.3 (2016), pp. 1–21. DOI: `10.1371/journal.pone.0150359`.

[11] Meng Wang et al. "Enhancing gesture decoding performance using signals from posterior parietal cortex: a stereo-electroencephalograhy (SEEG) study". en. In: *Journal of Neural Engineering* 17.4 (Sept. 2020). Publisher: IOP Publishing, p. 046043. DOI: `10.1088/1741-2552/ab9987`.

[12]   MacAuley Smith Breault et al. "Non-motor Brain Regions in Non-dominant Hemisphere Are Influential in Decoding Movement Speed". In: *Frontiers in Neuroscience* 13.JUL (July 2019), pp. 1–13. DOI: 10.3389/fnins.2019.00715.

[13]   H. Ramoser, J. Muller-Gerking, and G. Pfurtscheller. "Optimal spatial filtering of single trial EEG during imagined hand movement". In: *IEEE Transactions on Rehabilitation Engineering* 8.4 (Dec. 2000). Conference Name: IEEE Transactions on Rehabilitation Engineering, pp. 441–446. DOI: 10.1109/86.895946.

[14]   Saed Khawaldeh et al. "Subthalamic nucleus activity dynamics and limb movement prediction in Parkinson's disease". In: *Brain* 143.2 (Feb. 2020), pp. 582–596. DOI: 10.1093/brain/awz417.

[15]   Kai J. Miller et al. "Spectral Changes in Cortical Surface Potentials during Motor Movement". en. In: *Journal of Neuroscience* 27.9 (Feb. 2007). Publisher: Society for Neuroscience Section: Articles, pp. 2424–2432. DOI: 10.1523/JNEUROSCI.3886-06.2007.

[16]   A. M. Dale, B. Fischl, and M. I. Sereno. "Cortical surface-based analysis. I. Segmentation and surface reconstruction". eng. In: *NeuroImage* 9.2 (Feb. 1999), pp. 179–194. DOI: 10.1006/nimg.1998.0395.

[17]   Liberty S. Hamilton et al. "Semi-automated Anatomical Labeling and Inter-subject Warping of High-Density Intracranial Recording Electrodes in Electrocorticography". English. In: *Frontiers in Neuroinformatics* 11 (2017). Publisher: Frontiers. DOI: 10.3389/fninf.2017.00062.

[18]   Christian Kothe. *sccn/labstreaminglayer*. original-date: 2018-02-28T10:50:12Z. 2014.

[19]   Alexandre Gramfort et al. "MNE software for processing MEG and EEG data". eng. In: *NeuroImage* 86 (Feb. 2014), pp. 446–460. DOI: 10.1016/j.neuroimage.2013.10.027.

[20]   Fabian Pedregosa, Ron Weiss, and Matthieu Brucher. "Scikit-learn : Machine Learning in Python". In: *Journal of machine learning research* 12 (2011), pp. 2825–2830.

[21]   Luca Turella and Angelika Lingnau. "Neural correlates of grasping". eng. In: *Frontiers in Human Neuroscience* 8 (2014), p. 686. DOI: 10.3389/fnhum.2014.00686.

[22]   Manuel R Mercier et al. "Evaluation of cortical local field potential diffusion in stereotactic electro-encephalography recordings: A glimpse on white matter signal". In: *NeuroImage* 147 (2017). Publisher: Elsevier, pp. 219–232. DOI: 10.1016/j.neuroimage.2016.08.037.

[23]   Simon Little et al. "Human motor cortical beta bursts relate to movement planning and response errors". en. In: *PLOS Biology* 17.10 (Oct. 2019). Publisher: Public Library of Science, e3000479. DOI: 10.1371/journal.pbio.3000479.
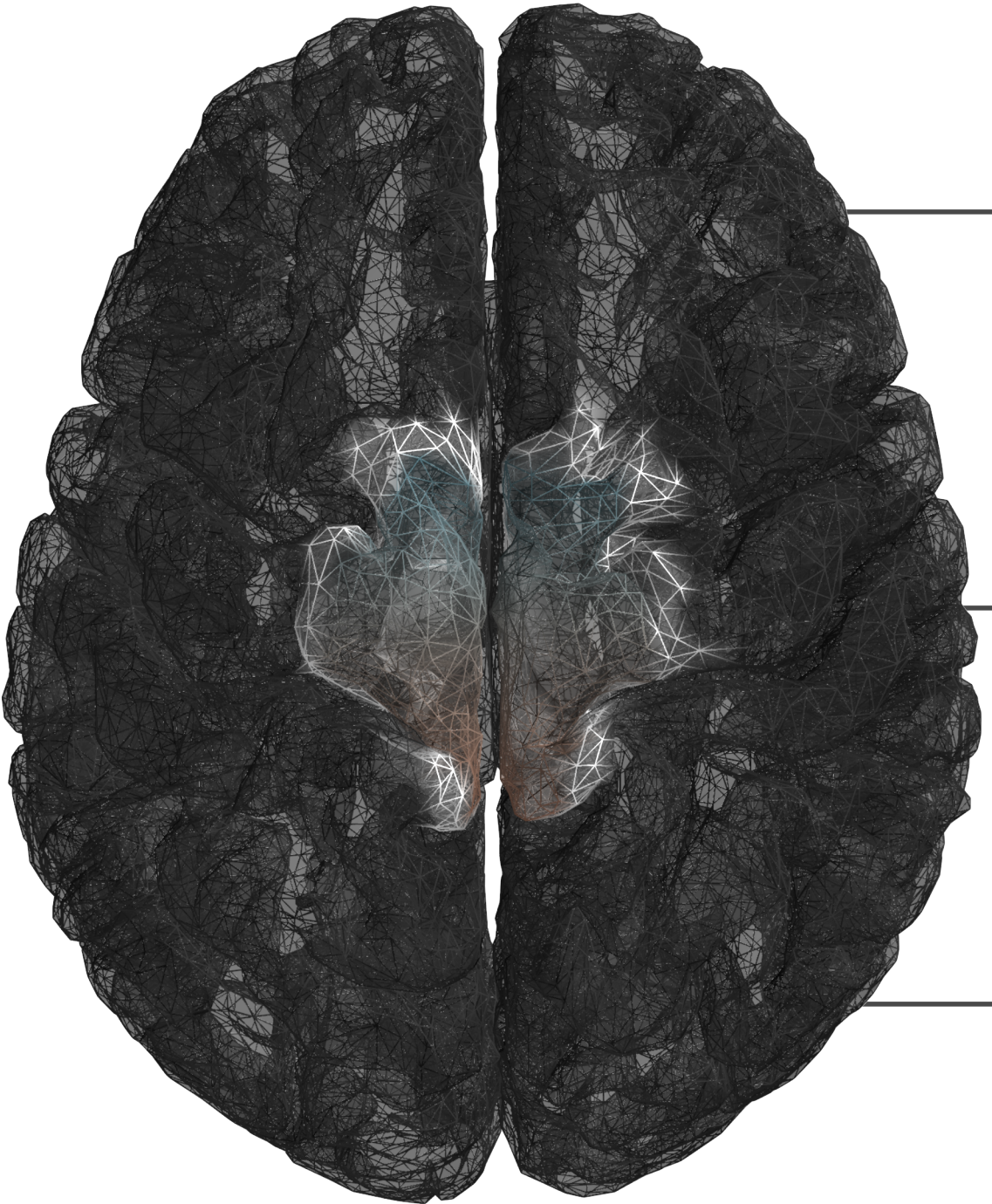
3

Decoding executed and imagined grasping movements from distributed non-motor brain areas using a Riemannian decoder

2023

M.C. Ottenhoff, M. Verwoert, S. Goulis, A.J. Colon, L. Wagner, S. Tousseyn, J.P. van Dijk, P.L. Kubben and C. Herff

Abstract

Using brain activity directly as input for assistive tool control can circumvent muscular dysfunction and increase functional independence for physically impaired people. The motor cortex is commonly targeted for recordings, while growing evidence shows that there exists decodable movement-related neural activity outside of the motor cortex. Several decoding studies demonstrated significant decoding from distributed areas separately. Here, we combine information from all recorded non-motor brain areas and decode executed and imagined movements using a Riemannian decoder. We recorded neural activity from 8 epilepsy patients implanted with stereotactic-electroencephalographic electrodes (sEEG), while they performed an executed and imagined grasping tasks. Before decoding, we excluded all contacts in or adjacent to the central sulcus. The decoder extracts a low-dimensional representation of varying number of components, and classified move/no-move using a minimum-distance-to-geometric-mean Riemannian classifier. We show that executed and imagined movements can be decoded from distributed non-motor brain areas using a Riemannian decoder, reaching an area under the receiver operator characteristic of 0.83 ± 0.11. Furthermore, we highlight the distributedness of the movement-related neural activity, as no single brain area is the main driver of performance. Our decoding results demonstrate a first application of a Riemannian decoder on sEEG data and show that it is able to decode from distributed brain-wide recordings outside of the motor cortex. This brief report highlights the perspective to explore motor-related neural activity beyond the motor cortex, as many areas contain decodable information.

3.1 Introduction

Motor neuron diseases, aging-related diseases and accidents can lead to losing a part of or complete muscle control: in the Netherlands alone, 415.000 people are experiencing severe physical disability (2011) [1, 2]. A main predictor of their life satisfaction is their functional independence [3, 4], which could be regained with appropriate assistive tools. An intuitive way to increase functional independence again is to circumvent muscular dysfunction by using brain activity directly as input for control of assistive tools [5, 6]. To achieve this, decoding studies target the primary motor cortex to capture movement-related neural activity [7–10]. For example, implantations of microelectrode arrays (MEA) in the hand-knob area of the human primary motor cortex have resulted in state-of-the-art decoders that can decode imagined handwriting at speeds comparable to regular smartphone typing [11]. However, the motor-related activity from the motor cortex may not capture the full extent of the motor system [12], as descending motor neurons and concrete motor commands originate from other brain areas than the primary motor cortex as well [13]. Furthermore, motor-related activity is more widespread than previously thought [14].

Accordingly, multiple invasive studies reported decoding of motor-related activity outside of the motor cortex in humans, and found significant decoding results from multiple cortical and sub-cortical areas, such as the ventral premotor cortex [15], posterior parietal cortex [16–18], somatosensory cortex [15], supramarginal gyrus [15, 17], temporal areas [19], insula [17, 19], hippocampus [17, 19], basal ganglia [20] and subthalamic nucleus [21]. So far, all non-primary motor decoding studies show promising results by decoding significantly above chance from many areas individually. Leveraging all brain-wide information by including all channels may increase decoding power.

However, including all channels increases the risk of a poor decoder fit. The increased dimensionality may leave too little data to for the decoder to train on. Furthermore, including neural activity from brain wide areas might include more channels that do not hold any movement-related information, decreasing the signal-to-noise ratio. To address this

dimensionality issue, techniques such as principal component analysis can be used to acquire a low-dimensional representation of the neural data [22]. Furthermore, techniques like Riemannian decoders [23] used in surface EEG, known for its low signal to noise ratio, may be applicable to sEEG data as well.

Here, we expand from decoding movement from individual non-motor brain areas to including all available information, We capture whole-brain activity by recording data from stereotactic electroencephalographic (sEEG) electrodes implanted in epilepsy patients. Combined over participants these electrodes cover the whole brain and provide a high-spatial and temporal resolution [24]. To ensure we only include data from non-primary motor areas, we remove all electrode contacts around the central sulcus bilaterally. We reduce dimensionality of the signal into a low-dimensional representation and apply a Riemannian decoder that directly classifies based on the covariance matrix of this representation (Figure 3.1a). We show significant above chance performance for both executed and imagined movements for nearly all number of principal components (Figure 3.2), without the need for areas surrounding the central sulcus.
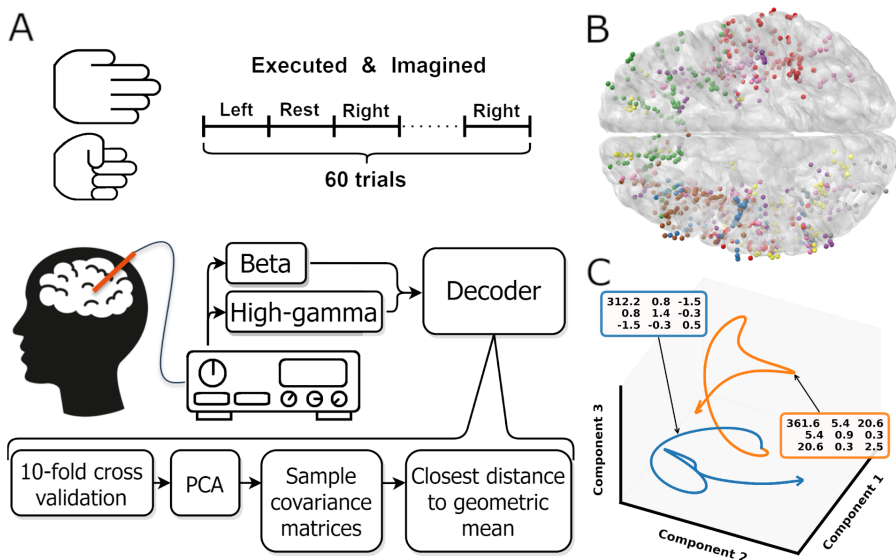
Figure 3.1: **A**) Overview experimental protocol. **B**) Contact locations of all participants warped onto an average brain. Each color represents contacts from one participant. **C**) Low dimensional representation of the average movement (blue) and rest (orange) trial for one participant. For both trajectories the covariance matrix of the first three components is shown in the colored boxes. These covariance matrices are used as input for the Riemannian decoder. The trajectories, shown are smoothed by a low pass filter, the unsmoothed trajectories are shown in supplementary figure 1. Note that the trajectories are clearly separated in the space spanned by the first three components.

3.2 Methods

Participants

Eight participants were included in this work (age 35.8 ± 14.2 years, mean $\pm$ SD; 5 male, 3 female, supplementary table 1). All participants are refractory epilepsy patients undergoing presurgical assessment for resection surgery. They were implanted with sEEG electrodes for two to three weeks to monitor seizures and identify the epileptogenic zone. The electrode placement and trajectories were determined solely based on their clinical needs. Participants were implanted with 5 to 14 electrodes containing 42 to 125 recordable contacts.

Tasks

Each participant was asked to continuously open and close their hand for 3 s per trial follow by a 3 s rest period. 30 trials were cued per hand, resulting in 60 move and 60 rest trials (Figure 3.1a). The stimuli were presented in random order on a laptop screen that was resting on the participants lap or on a table in front. We ran the protocol for executed and imagined grasping movements. Participants were instructed to move only their hands and to keep the rest of their body still during executed grasping. For imagined movements, the participants were asked to remain completely still, and the experimenter visually checked if the participants adhered to the instruction. We did not use stricter or more objective methods like electromyography (EMG) to measure any micro-movements or increased muscle tension [25]. In our experience, participants often find it challenging to imagine movements. Therefore, we always preceded the imagined grasping task with the executed grasping task to provide the participant with a fresh memory of the kinematic and proprioceptive sensation of a grasping movement. We assumed it was easier for our participant to recall a mental image of the grasping movement, helping them to perform the imagery task as good as possible. Additionally, the experimenter briefly introduced two potential imagery strategies: kinesthetic or visual [26], but the participants were free to use any strategy that they thought was most effective for them.

Ethical approval

The experimental protocol was approved by the institutional review board of Maastricht University and Epilepsy Center Kempenhaeghe (METC 2018-0451). All experiments were in accordance with the local guidelines and regulations and under supervision of experienced healthcare staff. All participants joined the study voluntarily and gave written informed consent.

Data Recording

Neural activity was recorded by platinum-iridium sEEG electrodes (Microdeep intracerebral electrodes; Dixi Medical, Beçanson, France) us-

ing two stacked 64-channel Micromed SD LTM Amplifiers (Micromed S.p.A., Treviso, Italy). The electrodes are 0.8mm in diameter and contain 5 to 18 contacts.The contacts are 2mm in length, have a 1.5mm intercontact distance, and are referenced to a white matter electrode that did not show epileptic activity, visually determined by the epileptologist. All recordings and stimuli were synchronized using LabStreamingLayer [27]. For clarity, throughout this work we refer to 'electrode' as the implanted shaft and 'contact' for each location on each electrode where activity is measured.

Imaging

The anatomical locations for each contact were determined using the img_pipe Python package [28] and parcellation based on the Destrieux atlas [29]. To do so, we coregistered a pre-implantation anatomical T1-weighted MRI scan, parcellated using Freesurfer (https://surfer.nmr.mgh.harvard.edu/), and a post-implantation CT scan. For visualization purposes, the electrodes were warped to average brain from the CVS average-35 atlas in MNI152 space.

To remove motor cortical areas we excluded all contacts of which the determined anatomical label contained the word 'motor' or 'central' (supplementary data 1). This was a strict exclusion of contacts, meaning that contacts in white matter close to the central sulcus and primary (sensori-)motor cortex are removed as well. Note that the white matter anatomical labels in the Destrieux atlas are based on proximity to labeled grey matter area, introducing some uncertainty of the exact location.

Electrode coverage

In total, 956 contacts on 82 electrodes were implanted in our participants, with electrodes containing a minimum of 5 and a maximum of 18 contacts per electrode (Figure 3.1b). All contacts across participants covered 59 unique grey matter areas with 448 contacts, where the superior insular sulcus is covered the most ($n = 25$) followed by the superior temporal sulcus ($n = 23$) and the middle frontal gyrus ($n = 23$). The remaining contacts are located in white matter ($n = 408$) or unknown ar-

eas ($n = 100$). Unknown areas are areas that could not be identified due to various technical reasons. See supplementary data 5 for a graphical overview of all areas. Because of a limited number of channels ($n = 128$) that can be recorded by the amplifiers, not all contact could be recorded, reducing the total amount of recorded contacts by 71 (supplementary table 1). The selection of which contacts should be included was made by the epileptologist for clinical reasons. The amount of recorded contacts left after motor and noise removal are shown in supplementary table 1.

Preprocessing

First, we removed all contact in areas in or adjacent to the central sulcus (Supplementary data 2 for a complete list of removed labels). Then, we evaluated the signal quality of each contact by assessing excessive noise. First, contacts were flagged if the 50 Hz frequency band power exceeded two times the interquartile range of the signal. Additionally, contacts with a z-scored log square mean value that was significantly higher ($p < 0.05$, assuming normal distribution) than the values in other contacts were flagged for abnormal amplitude (supplementary table 1). The remaining contacts were detrended, demeaned and band-stop filtered for 50 Hz line noise its and harmonics up to and including 200Hz, using a finite impulse response filter implemented in the MNE python package [30]. Then, we extracted beta (12-30Hz) and high-gamma (55-90Hz) envelope by taking the absolute of the Hilbert transform on the band-passed filtered signal. These frequency bands are chosen as they are known to be movement related and have shown to be effective in decoding studies [7, 31–33]. After preprocessing, the data was split into trials. Left and right hand movement trials were combined into a single movement class.

Decoder

A decoder was trained and tested for [3, 5, 10, ..., 50] principle components and beta, high-gamma and beta + high-gamma bands. One participant had less than 50 contacts and could therefore not be evaluated with 50 components. Each component and band combination was trained and

evaluated as follows: first, the data was split using 10-fold cross valida-
tion. On the training data, the data was standardized over all included
trials per fold and a principal component analysis was performed. The
learned transformation was subsequently used to transform the train-
ing and test fold to the specific amount of principal components. Af-
ter transformation into the components space, the sample covariance
matrix for each trial was calculated and regularized by the Ledoit-Wolf
lemma [34]. Figure 3.1c shows the average behavior per class for one par-
ticipant. The covariance matrices are used as input for the Riemannian
decoder. Then, the geometric mean per class was calculated based on
the Kullback-Leibler divergence. Trials were then classified by select-
ing the class with the shortest distance to class geometric mean. For the
calculations, we used the pyRiemann implementation [35].

Evaluation
We evaluated the decoder by the area under the receiver operator char-
acteristics (AUC). We tested statistical significance against chance level
(mean $AUC = 0.5$) using a one sample t-test and corrected for mul-
tiple testing using Bonferroni correction. For the control analysis for
motor cortical areas, we used a Wilcoxon signed rank-test (Bonferroni
corrected, $n = 66$, Supplementary Table 2) to compare the difference in
performance with and without motor cortical areas. We compared the
Riemannian decoder with a common spatial pattern [36] and linear dis-
criminant analysis (CSP-LDA) decoder. Covariance matrices estimated
during the CSP analysis were regularized using Ledoit-Wolf regulariza-
tion [34]. After spatial filtering, the average power for each CSP was cal-
culated. We used the MNE implementation of CSP [30].

3.3 Results
Our classifier was able to decode executed movements from rest periods
significantly above chance for all number of principal components and
frequency features, except beta using 3 or 5 components. The highest
performance was achieved by combining beta and high-gamma activity
with 45 principal components (0.83 ± 0.11 AUC $\pm$ SD, Figure 3.2). Using

only beta or high-gamma reached 0.81±0.12 and 0.75±0.10, respectively. For the imagined movement task, the decoder reached above chance performance for most number of components for both beta and beta + high-gamma. However, including only high-gamma produced barely any significant decoding results. Lower number of principal components did not reach above chance decoding, specifically: 3 and 5 in beta, 3, 5 or 10 in beta + high-gamma. Overall, decoding imagined movements yielded lower performance than decoding executed movements. The maximum performance for imagined movements using beta, high-gamma or beta + high-gamma was 0.68 ± 0.08, 0.63 ± 0.08 and 0.66 ± 0.06, respectively. The decoder performed comparable to a CSP-LDA decoder, where the latter performed better with fewer CSPs ($< \pm25$) and the former with more components ($> \pm25$, supplementary figure 2)

For high-gamma and beta + high-gamma in executed movements, the decoder was able to decode significantly above chance for all number of principal components. For beta, at least 10 were required. In the imagined tasks, at least 10 components were required as well for beta power. For high-gamma however, only 30 and 40 components were sufficient. Combining both beta and high-gamma showed that at least 15 components were required. Overall, it seems that 10 to 15 components are sufficient to reliably decode movement in both tasks. Increasing the amount of components gradually increases performance, where the maximum performance is between 35 to 50 components. However, the increase in performance per extra component decreases as more components are added, and stabilizes at about 25 components.

In this work, we included all available contacts in the decoding pipeline, except those around the central sulcus. When vizualizing the contribution of each electrode to the first principal components, a distributed pattern is visible (Figure 3.3, red and yellow for high and low contribution, respectively). While there are a few regions contributing more to the first component than others, mostly posterior areas, it seems like motor-related information is distributed throughout the brain. Specifically considering that at least 3 to 10 components are required for above chance decoding.
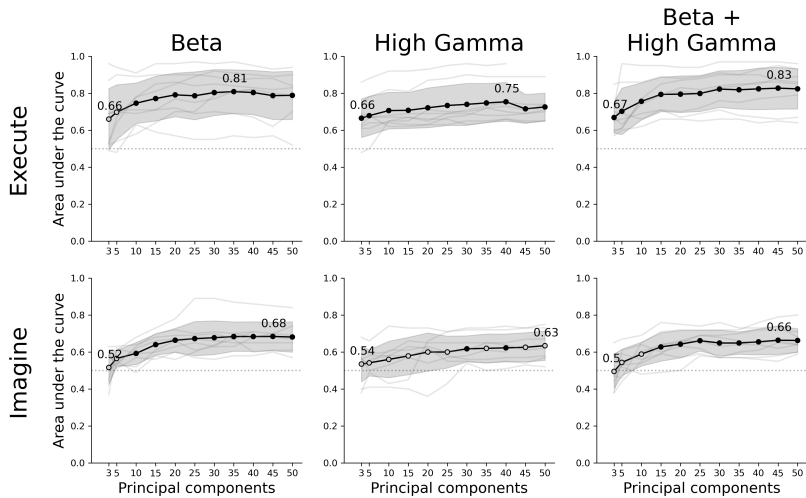
Figure 3.2: Decoder performance for different movement tasks, frequency features and number of components. The rows show the results of the executed or imagined movement task and the columns each frequency feature set used as input for the decoder. The x-axis depicts the amount of principal components extracted from the data set and the y-axis the AUC score. The light grey lines show the individual average scores over all folds per participant and the black circles are the average scores for each number of components. A filled black circle represents an average score that is significantly above chance (corrected for multiple testing), whereas an empty circle is not significant. The grey shaded area shows the standard deviation over participants and the dotted line the chance level (0.5 AUC).
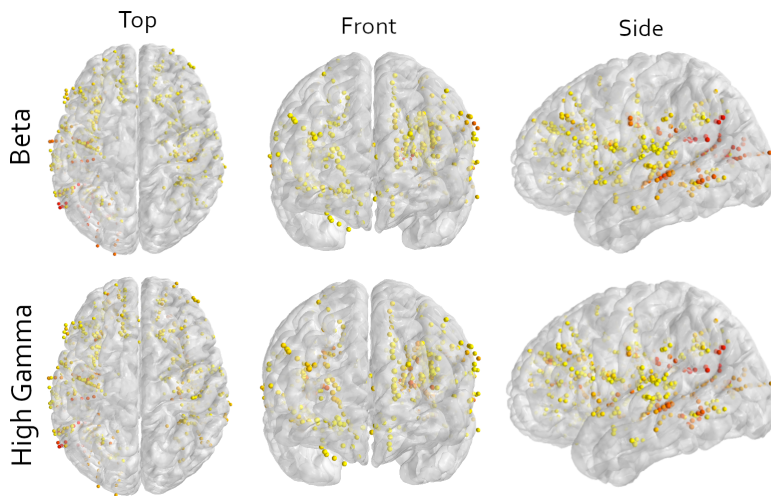
Figure 3.3: Multi-angle view of all contacts of all participants warped to an average brain for either the beta or high-gamma frequency in the imagined movement task. All contacts in motor cortical areas are excluded. The color indicates the contribution of that contact to the first principal component, scaled to the explained variance of that component. Yellow means low contribution and red mean high contribution. The image shows that orange and red colors are not bound to a specific area, illustrating the wide distribution of information. Note that here only the contributions to the first principal components are shown and that sufficient decoding requires at least 3 components (Figure 3.2). Furthermore, to visualize all contacts, the electrodes are non-linearly warped onto an average brain. This may result in contacts appearing to be in or around the central sulcus. This is an unpreventable visual artifact, and all locations are determined in the patient's native space.

3.4 Discussion

Here, we demonstrate that a Riemannian decoder is able to decode both executed and imagined movements using a low-dimensional representation from distributed brain-wide recordings. Furthermore, we show that non-motor brain areas contain sufficient information for our decoder to predict movement significantly above chance.

Our results support the notion that movement-related activity is widespread throughout the brain and that extracting a lower-dimensional representation is effective to capture this distributed activity [12, 37]. So far, studies decoding motor-related activity from distributed recordings have investigated contributions per contact or grouped cortical areas [15–17]. Here, we expand to include neural activity from all brain regions, excluding those surrounding the central sulcus. Using this approach, we were able to decode significantly above chance for almost all participants. Specifically, when using beta & high-gamma as input power bands, we were able to decode above chance, regardless of electrode configuration (Figure 3.2).

Although our decoder was able to predict movements, the used methods include any signal that is relevant for the classification task, and no selection is made based on a mechanistic presumption. Thus, the relevant information may also include any other motor related signal, like motor planning, sequencing or decision-making, as well as non-motor information such as attention, stimulus processing, stimulus comprehension or spatial information. The used paradigm does not allow us to make an inference of the contents of the neural signals. Nonetheless, looking at the contributions per electrode indicates that it is not a single area driving the performance, but the combination of many different non-motor areas (Figure 3.3). This is supported by the observation that multiple different electrode configurations resulted in above chance decoding (Figure 3.2, Figure 3.1b).

The performance of our Riemannian decoder demonstrates that this type of decoder is applicable to the distributed recordings of sEEG. The presented pipeline is simple and near non-parametric. While there are multiple variations of Riemannian decoders [38], the only parameter we

choose was the distance metric (Kullback-Leibler, based on Chevallier et al. [39]), and the number of principal components. When using Riemannian decoders the dimensionality should preferably to be low. During training, the decoder calculates the geometric mean between all sample covariance matrices per class, which is an optimization problem that scales exponentially with increased dimensions.

Furthermore, using a low-dimensional representation combines information from all contacts, which separately might not have enough information for sufficient decoding. Since the information is distributed throughout the brain, the loss of single contacts likely only has a minor influence on overall decoding performance. This is especially useful in the eventual target population, were neurodegenerative diseases might cause specific brain areas to stop contributing information, or electrode degradation can decrease the recorded activity from a contact.

Limitations
All our participants are diagnosed with refractory epilepsy, a condition of which it is unclear how it influences our decoding results. During the monitoring phase in which we perform our measurements, our participants are expected to have as much seizures as possible, albeit no seizures occurred during one of the experimental sessions. After a few days of settling in the monitoring center, medication is reduced and eventually the participants are stimulated in various forms to elicit seizures. Therefore, participants often feel drowsy and experience post-ictal discharges. We try to reduce influences as much as possible by visiting as early in their treatment as possible, but we are dependent on the clinical schedule of the patient. Lastly, our decoder is evaluated on a trial-based paradigm, and thus cannot be applied in real-time decoding applications in its current form.

3.5 Conclusion
Both executed and imagined movements can be decoded from distributed non-motor brain areas using a lower dimensional representation from sEEG electrodes. We demonstrate that a Riemannian decoder captures

relevant movement-related information that is spread throughout the brain, which hold enough information to predict movement. Future work may focus on optimizing Riemannian methods on distributed data, and application in an online paradigm.

3.6 Declarations

Acknowledgements

Author contributions
Conceptualization: MO, CH; Methodology: MO, CH; Software: MO, MV, SG, CH; Validation: MO, PK, CH; Formal Analysis: MO, CH; Investigation: MO, MV, AC, LW, ST, JD, PK, CH; Resources: AC, LW, ST, JD, PK, CH; Data Curation: MO, MV, SG, CH; Writing - original draft preparation: MO, CH; Writing - review and editing: MO, MW, SG, AC, LW, ST, JD, PK, CH; Visualization: MO, MV, SG, CH; Supervision: PK, CH; Project administration: MO, PK, CH; Funding acquisition: PK, CH.

Competing interests
None of the authors have competing interests.

Funding

Data and Code availability
The datasets presented in this study can be found at `https://osf.io/xw386`, and the accompanying code at `https://github.com/mottenhoff/distributed_motor_decoding`.

References

[1]   M de Klerk et al. *Factsheet: Mensen met een lichamelijke of verstandelijke beperking*. Dutch. 2012.

[2]   Adriaan D. de Jongh et al. "Incidence, Prevalence, and Geographical Clustering of Motor Neuron Disease in the Netherlands". en. In: *Neurology* 96.8 (Feb. 2021). Publisher: Wolters Kluwer Health, Inc. on behalf of the American Academy of Neurology Section: Article, e1227–e1236. DOI: 10.1212/WNL.0000000000011467.

[3]   Christel M. van Leeuwen et al. "Trajectories in the Course of Life Satisfaction After Spinal Cord Injury: Identification and Predictors". en. In: *Archives of Physical Medicine and Rehabilitation* 92.2 (Feb. 2011), pp. 207–213. DOI: 10.1016/j.apmr.2010.10.011.

[4]   J. Scott Richards et al. "Access to the environment and life satisfaction after spinal cord injury". en. In: *Archives of Physical Medicine and Rehabilitation*. Spinal Cord Injury 80.11 (Nov. 1999), pp. 1501–1506. DOI: 10.1016/S0003-9993(99)90264-2.

[5]   Vikash Gilja et al. "Clinical translation of a high-performance neural prosthesis". eng. In: *Nature Medicine* 21.10 (Oct. 2015), pp. 1142–1145. DOI: 10.1038/nm.3953.

[6]   Janis J. Daly and Jane E. Huggins. "Brain-Computer Interface: Current and Emerging Rehabilitation Applications". en. In: *Archives of Physical Medicine and Rehabilitation*. The Fifth International Brain-Computer Interface Meeting Presents Clinical and Translational Developments in Brain-Computer Interface Research 96.3, Supplement (Mar. 2015), S1–S7. DOI: 10.1016/j.apmr.2015.01.007.

[7]   David A. Moses et al. "Neuroprosthesis for Decoding Speech in a Paralyzed Person with Anarthria". In: *New England Journal of Medicine* 385.3 (July 2021). Publisher: Massachusetts Medical Society _eprint: https://doi.org/10.1056/NEJMoa2027540, pp. 217–227. DOI: 10.1056/NEJMoa2027540.

[8]   Sharlene N. Flesher et al. "A brain-computer interface that evokes tactile sensations improves robotic arm control". In: *Science* 372.6544 (May 2021). Publisher: American Association for the Advancement of Science, pp. 831–836. DOI: 10.1126/science.abd0380.

[9]   Ujwal Chaudhary et al. "Spelling interface using intracortical signals in a completely locked-in patient enabled via auditory neurofeedback training". en. In: *Nature Communications* 13.1 (Mar. 2022). Number: 1 Publisher: Nature Publishing Group, p. 1236. DOI: 10.1038/s41467-022-28859-8.

[10] Chethan Pandarinath et al. "High performance communication by people with paralysis using an intracortical brain-computer interface". eng. In: *eLife* 6 (Feb. 2017). DOI: 10.7554/eLife.18554.

[11] Francis R. Willett et al. "Hand Knob Area of Premotor Cortex Represents the Whole Body in a Compositional Way". en. In: *Cell* 181.2 (Apr. 2020), 396–409.e26. DOI: 10.1016/j.cell.2020.02.043.

[12] Juan A. Gallego, Tamar R. Makin, and Samuel D. McDougle. "Going beyond primary motor cortex to improve brain–computer interfaces". English. In: *Trends in Neurosciences* 45.3 (Mar. 2022). Publisher: Elsevier, pp. 176–183. DOI: 10.1016/j.tins.2021.12.006.

[13] Peter L. Strick, Richard P. Dum, and Jean-Alban Rathelot. "The Cortical Motor Areas and the Emergence of Motor Skills: A Neuroanatomical Perspective". eng. In: *Annual Review of Neuroscience* 44 (July 2021), pp. 425–447. DOI: 10.1146/annurev-neuro-070918-050216.

[14] Nicholas A. Steinmetz et al. "Distributed coding of choice, action and engagement across the mouse brain". en. In: *Nature* 576.7786 (Dec. 2019). Number: 7786 Publisher: Nature Publishing Group, pp. 266–273. DOI: 10.1038/s41586-019-1787-x.

[15] Sarah K. Wandelt et al. "Decoding grasp and speech signals from the cortical grasp circuit in a tetraplegic human". en. In: *Neuron* (Mar. 2022). DOI: 10.1016/j.neuron.2022.03.009.

[16] Richard A. Andersen, Tyson Aflalo, and Spencer Kellis. "From thought to action: The brain–machine interface in posterior parietal cortex". In: *Proceedings of the National Academy of Sciences* 116.52 (Dec. 2019). Publisher: Proceedings of the National Academy of Sciences, pp. 26274–26279. DOI: 10.1073/pnas.1902276116.

[17] Guangye Li et al. "Assessing differential representation of hand movements in multiple domains using stereo-electroencephalographic recordings". en. In: *NeuroImage* 250 (Apr. 2022), p. 118969. DOI: 10.1016/j.neuroimage.2022.118969.

[18] Meng Wang et al. "Enhancing gesture decoding performance using signals from posterior parietal cortex: a stereo-electroencephalograhy (SEEG) study". en. In: *Journal of Neural Engineering* 17.4 (Sept. 2020). Publisher: IOP Publishing, p. 046043. DOI: 10.1088/1741-2552/ab9987.

[19] Macauley Smith Breault et al. "Neural Correlates of Internal States that Capture Movement Variability". In: *2019 41st Annual International Conference of the IEEE Engineering in Medicine and Biology Society (EMBC)*. ISSN: 1558-4615. July 2019, pp. 534–537. DOI: 10.1109/EMBC.2019.8856778.

[20] K. A. Mamun et al. "Movement decoding using neural synchronization and inter-hemispheric connectivity from deep brain local field potentials". In: *Journal of Neural Engineering* 12.5 (2015). Publisher: IOP Publishing. DOI: 10.1088/1741-2560/12/5/056011.

[21] Syed Ahmar Shah et al. "Towards Real-Time, Continuous Decoding of Gripping Force from Deep Brain Local Field Potentials". In: *IEEE Transactions on Neural Systems and Rehabilitation Engineering* 26.7 (2018). Publisher: IEEE, pp. 1460–1468. DOI: 10.1109/TNSRE.2018.2837500.

[22] Juan A. Gallego et al. "Cortical population activity within a preserved neural manifold underlies multiple motor behaviors". en. In: *Nature Communications* 9.1 (Oct. 2018). Number: 1 Publisher: Nature Publishing Group, p. 4233. DOI: 10.1038/s41467-018-06560-z.

[23] Marco Congedo, Alexandre Barachant, and Rajendra Bhatia. "Riemannian geometry for EEG-based brain-computer interfaces; a primer and a review". In: *Brain-Computer Interfaces* 4.3 (July 2017). Publisher: Taylor & Francis _eprint: https://doi.org/10.1080/2326263X.2017.1297192, pp. 155–174. DOI: 10.1080/2326263X.2017.1297192.

[24] Christian Herff, Dean J. Krusienski, and Pieter Kubben. "The Potential of Stereotactic-EEG for Brain-Computer Interfaces: Current Progress and Future Directions". English. In: *Frontiers in Neuroscience* 14 (2020). Publisher: Frontiers. DOI: 10.3389/fnins.2020.00123.

[25] Andreea I. Sburlea and Gernot R. Müller-Putz. "Exploring representations of human grasping in neural, muscle and kinematic signals". In: *Scientific Reports* 8.1 (2018), pp. 1–14. DOI: 10.1038/s41598-018-35018-x.

[26]   Takashi Hanakawa. "Organizing motor imageries". In: *Neuroscience Research* 104 (2016). Publisher: Elsevier Ireland Ltd and Japan Neuroscience Society, pp. 56–63. DOI: 10.1016/j.neures.2015.11.003.

[27]   C Kothe. *Lab Streaming Layer (lsl)*. 2014.

[28]   Liberty S. Hamilton et al. "Semi-automated Anatomical Labeling and Inter-subject Warping of High-Density Intracranial Recording Electrodes in Electrocorticography". English. In: *Frontiers in Neuroinformatics* 11 (2017). Publisher: Frontiers. DOI: 10.3389/fninf.2017.00062.

[29]   Christophe Destrieux et al. "Automatic parcellation of human cortical gyri and sulci using standard anatomical nomenclature". eng. In: *NeuroImage* 53.1 (Oct. 2010), pp. 1–15. DOI: 10.1016/j.neuroimage.2010.06.010.

[30]   Alexandre Gramfort et al. "MNE software for processing MEG and EEG data". eng. In: *NeuroImage* 86 (Feb. 2014), pp. 446–460. DOI: 10.1016/j.neuroimage.2013.10.027.

[31]   Cory T. Miller et al. "Natural behavior is the language of the brain". English. In: *Current Biology* 32.10 (May 2022). Publisher: Elsevier, R482–R493. DOI: 10.1016/j.cub.2022.03.031.

[32]   Etienne Combrisson et al. "From intentions to actions: Neural oscillations encode motor processes through phase, amplitude and phase-amplitude coupling". In: *NeuroImage* 147.November 2016 (2017). Publisher: Elsevier, pp. 473–487. DOI: 10.1016/j.neuroimage.2016.11.042.

[33]   Syed A. Shah, Huiling Tan, and Peter Brown. "Continuous force decoding from deep brain local field potentials for Brain Computer Interfacing". In: *International IEEE/EMBS Conference on Neural Engineering, NER* (2017). ISBN: 9781538619162, pp. 371–374. DOI: 10.1109/NER.2017.8008367.

[34]   Olivier Ledoit and Michael Wolf. "Honey, I Shrunk the Sample Covariance Matrix". en. In: *The Journal of Portfolio Management* 30.4 (July 2004). Publisher: Institutional Investor Journals Umbrella Section: Primary Article, pp. 110–119. DOI: 10.3905/jpm.2004.110.

[35]   A. Barachant. *pyRiemann v0.2.2*. June 2015. DOI: 10.5281/zenodo.18982.

[36]   Z. J. Koles, M. S. Lazar, and S. Z. Zhou. "Spatial patterns underlying population differences in the background EEG". eng. In: *Brain Topography* 2.4 (1990), pp. 275–284. DOI: 10.1007/BF01129656.

[37]   Carsen Stringer et al. "Spontaneous Behaviors Drive Multidimensional, Brain-wide Activity". In: *Science* 364.6437 (Apr. 2019), p. 255. DOI: 10.1126/science.aav7893.

[38]   Florian Yger, Maxime Berar, and Fabien Lotte. "Riemannian Approaches in Brain-Computer Interfaces: A Review". In: *IEEE Transactions on Neural Systems and Rehabilitation Engineering* 25.10 (Oct. 2017). Conference Name: IEEE Transactions on Neural Systems and Rehabilitation Engineering, pp. 1753–1762. DOI: 10.1109/TNSRE.2016.2627016.

[39]   S. Chevallier et al. "Review of Riemannian Distances and Divergences, Applied to SSVEP-based BCI". en. In: *Neuroinformatics* 19.1 (Jan. 2021), pp. 93–106. DOI: 10.1007/s12021-020-09473-9.

3.7 Supplementary material
Participants characteristics

#	Age	Sex	Sample rate	Electrodes	Contacts		Noise		Motor
					Executed	Imagined	Executed	Imagined	
1	16	M	2048	14	116	116	8	8	10
2	47	M	1024	11	110	108	20	22	0
3	52	M	1024	6	54	52	65	67	9
4	22	F	1024	5	42	44	85	83	0
5	20	F	1024	11	106	105	13	14	6
6	40	M	1024	12	117	117	13	13	0
7	55	F	1024	12	108	105	15	18	8
8	34	M	1024	11	108	106	17	19	3

Supplementary data 1 - Participants and their electrode configurations. 'Contacts' denotes the amount of contacts after noise and motor removal. 'Motor' denotes the amount of contacts located in an area surrounding the central sulcus.

Excluded areas
Supplementary data 2 - List of removed areas surrounding the central sulcus

- ctx-rh-paracentral
- ctx-rh-precentral
- ctx-rh-postcentral
- wm-lh-paracentral
- wm-lh-postcentral
- wm-lh-precentral
- wm-rh-paracentral
- wm-rh-postcentral
- wm-rh-precentral
- ctx-lh-G_paracentral
- ctx-lh-G_postcentral
- ctx-lh-G_precentral
- ctx-lh-G_subcentralctx-lh-S_central
- ctx-lh-S_paracentral
- ctx-lh-S_postcentral
- ctx-lh-S_precentral-Inferior-part
- ctx-lh-S_precentral-Superior-part
- ctx-lh-S_subcentral_ant
- ctx-lh-S_subcentral_post
- ctx-rh-G_paracentral
- ctx-rh-G_postcentral
- ctx-rh-G_precentral
- ctx-rh-G_subcentralctx-rh-S_central
- ctx-rh-S_paracentral
- ctx-rh-S_postcentral
- ctx-rh-S_precentral-Inferior-part
- ctx-rh-S_precentral-Superior-part
- ctx-rh-S_subcentral_ant
- ctx-rh-S_subcentral_post
- wm-lh-G_paracentral
- wm-lh-G_postcentral
- wm-lh-G_precentral
- wm-lh-G_subcentral
- wm-lh-S_central
- wm-lh-S_paracentral
- wm-lh-S_postcentral
- wm-lh-S_precentral-Inferior-part
- wm-lh-S_precentral-Superior-part
- wm-lh-S_subcentral_ant
- wm-lh-S_subcentral_post
- wm-rh-G_postcentral
- wm-rh-G_precentral
- wm-rh-G_subcentral
- wm-rh-S_central
- wm-rh-S_paracentral
- wm-rh-S_postcentral
- wm-rh-S_precentral-Inferior-part
- wm-rh-S_precentral-Superior-part
- wm-rh-S_subcentral_ant
- wm-rh-S_subcentral_post

- `ctx_lh_G_and_S_paracentral`
- `ctx_lh_G_and_S_subcentral`
- `ctx_lh_G_postcentral`
- `ctx_lh_G_precentral`
- `ctx_lh_S_central`
- `ctx_lh_S_postcentral`
- `ctx_lh_S_precentral-inf-part`
- `ctx_lh_S_precentral-sup-part`
- `ctx_rh_G_and_S_paracentral`
- `ctx_rh_G_and_S_subcentral`
- `ctx_rh_G_postcentral`
- `ctx_rh_G_precentral`
- `ctx_rh_S_central`
- `ctx_rh_S_postcentral`
- `ctx_rh_S_precentral-inf-part`
- `ctx_rh_S_precentral-sup-part`
- `wm_lh_G_and_S_paracentral`
- `wm_lh_G_and_S_subcentral`
- `wm_lh_G_postcentral`
- `wm_lh_G_precentral`
- `wm_lh_S_central`
- `wm_lh_S_postcentral`
- `wm_lh_S_precentral-inf-part`
- `wm_lh_S_precentral-sup-part`
- `wm_rh_G_and_S_paracentral`
- `wm_rh_G_and_S_subcentral`
- `wm_rh_G_postcentral`
- `wm_rh_G_precentral`
- `wm_rh_S_central`
- `wm_rh_S_postcentral`
- `wm_rh_S_precentral-inf-part`
- `wm_rh_S_precentral-sup-part`
- `ctx-lh-primary-motor`
- `ctx-lh-premotor`
- `ctx-rh-primary-motor`
- `ctx-rh-premotor`

Unsmoothed trajectories

P1

P2

P3

P4

P5

P6

P7

P8
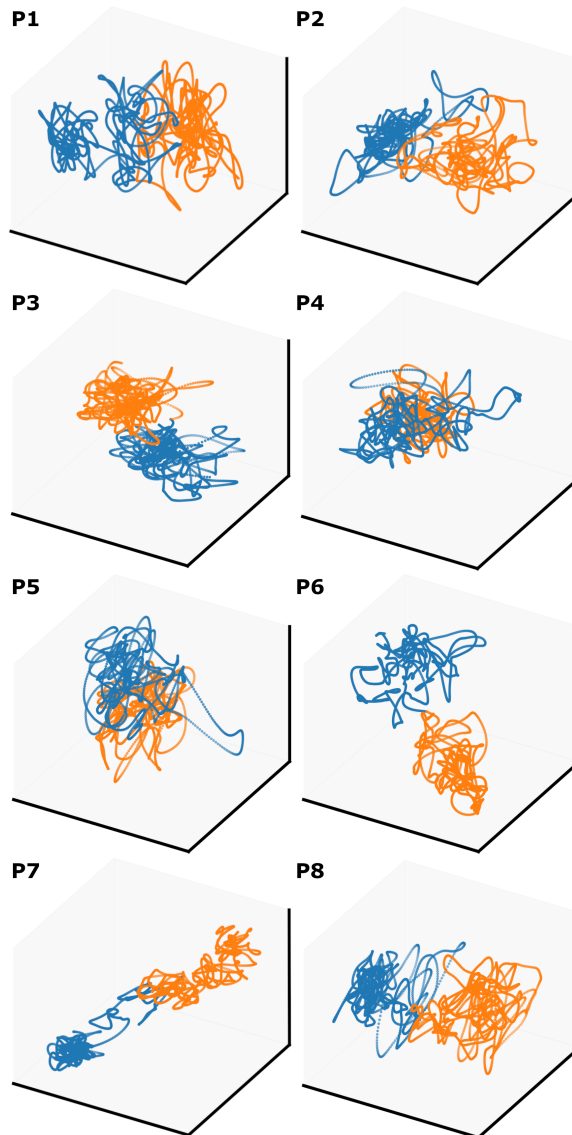
Supplementary data 3 - Unsmoothed trajectories in components space. Calculated from beta activity in executed movements. The trajectories of P8 are the same as in Figure 1c.

P-values in pairwise comparison with motor cortical areas included.

	3	5	10	15	20	25	30	35	40	45	50
Exec - Beta	0.98	0.71	0.83	0.89	0.84	0.90	0.98	0.98	1.00	0.95	0.94
Exec - High-gamma	0.86	0.79	0.93	0.86	0.95	0.75	0.91	0.89	0.92	1.00	0.97
Exec - Beta + High-gamma	0.83	0.73	0.87	0.76	0.82	0.75	0.63	0.91	0.91	0.30	0.72
Imag - Beta	0.65	0.47	0.44	0.88	0.74	0.84	0.84	0.66	0.87	0.78	0.85
Imag - High-gamma	0.80	0.97	0.75	0.77	0.98	0.92	0.93	0.82	0.79	0.80	0.76
Imag - Beta + High-gamma	0.85	0.78	0.79	0.75	0.80	0.79	0.75	0.75	0.84	0.83	0.88

Supplementary data 4 - P-values for significance tests between the performance using all electrodes and the performance without motor cortical areas. None of the tests were significant, meaning that the null hypothesis that both groups come from the same distribution cannot be rejected.
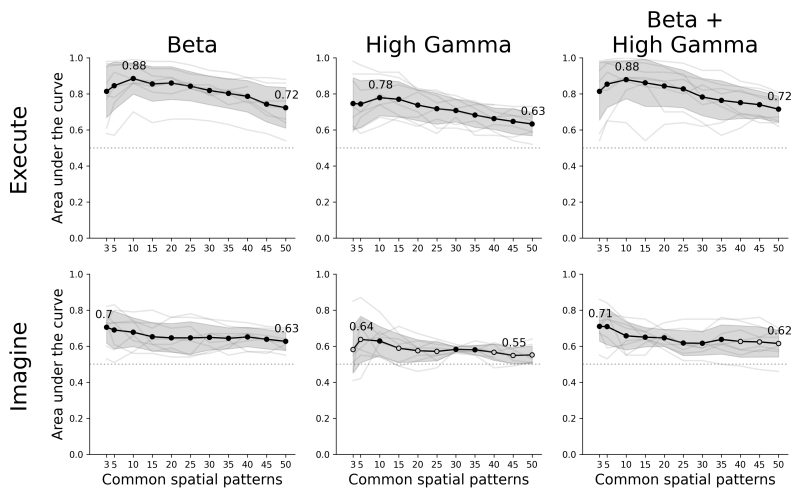
Figure 3.4: Decoding performance for a common spatial pattern (CSP) and linear discriminant analysis (LDA) decoder. Compared to the Riemannian decoder, the CSP-LDA decoder performs better with fewer spatial filters ($<$ ± 25), while the Riemannian decoder performs better with more components ($>$ ± 25).
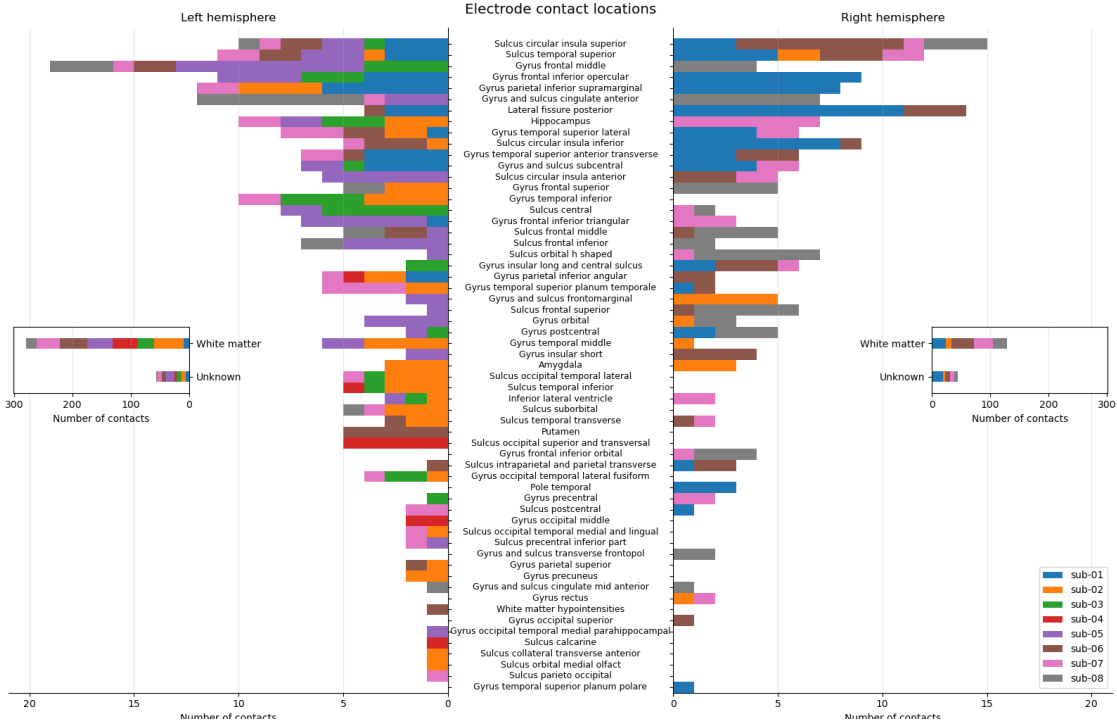
Supplementary data 5 - Captured areas by all contacts per hemisphere. The insets shows all contacts in white matter and labeled unknown. Note that the size of the X-axis on the insets is much larger than the main figure.
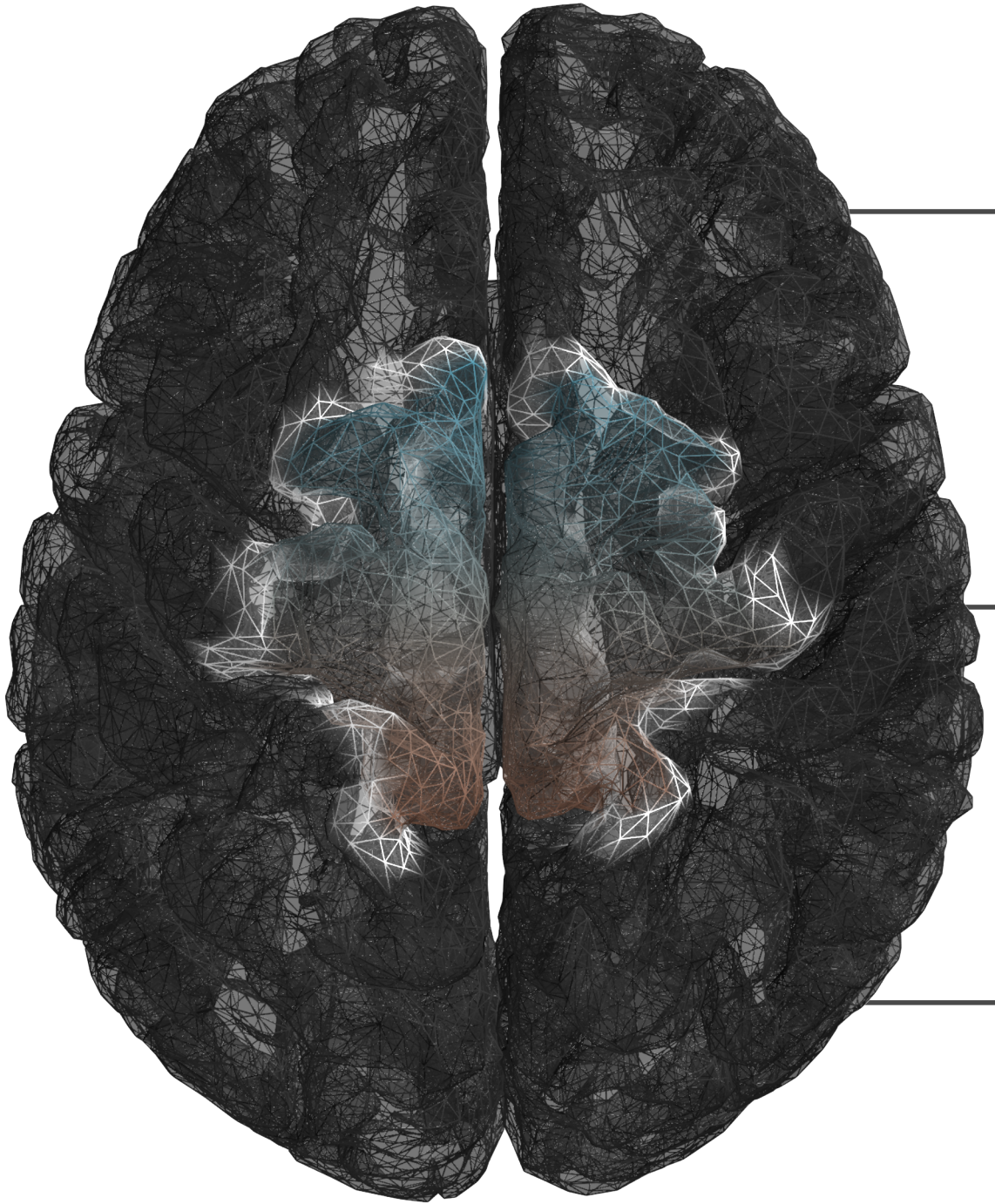
4

Global motor dynamics - Invariant neural representations of motor behavior in distributed brain-wide recordings

2023

M.C. Ottenhoff, M. Verwoert, S. Goulis, A.J. Colon, L. Wagner, S. Tousseyn, J.P. van Dijk, P.L. Kubben and C. Herff

Abstract

Neural activity is presumed to be correlated with motor behavior almost everywhere in the brain, implying that many different brain processes are involved in generating a behavioral output. Recent studies in multiple non-human species have observed pervasive brain-wide neural activity directly related to motor output. However, similar brain-wide investigations in humans with high-temporal resolution are lacking to date. Here, we recorded invasive data from brain-wide distributed electrodes in humans and reveal global neural dynamics that are predictive of movement across tasks and across participants. The dynamics are remarkably stable between participants with substantially varying electrode configurations and to loss of information. We demonstrate that these global neural dynamics are near brain-wide and present in all participants. Uncovering these global neural dynamics may allow for a more holistic and network-based perspective on motor-related neural activity.

4.1 Introduction

Nearly all decisions eventually lead to movement, and consequently most neural processes facilitate a downstream motor output. While the neural basis and localization of the processes involved remain elusive, it is conceivable that movement sparks the involvement of many different brain areas. In animals, brain-wide neural activity associated to motor output was observed in zebrafish [1] and mice [2–5], where spontaneous behaviors elicited a broadcast of neural activity throughout the dorsal cortex. Moreover, in a study with 12.000 recorded neurons in mice, nearly all neurons were strongly modulated by any type (instructed and uninstructed) of movement in mice [6]. Consequently, the authors conclude that robust movement representations might be present throughout the brain. In humans, early indications in functional magnetic resonance imaging (fMRI) suggest that similar brain-wide activity exists [7], but it has yet to be demonstrated in humans with high temporal resolution in electrophysiological recordings.

Capturing the neural substrate of these brain-wide motor-related responses in humans will not only increase our understanding of motor processes in the brain, but also allow for robust neural decoders. Results from animal studies that identified global motor-related activity suggest that there indeed exists decodable information throughout the brain. To this end, stereotactic-electroencephalographic (sEEG), also called depth electrodes, provide a unique opportunity to record from sparse but brain-wide cortical and subcortical areas, and allow us to shine light on global motor activity and its dynamics [8]. To date, motor decoding studies based on sEEG recordings have described the decoding of action (e.g. different hand signs or grasp types) from a variety of individual cortical and subcortical areas [9], including the ventral premotor cortex [10], posterior parietal cortex [11–13], somatosensory cortex [10], supramarginal gyrus [10, 12, 14], middle temporal gyrus and fusiform gyrus [14], insula [12, 14] and hippocampus [12, 14].

Given that individual areas are predictive of movements, the underlying neural dynamics between areas could increase the available information and uncover global dynamics. To capture these dynamics into

a low-dimensional representation, multiple techniques are available to reduce the neural space into a single manifold that describe the underlying neural dynamics [15–20]. Manifolds are demonstrated to capture robust representations of latent dynamics [21] and to be predictive for multiple types of behaviors [22, 23] and subjects [24]. In the context of decoding motor behavior, these neural manifold approaches have almost exclusively been used to decode spiking activity recorded in the primary motor cortex, although the methods are well suited for local field potentials recorded with sEEG electrodes.

Here, we explore motor-related activity from brain-wide distributed recordings. Eight participants implanted with sEEG electrodes performed trial-based executed and imagined motor tasks. In each 3-second trial, they continuously opened and closed either their left or right hand. In total, we recorded data from 956 contacts covering 60 unique brain areas. By extracting a low-dimensional representation, we were able to decode movements across tasks and participants using a Riemannian geometry approach (Figure 4.1, Figure 4.2a). We find remarkably stable motor dynamics that are independent of task and participant. Indeed, we were able to decode movements across participants with non-overlapping electrodes.
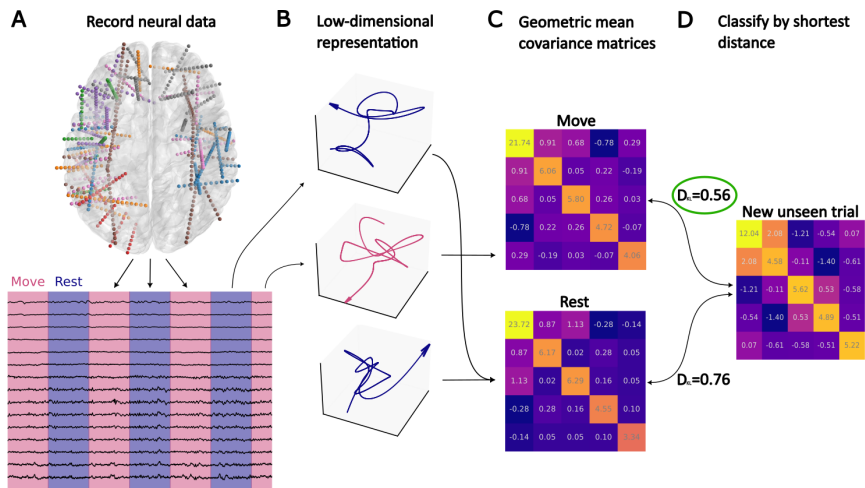
Figure 4.1: Conceptual overview of the methods. **A**) Electrode configurations of 8 participants mapped onto an average brain. A total of 956 contacts cover 60 unique brain areas. For each participant, data were recorded in 3-second trials in either a move (red) or rest (blue) trial. **B**) On the training set, principal components were extracted and each trial was transformed to a lower dimensional representation. **C**) Then, the sample covariance matrix was estimated for each trial, and for all trials per class in the training set, the geometric mean of the covariance matrices was calculated using the kullback-leibler divergence. **D**) New, unseen trials from the test set are then classified by findings the geometric class mean with the smallest kullback-leibler divergence to the new trial sample covariance matrix.

4.2 Results

Executed and imagined movement can be decoded from low-dimensional neural representations from distributed brain areas

The Riemannian geometry-based classifier was able to decode executed movements for beta, high-gamma and both frequency bands and all number of principal components (Figure 4.2b, e, h) significantly above chance level. Beta power resulted in higher decoding performance than high-gamma power (0.83 ± 0.15 area under the curve (auc) vs 0.75 ± 0.17 auc), and including both frequency bands led to similar performance

(0.84 ± 0.14 auc) as beta power. All number of principal components and frequency inputs resulted in decoding performance significantly above chance (one sample t-test, $\alpha = 0.05$, FDR corrected). Zooming in on 10 components for executed movements, based on the optimum further described in section 4.2, most participants reached above chance decoding, averaging 0.75 ± 0.18, 0.69 ± 0.18, 0.74 ± 0.18 for beta, high-gamma and both, respectively (Figure 4.2d, g, j). Inter-participant variance was high, ranging from chance level decoding to $auc > 0.9$. This is regularly observed in sEEG decoding studies due to varying electrode configurations. In the imagined task, the decoder reached above chance decoding as well for nearly all combinations of principal components and frequency bands (Figure 4.2c, f, i), except for the lower number of principal components ($n_{components} < 10$) in beta and beta & high-gamma. Compared to executed movement, the performance was lower overall, but similar between all frequency bands (0.65 ± 0.17, 0.64 ± 0.15 and 0.64 ± 0.18 auc), where beta power and beta & high-gamma power achieved the highest performance. Given that beta provides the same predictive power as both beta and high-gamma, further analyses will continue with beta power only.

The optimal amount of components remains stable under loss of information

To assess whether the extracted low-dimensional representation captures neural dynamics on a stable manifold, we performed an ablation study that progressively removed information from randomly selected channels. The number of principal components included strongly determined the baseline performance (Figure 4.3a), defined as having access to 100% of the available channels. A higher baseline performance led to a progressive decrease in stability, as the performance dropped more rapidly for models with more components when information was removed. Using $n_{components} < 10$, the performance showed no drop in performance for up to 50% information loss, whereas $n_{components} = 50$ led to a drop of 0.15 auc when losing only 10% of information. Losing even more information reduced the performance to chance level already
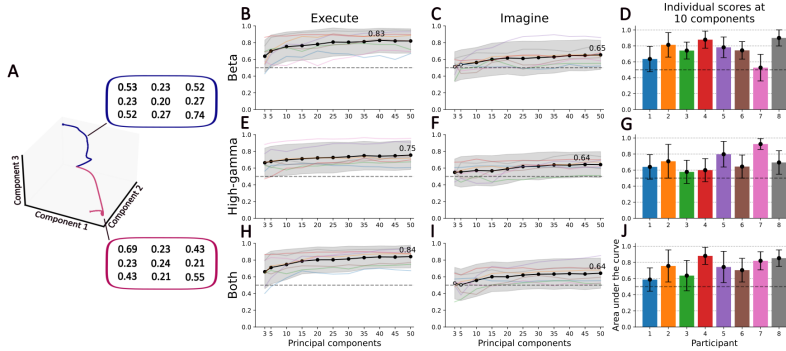
Figure 4.2: Decoder performance. **A**) Representation of the average dynamics of movements and rest in the first three components. Blue (rest) and red (move) boxes illustrate the corresponding covariance matrices. **B** Average decoding performance for executed movements using only beta power. Performance significantly (one sample t-test, $\alpha = 0.05$, false discovery rate corrected) above chance (0.5, black dotted line) is shown by filled circled, non-significant scores are shown as open circles. The annotated number shows the maximum performance. Each colored line is one participant. **C** Same as **B**, but for imagined movement decoding. **D** Decoding performance per participant for executed movements using only beta power and 10 principal components. Error bars show standard deviation over folds. Red dotted line shows chance level (0.5). **E, F, G**) Same as **B, C, D**, respectively, but with high-gamma power. **H, I, J**) Same as **B, C, D**, respectively, but with both beta and high-gamma power.

at 70% of the available channels. The results introduce a trade-off between decoder performance and stability, suggesting that there exists an optimum. Therefore, we calculated the mean performance over all percentages of information loss for each number of principal components, and find a smooth curve with an optimum of $n_{components} = 10$ (Figure 4.3b). Further inspection of the individual scores at the optimum (Figure 4.3c) revealed that the stability found on average holds true for each participant, regardless of their individual performance. While standard deviation increased slightly as expected, the mean performance remains equal or decreases only slightly under increasing loss of information.
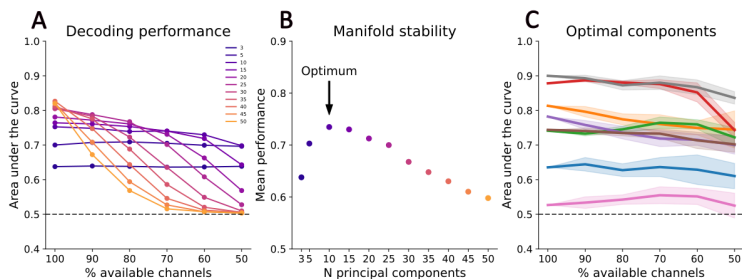
Figure 4.3: Manifold stability. **A**) Decoder performance when information is removed from a percentage of channels. Less components (purple) leads to lower baseline performance that remains stable over information loss, whereas more components (yellow) leads to higher baseline performance, but instability to information loss. **B**) Mean performance over different percentages of information loss, where the optimum is shown at 10 principal components. **C**) Performance per participant for the optimal number of components. Regardless of baseline performance, the performance remains relatively stable with increasing information loss for each participant.

Optimal manifold captures similar information across tasks

Next, we explored whether the stable manifold describes task-specific or broader movement-related information. To test this, we trained our decoder on executed movements and tested it on imagined movements. The decoder reached performance significantly above chance (one sample t-test, $\alpha = 0.05$, FDR corrected) for all components, except using only 3 (Figure 4.4a, black line). Maximum performance was 0.61 ± 0.07 auc at 25 components. Interestingly, cross-task performance is equal to within-task performance (Figure 4.4a, black dashed line), as there is no significant difference between the performances. The performance is similar specifically up to 30 components, after which both start to diverge with an increasing number of principal components.

Optimal manifold captures participant invariant global neural dynamics

To further explore the extend of shared information captured by the manifold, we evaluated the decoding performance on executed movements across participants. We trained our decoder on a source partici-

pant and tested it on each remaining target participant. For 7 out of 8 source participants the decoder was able to decode significantly above chance (one sided t-test, $\alpha = 0.05$, FDR corrected, Figure 4.4b) on average over all target participants using beta power. For the same analysis using high-gamma power, 6 out of 8 participants reached significantly above chance decoding, whereas beta + high-gamma resulted significant decoding in 0 out of 8 participants. While each participant's electrode configuration was quite varied and distributed throughout the brain (Figure 4.1b, Figure 4.4e), nearly all electrode configurations were sufficient to capture similar information across participants on average. Surprisingly, even source-target pairs with barely overlapping electrode configurations were able to achieve good decoding results (Figure 4.4d, e). A closer inspection of the first principal component showed that the variance is significantly lower (independent t-test, $p = 0.001$) during the move trials compared to rest (Figure 4.4c). This suggests that the first component captures beta band desynchronization, as this analysis only uses beta power as input. Inspecting the individual performance values showed that the source-target pairs are not symmetrical: if one participant is a good source, it does not seem to predict that one is a good target as well. For example, the circle shown in Figure 4.4d, shows a high decoding performance as target ($auc = 0.82$), but the reversed direction only shows $auc = 0.54$. Furthermore, it seems that if a participant has good target decoding, they are generally a good target for the other participants (Figure 4.4d, columns). From a source perspective, this is not the case, as the scores vary substantially over participants. Quantitatively, it shows that the standard deviation (std) of the target perspective, that is whether a participant is a good target, is substantially lower than the source perspective: 0.062 ± 0.026 vs 0.096 ± 0.020 (mean $\pm$ std of the std). Taken together, our results suggests that decodable global neural dynamics exist and these dynamics are similar across tasks and across participants.
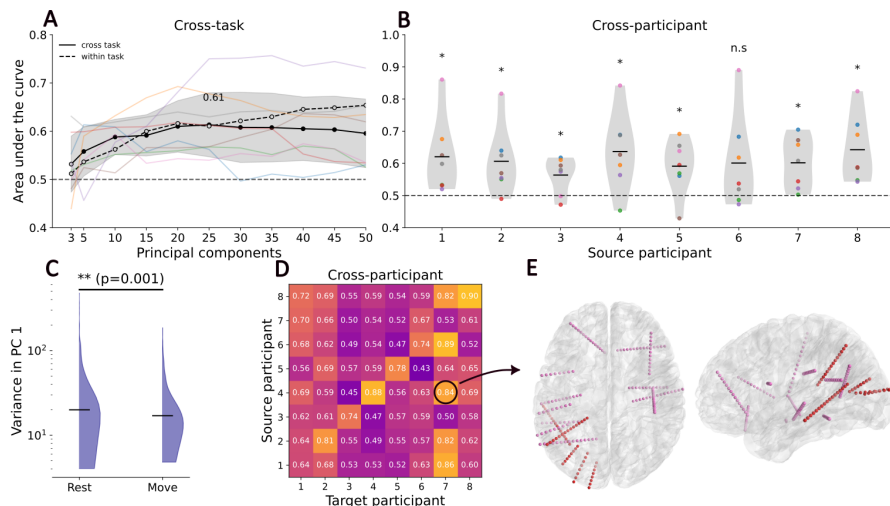
Figure 4.4: Cross-task and cross-participant decoding. **A)** Performance across task, where the decoder is trained on executed movements and tested on imagined movements. For cross-task (filled line) the filled circles represent scores significantly above chance (one sample t-test, $\alpha = 0.05$, FDR corrected), whereas the circles in within tasks (dashed line) shows whether the scores are significantly different then across task (independent t-test, $\alpha = 0.05$, FDR corrected). None of the within task decoding scores are significantly different than across task, although performance starts to increase gradually over cross-task performance with 30 or more principal components. **B)** Decoding performance when trained on a source participant and tested on the remaining target participants. Each color represents a single participant. * shows decoding performance significantly above chance (one sample t-test, $\alpha = 0.05$, FDR corrected). n.s. = not significant. **C)** Distribution of variance in the first components per class. PC = principal component. **D)** Performance matrix for each source-target pair. The diagonal (i.e. source participant 1 vs target participant 1) shows the within participant performance. An example cross-participant performance is highlighted by the circle and arrow, and shows the **E)** electrode configurations of the source (p4, red) and target (p7, pink) participant.

4.3 Discussion

We find a stable low-dimensional manifold underlying global motor activity in sEEG recordings that is predictive for both executed and imagined grasping movements. Any number of components is sufficient to decode executed movement, but we observe that including more components gradually increases performance (Figure 4.2b, e, h). In imagined movements, the decoding performance is significantly above chance from 15 or more components, and the same gradual increase in performance is observed (Figure 4.2c, f, i). However, the ablation study revealed that including too many components decreased the stability of the decoder. The more components included, the faster the performance of the decoder decreased under loss of information (Figure 4.3). Thus, it seems like restricting the number of components increases the generalizability of the decoder and prevents it from fitting dataset specific information. It is challenging to discern whether the increased performance is movement-related information only captured by the participant-specific electrode configuration, or that it increasingly overfits on dataset specific bias or other non-movement related noise.

Our results indicate that there is a performance-stability trade-off (Figure 4.3b) with an optimum of 10 components. Decoding with this optimum reveals a manifold that describes remarkably stable neural dynamics, demonstrating that movement-related activity is captured in a smaller subspace than the original space. For all participants, this manifold remained stable for up to 50% of missing information, regardless of baseline performance. The stability shows that the information must come from multiple sources, suggesting that the manifold captured a distributed network throughout the brain. If a single region or process was mainly driving performance, we would expect that fewer components were required to capture the same information, a larger standard deviation under loss of information, as well as non-significant decoding performance across participants. The distributed network captured by the manifold is even predictive across tasks and across participants with non-overlapping electrode configurations (Figure 4.4a, b), demonstrating that it describes generalizable dynamics. In the cross-task analy-

sis (Figure 4.4a) the decrease in generalizability becomes apparent when adding more components. For up to 25 components, the performance is equal, after which the within-task performance continues to increase and cross-task performance starts to decrease.

Taken together, our results point towards global motor dynamics and are congruent with results reported in other species [2–4], other recording modalities [7], and in human sEEG motor decoding studies decoding from individual brain-wide areas [9–14]. A key difference with the global motor dynamics reported in animals or fMRI is that those are based on spiking activity or hemodynamics, while our results are based on local field potentials. Furthermore, Steinmetz et al. [2] report that a majority of the neurons correlated with movement increased their activity, while a significant minority reduced their activity, highlighting the heterogeneity in responses required to capture the full neural dynamics. In this work, we focused on beta and high-gamma activity because of their known involvement with motor behavior. We found a significant decrease in variation in the first components between move and rest that might indicate a beta desynchronization (Figure 4.4c). Nonetheless, perhaps a broader spectral scope could reveal stronger generalizable dynamics.

Our data reveal some contours of the network. First, the network seems to be global, but not ubiquitous: not all participants reached sufficient decoding performance when using the optimal number of components, (Figure 4.2d, g, j) and some participants seems to be good targets but poor sources for decoding, and vice versa (Figure 4.4b, d). Notably, we observe that the lowest performing participant in executed beta (p7, pink) is the best target for cross-decoding (Figure 4.4). Even more, based on the individual source-target scores, some participants are good targets for all other participants. That means that if a participant is a good target in a source-target pair, then it is likely that the participant is also a good target for the other participants. However, this does not seems to be the case from the source perspective. The varying performance between participants and source-target pairs might also be influenced by non-technical reasons, such as varying engagement, as all our participants are under clinical treatment during our experiments, and often

report tiredness and lack of concentration.

The global motor dynamics may enable us to combine data from multiple participants, regardless of electrode configuration, improving performance of future decoders as well as reducing calibration times. Although the task is simple, detecting movements is an essential part for hierarchical decoders [25, 26]. Moreover, movement detection might be useful for adaptive deep-brain stimulation, where an intended movement might be detected, which subsequently activates stimulation [27]. More speculatively, the revealed global neural dynamics might be able to inform about a disease state [28], where changes in global motor dynamics might reflect disease progression. Future work will be required to disentangle the size and content of the neural dynamics, and explore potential application in new or existing decoders.

4.4 Conclusion

In summary, we have identified decodable global motor-related neural dynamics that is captured by a low-dimensional manifold. This manifold is stable to loss of information, and captures information that is similar across tasks and across participants, even with varying and non-overlapping electrodes. These results are the first demonstration showing decodable brain-wide movement-related neural activity in human electrophysiological recordings, and builds upon studies showing similar brain-wide activity across multiple species. These global dynamics might open up the way for a broader scope for all movement-related neuroscience research, including combining datasets of multiple participants, detection of movements for adaptive stimulation technologies and potentially disease progressions states.

4.5 Methods
Participants

We recorded data from eight epilepsy patients (age 35.8 ± 14.2, mean $\pm$ standard deviation, supplementary data 1). All participants were undergoing presurgical assessment for resection surgery as treatment for their

medication-resistant epilepsy. Each participant was implanted with a varying amount of sEEG electrodes (supplementary data 1) in varying locations (Figure 4.1a, supplementary data 2). All electrode configurations and trajectories were solely based on clinical need and were not influenced in any way by this study. The amount of implanted shafts ranged from 5 to 14 electrodes, containing 42 to 127 recordable contacts.

Ethical approval

The institutional review board of Maastricht University and Epilepsy Center Kempenhaeghe (METC 20180451) approved the experimental protocol. All experiments were in accordance with local guidelines and regulations, and were under supervision of experienced healthcare staff. All participants participated voluntarily and provided written informed consent.

Tasks

Our participants performed an executed and imagined continuous grasping task. In the execution task, they were instructed to open and close their left or right hand continuously, based on visual instruction. Each trial was 3 seconds long, directly followed by a 3 second rest period (Figure 4.1a). Left and right hand were each cued 30 times in pseudorandomized order, resulting in a total of 60 movement trials and 60 rest trials. After a short break, the participants were instructed to imagine performing the previous execution task. The imagined task was always after the execution task. In earlier pilots, participants reported to find it challenging to imagine the movements. Thus, performing the executed task prior to the imagined task provided a fresh memory of the proprioceptive and kinematic experience of the grasping movement. To further aid the participants, the experimenter briefly introduced a kinesthetic and visual strategy [29]. However, the participants were free to use any strategy they felt was most effective. During the imagery task, the experimenter instructed the participants to remain completely still and visually checked whether they adhered to the instruction.

Recordings and electrodes

Participants were implanted with platinum-iridium stereotactic electro-encephalography electrodes (Microdeep intracerebal electrodes; Dixi Medical, Beçanson, France), containing 5 to 18 contacts (2 mm long, 0.8 mm in diameter and 1.5 mm intercontact distance). Neural activity was recorded using two stacked Micromed SD LTM amplifiers (Micromed, S.p.A., Treviso, Italy). All contacts were referenced to a contact in white matter that visually did not show epileptic activity, determined by the epileptologist. Neural data and experimental stimuli were synchronized using LabStreamingLayer [30]. In this work, we refer to electrodes as the full shaft and contact as each recording location on the shaft. Once data is recorded and digitized, we then refer each contact as a channel.

Imaging

We determined the anatomical locations of each contact by coregistering a pre-implantation anatomical T1-weighted MRI scan and post-implantation CT scan. We first parcellated the MRI using Freesurfer (`https://surfer.nmr.mgh.harvard.edu`) and then labeled the anatomical locations according to the Destrieux atlas [31] using img_pipe [32]. To generate a visualization with all electrodes from all participants on a single brain (Figure 4.1a), we warped all brains and corresponding electrode locations to the CVS average-35 atlas in MNI512 space. Note that anatomical locations are always determined in native space.

Electrode coverage

A total of 956 contacts on 82 electrodes covered 59 unique grey matter areas (supplementary data 2). The grey matter areas covered most were the insular sulcus ($n = 25$), superior temporal sulcus ($n = 23$) and middle frontal gyrus ($n = 23$). Most non-grey matter areas were in white matter ($n = 408$) or unknown areas ($n = 100$). The unknown areas could not be labeled due to various reasons, such as the atlas not having a label for a specific location or contacts between brain tissues, e.g. in sulci.

Data preparation

All our analyses were done using `Python 3.9.7` and all code is publicly available on `github.com/mottenhoff/manuscript_glo bal_motor_dynamics`. First, we removed channels without relevant information, such as marker channels and disconnected channels. Then we removed the channel mean and detrended the signal. Lastly, we extracted 3 sets of frequency bands: beta $(12 - 30$ hz), high-gamma $(55 - 90$ Hz) and both. For the combination of both frequency bands, we concatenated the channels per frequency. To acquire the instantaneous power, we band-pass filtered the data using a zero-phase finite impulse response filter and then took the absolute of the hilbert transform. Finally, we split the continuous data into trials, and combine `left` and `right` hand movement trials into a single `move` class.

Decoding

We used a Riemannian classifier, which directly classifies based on the trial covariance matrix [33]. Riemannian approaches have shown to be promising for brain-computer interface applications, given its robustness to outliers and applications in surface EEG [34, 35]. To decode movement from neural activity, we first split the data into training and test data using 10-fold cross validation. On the training data, we z-score the data, fit a principal components analysis (PCA) and transform the data to 3 to 50 principal components (Figure 4.1b). Then, for each trial we estimate a regularized (Ledoit and Wolf [36]) sample covariance matrix and calculate the geometric mean of all covariance matrices of one class using the symmetric Kullback-Leibler divergence [37] (Figure 4.1c). To classify trials in the test set, the learned standardization and filters from the PCA are applied to the test data. Then, for each trial in the test set the same regularized sample covariance matrix is estimated. Next, a prediction is made per trial by the minimum distance to the learned geometric class means (Figure 4.1d). We used the `pyRiemann` package [38] for covariance estimation and decoding.

Manifold stability

To assess whether the extracted low-dimensional representation captures neural dynamics on a stable manifold, we performed an ablation study that removed information from randomly selected channels [39] We progressively removed information by setting all values in randomly selected channels to zero, and then retested our decoder. Baseline performance was defined at 100% of the available channels. We then removed information from 10%, 20%, 30%, 40% and 50% randomly selected channels by setting all values to 0. We then applied the previously described decoding (section 4.5) strategy. Within each fold, we repeated the random channel selection 10 times.

Cross-task and cross-participant decoding

To decode across tasks, we trained our decoder on the full executed dataset, and tested it on the full imagined dataset. The standardization, principal components filters and geometric class means were fitted on the executed data, and then applied to the imagined test data. To decode across participants, the same strategy was used as cross-task decoding, but the training and test set were a source and a target participant.

Evaluation

All decoding scores were evaluated by the area under curve the receiver operator characteristic. To compare the decoding results against chance level ($AUC = 0.5$), we used a one-sample t-test and applied a False Discovery Rate (Benjamin-Hochberg) correction to correct for multiple testing in the main results (Figure 4.2b, c, e, f, h, i) and Figure 4.4a, b).

4.6 Data availability

Data will be made publicly available at publication.

4.7 Code Availability

All code to perform the analyses and to generate the figures are available at `https://github.com/mottenhoff/manuscript_global_`

`motor_dynamics.`

4.8 Competing interests
The authors declare no competing interests.

4.9 Acknowledgements

References
[1]   Misha B. Ahrens et al. "Brain-wide neuronal dynamics during motor adaptation in zebrafish". en. In: *Nature* 485.7399 (May 2012). Number: 7399 Publisher: Nature Publishing Group, pp. 471–477. DOI: `10.1038/nature11057`.

[2]   Nicholas A. Steinmetz et al. "Distributed coding of choice, action and engagement across the mouse brain". en. In: *Nature* 576.7786 (Dec. 2019). Number: 7786 Publisher: Nature Publishing Group, pp. 266–273. DOI: `10.1038/s41586-019-1787-x`.

[3]   Carsen Stringer et al. "Spontaneous Behaviors Drive Multidimensional, Brain-wide Activity". In: *Science* 364.6437 (Apr. 2019), p. 255. DOI: `10.1126/science.aav7893`.

[4]   Peter Zatka-Haas et al. "Sensory coding and the causal impact of mouse cortex in a visual decision". In: *eLife* 10 (July 2021). Ed. by Martin Vinck, Joshua I Gold, and Karel Svoboda. Publisher: eLife Sciences Publications, Ltd, e63163. DOI: `10.7554/eLife.63163`.

[5]   International Brain Lab et al. *A Brain-Wide Map of Neural Activity during Complex Behaviour*. en. Pages: 2023.07.04.547681 Section: New Results. July 2023. DOI: `10.1101/2023.07.04.547681`.

[6]   Simon Musall et al. "Single-trial neural dynamics are dominated by richly varied movements". en. In: *Nature Neuroscience* 22.10 (Oct. 2019). Number: 10 Publisher: Nature Publishing Group, pp. 1677–1686. DOI: `10.1038/s41593-019-0502-4`.

[7]   Javier Gonzalez-Castillo et al. "Whole-brain, time-locked activation with simple tasks revealed using massive averaging and model-free analysis". In: *Proceedings of the National Academy of Sciences* 109.14 (Apr. 2012). Publisher: Proceedings of the National Academy of Sciences, pp. 5487–5492. DOI: `10.1073/pnas.1121049109`.

[8]   Christian Herff, Dean J. Krusienski, and Pieter Kubben. "The Potential of Stereotactic-EEG for Brain-Computer Interfaces: Current Progress and Future Directions". English. In: *Frontiers in Neuroscience* 14 (2020). Publisher: Frontiers. DOI: `10.3389/fnins.2020.00123`.

[9]   Alexander P. Rockhill et al. "Stereo-EEG recordings extend known distributions of canonical movement-related oscillations". en. In: *Journal of Neural Engineering* 20.1 (Jan. 2023). Publisher: IOP Publishing, p. 016007. DOI: 10.1088/1741-2552/acae0a.

[10] Sarah K. Wandelt et al. "Decoding grasp and speech signals from the cortical grasp circuit in a tetraplegic human". en. In: *Neuron* (Mar. 2022). DOI: 10.1016/j.neuron.2022.03.009.

[11] Richard A. Andersen, Tyson Aflalo, and Spencer Kellis. "From thought to action: The brain–machine interface in posterior parietal cortex". In: *Proceedings of the National Academy of Sciences* 116.52 (Dec. 2019). Publisher: Proceedings of the National Academy of Sciences, pp. 26274–26279. DOI: 10.1073/pnas.1902276116.

[12] Guangye Li et al. "Assessing differential representation of hand movements in multiple domains using stereo-electroencephalographic recordings". en. In: *NeuroImage* 250 (Apr. 2022), p. 118969. DOI: 10.1016/j.neuroimage.2022.118969.

[13] Meng Wang et al. "Enhancing gesture decoding performance using signals from posterior parietal cortex: a stereo-electroencephalograhy (SEEG) study". en. In: *Journal of Neural Engineering* 17.4 (Sept. 2020). Publisher: IOP Publishing, p. 046043. DOI: 10.1088/1741-2552/ab9987.

[14] MacAuley Smith Breault et al. "Non-motor Brain Regions in Non-dominant Hemisphere Are Influential in Decoding Movement Speed". In: *Frontiers in Neuroscience* 13.JUL (July 2019), pp. 1–13. DOI: 10.3389/fnins.2019.00715.

[15] Krishna V. Shenoy and Jonathan C. Kao. "Measurement, manipulation and modeling of brain-wide neural population dynamics". en. In: *Nature Communications* 12.1 (Jan. 2021). Number: 1 Publisher: Nature Publishing Group, p. 633. DOI: 10.1038/s41467-020-20371-1.

[16] Omid G. Sani et al. "Modeling behaviorally relevant neural dynamics enabled by preferential subspace identification". en. In: *Nature Neuroscience* 24.1 (Jan. 2021). Number: 1 Publisher: Nature Publishing Group, pp. 140–149. DOI: 10.1038/s41593-020-00733-0.

[17] Xiyuan Jiang et al. "Structure in Neural Activity during Observed and Executed Movements Is Shared at the Neural Population Level, Not in Single Neurons". eng. In: *Cell Reports* 32.6 (Aug. 2020), p. 108006. DOI: 10.1016/j.celrep.2020.108006.

[18] Jonathan A. Michaels, Benjamin Dann, and Hansjörg Scherberger. "Neural Population Dynamics during Reaching Are Better Explained by a Dynamical System than Representational Tuning". en. In: *PLOS Computational Biology* 12.11 (Nov. 2016). Publisher: Public Library of Science, e1005175. DOI: 10.1371/journal.pcbi.1005175.

[19] Sean M. Perkins et al. *Simple decoding of behavior from a complicated neural manifold*. en. Pages: 2023.04.05.535396 Section: New Results. Apr. 2023. DOI: 10.1101/2023.04.05.535396.

[20] Cecilia Gallego-Carracedo et al. "Local field potentials reflect cortical population dynamics in a region-specific and frequency-dependent manner". en. In: *bioRxiv* (May 2021), p. 2021.05.31.446454. DOI: 10.1101/2021.05.31.446454.

[21] Alan D. Degenhart et al. "Stabilization of a brain–computer interface via the alignment of low-dimensional spaces of neural activity". en. In: *Nature Biomedical Engineering* 4.7 (July 2020), pp. 672–685. DOI: 10.1038/s41551-020-0542-9.

[22]   Juan A. Gallego et al. "Cortical population activity within a preserved neural manifold underlies multiple motor behaviors". en. In: *Nature Communications* 9.1 (Oct. 2018). Number: 1 Publisher: Nature Publishing Group, p. 4233. DOI: 10.1038/s41467-018-06560-z.

[23]   Nikhilesh Natraj et al. "Compartmentalized dynamics within a common multi-area mesoscale manifold represent a repertoire of human hand movements". en. In: *Neuron* (Oct. 2021). DOI: 10.1016/j.neuron.2021.10.002.

[24]   Svenja Melbaum et al. "Conserved structures of neural activity in sensorimotor cortex of freely moving rats allow cross-subject decoding". en. In: *Nature Communications* 13.1 (Dec. 2022). Number: 1 Publisher: Nature Publishing Group, p. 7420. DOI: 10.1038/s41467-022-35115-6.

[25]   Sean L. Metzger et al. "Generalizable spelling using a speech neuroprosthesis in an individual with severe limb and vocal paralysis". en. In: *Nature Communications* 13.1 (Nov. 2022). Number: 1 Publisher: Nature Publishing Group, p. 6510. DOI: 10.1038/s41467-022-33611-3.

[26]   Alexandre Moly et al. "An adaptive closed-loop ECoG decoder for long-term and stable bimanual control of an exoskeleton by a tetraplegic". en. In: *Journal of Neural Engineering* 19.2 (Mar. 2022). Publisher: IOP Publishing, p. 026021. DOI: 10.1088/1741-2552/ac59a0.

[27]   Wolf-Julian Neumann et al. "Adaptive Deep Brain Stimulation: From Experimental Evidence Toward Practical Implementation". en. In: *Movement Disorders* n/a.n/a (May 2023). _eprint: https://onlinelibrary.wiley.com/doi/pdf/10.1002/mds.29415. DOI: 10.1002/mds.29415.

[28]   Eleonora Fiorenzato et al. "Dynamic functional connectivity changes associated with dementia in Parkinson's disease". In: *Brain* 142.9 (Sept. 2019), pp. 2860–2872. DOI: 10.1093/brain/awz192.

[29]   Takashi Hanakawa. "Organizing motor imageries". In: *Neuroscience Research* 104 (2016). Publisher: Elsevier Ireland Ltd and Japan Neuroscience Society, pp. 56–63. DOI: 10.1016/j.neures.2015.11.003.

[30]   C Kothe. *Lab Streaming Layer (lsl)*. 2014.

[31]   Christophe Destrieux et al. "Automatic parcellation of human cortical gyri and sulci using standard anatomical nomenclature". eng. In: *NeuroImage* 53.1 (Oct. 2010), pp. 1–15. DOI: 10.1016/j.neuroimage.2010.06.010.

[32]   Liberty S. Hamilton et al. "Semi-automated Anatomical Labeling and Inter-subject Warping of High-Density Intracranial Recording Electrodes in Electrocorticography". English. In: *Frontiers in Neuroinformatics* 11 (2017). Publisher: Frontiers. DOI: 10.3389/fninf.2017.00062.

[33]   Marco Congedo, Alexandre Barachant, and Rajendra Bhatia. "Riemannian geometry for EEG-based brain-computer interfaces; a primer and a review". In: *Brain-Computer Interfaces* 4.3 (July 2017). Publisher: Taylor & Francis _eprint: https://doi.org/10.1080/2326263X.2017.1297192, pp. 155–174. DOI: 10.1080/2326263X.2017.1297192.

[34]   Florian Yger, Maxime Berar, and Fabien Lotte. "Riemannian Approaches in Brain-Computer Interfaces: A Review". In: *IEEE Transactions on Neural Systems and Rehabilitation Engineering* 25.10 (Oct. 2017). Conference Name: IEEE Transactions on Neural Systems and Rehabilitation Engineering, pp. 1753–1762. DOI: 10.1109/TNSRE.2016.2627016.

[35] Alexandre Barachant et al. "Multiclass Brain–Computer Interface Classification by Riemannian Geometry". In: *IEEE Transactions on Biomedical Engineering* 59.4 (Apr. 2012). Conference Name: IEEE Transactions on Biomedical Engineering, pp. 920–928. DOI: 10.1109/TBME.2011.2172210.

[36] Olivier Ledoit and Michael Wolf. "Honey, I Shrunk the Sample Covariance Matrix". en. In: *The Journal of Portfolio Management* 30.4 (July 2004). Publisher: Institutional Investor Journals Umbrella Section: Primary Article, pp. 110–119. DOI: 10.3905/jpm.2004.110.

[37] S. Chevallier et al. "Review of Riemannian Distances and Divergences, Applied to SSVEP-based BCI". en. In: *Neuroinformatics* 19.1 (Jan. 2021), pp. 93–106. DOI: 10.1007/s12021-020-09473-9.

[38] A. Barachant. *pyRiemann v0.2.2*. June 2015. DOI: 10.5281/zenodo.18982.

[39] Richard Meyes et al. *Ablation Studies in Artificial Neural Networks*. arXiv:1901.08644 [cs, q-bio]. Feb. 2019. DOI: 10.48550/arXiv.1901.08644.

4.10 Supplementary material
Participant information

#	Age	Sex	Sample rate	Electrodes	Contacts
1	16	M	2048	14	127
2	47	M	1024	11	127
3	52	M	1024	6	68
4	22	F	1024	5	54
5	20	F	1024	11	117
6	40	M	1024	12	127
7	55	F	1024	12	127
8	34	M	1024	11	115

Supplementary data 1 - Participant information. Age = years, Sample rate = Hz

Supplementary data 2 - Brain regions covered by the implanted electrodes. Each color is a different participant. Note that most contacts are in white matter and unknown areas, as shown in the insets.
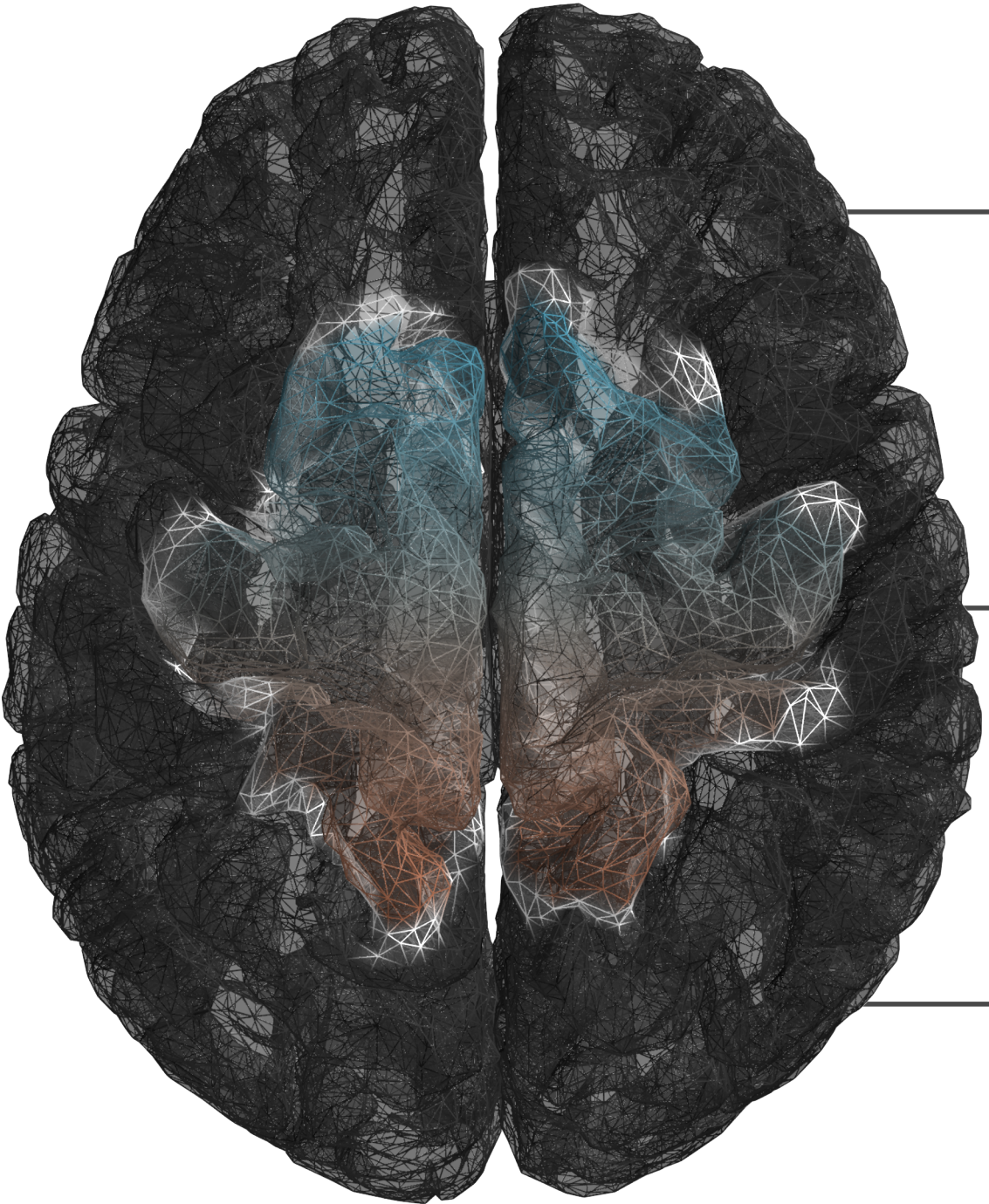
5

Continuous decoding of 3D hand kinematics from distributed brain-wide neural recordings

2023

M.C. Ottenhoff, M. Verwoert, S. Goulis, S. Tousseyn, M. Shanechi, O. Sani, P. Kubben and C. Herff

In preparation

Abstract

Correlation between neural activity and movements can be recorded nearly anywhere in the brain, but the neural contents of these global motor dynamics are still unknown. Decoding motor-related activity using distributed brain-wide neural recordings may shine light on global motor dynamics, but studies so far have used simple trial-based task-designs. To capture the full complexity of motor control, continuous decoding designs aimed at decoding more complex movements are necessary. Therefore, we designed a continuous hand tracking experiment and demonstrate successful decoding of 3D hand kinematics from distributed recordings. In this study, we included 16 participants implanted with stereotactic electroencephalographic electrodes, providing a sparse but brain-wide coverage. We designed a gamified 3D movement tasks and recorded continuous hand movement trajectories using a motion tracker. We extracted delta activity, alpha-beta power and broadband high-gamma power, and trained a preferential subspace identification model to predict the trajectories of 12 hand movement parameters. We were able to reconstruct non-directional hand speed and acceleration significantly above chance, where delta activity was most predictive with an average hand speed reconstruction correlation of 0.39 ± 0.20 (mean, std) and maximum of 0.75 ± 0.05. The decoder was able to reconstruct movement speed for any frequency input for all participants, regardless of electrode placement. Furthermore, we show strong correlations (both positive and negative) between delta activity and hand movement speed across the brain. The results indicate that non-direction movement kinematics are represented throughout the brain, expanding on earlier work on global motor dynamics. Our results highlight that delta phase information is strongly related to continuous hand movement control. Furthermore, sEEG may have untapped potential for online motor decoders on distributed recordings, and studies could uncover more recording targets for new and existing decoders.

5.1 Introduction

Movement-related neural activity is more widespread than was previously thought. High correlations throughout the animal brain between neural activity and movement are consistently being reported in zebrafish, and mice [1–3]. In humans, motor-related neural activity can be decoded from many different individual non-motor brain regions as well [4–11]. Previous work extended these findings of decoding individual regions by extracting a neural manifold from all recorded areas, and revealed that there exist global motor dynamics that are predictive across tasks and across participants with non-overlapping electrodes [12]. These studies all leverage the unique opportunity provided by stereotactic-encephalography (sEEG) electrodes [13], usually implanted in medication-resistant epilepsy patients. The electrode configurations cover the whole brain when combined over patients, enabling investigations of global motor activity.

So far, most sEEG studies are based on highly controlled trial-based experimental paradigms, and usually involve decoding of a small set of individual movements (e.g. finger flexion or different grasp types). While simple decoding designs has proven to effective in clinical BCIs [14], they impose a limit on the maximum complexity of control. To provide the full range of motor control to clinical brain-computer interfaces, experiments need to transition towards continuous decoding designs that specifically target more complex motor tasks. To date, few studies demonstrated continuous motor decoding using sEEG. Wu et al. (2022) were able to decode continuous force per trial with mean squared errors rates ranging from 0.05 to 0.35, depending on the decoder [15]. Bouton et al. (2021) [16] and Breault et al. (2019) [17] demonstrated trial-based continuous classification of hand flexion tasks and speed levels. Lastly, Shah et al. (2018) [18] demonstrated continuous decoding of force from the subthalamic nucleus with a reconstruction correlation up to 0.76. These results corroborate the possibility of continuous decoding from distributed recordings, although no decoding paradigm in sEEG has targeted a comprehensive overview of continuous decoding of hand-kinematics.

When broadening the scope to other local field potential (LFP) recording modalities (e.g. electrocorticography, ECoG), more evidence shows that continuous motor activity can be decoded from a variety of cortical areas. An important caveat in the context of distributed recordings it that nearly all ECoG studies target the motor cortex, which is rarely captured by sEEG implantations. Jerbi et al. report in their review that there is strong evidence that direction is encoded in M1 in low frequencies and spiking activity [19]. This low frequency component was named by Schalk et al. (2007) [20], who demonstrated the feasibility to use ECoG (i.e. LFPs) to decode 2D movement trajectories in a circular tracking task. The authors coined the term Local Motor Potential (LMP), which effectively is low-pass filtered ($< 5Hz$) neural activity. Combrisson et al. (2023) [10] decoded direction using sEEG and highlighted the importance of low-frequency phase ($< 1.5Hz$) as well.

The evidence so far leads us to hypothesize that continuous and more complex movements can be decoded from distributed recordings. To test this hypothesis, we recorded data from 16 epilepsy patients, covering 117 unique brain areas with 1520 contacts, and continuously decoded 12 different hand kinematics in a 3D hand movement task. Because of the relevance of low frequency phase, we included delta activity instead of power. Additionally, we use alpha-beta power and broadband high-gamma power, and trained a preferential subspace identification model [21] to decode 3D hand kinematics. The decoder was able to reconstruct non-directional hand kinematics for nearly all participants. Our results show that continuous non-directional control is strongly related to the low-frequency component. Moreover, we highlight that the highest correlations between channels and kinematics are distributed throughout the brain, further corroborating the distributed nature of motor-related neural activity.

5.2 Methods

Participants

We included 16 epilepsy patients implanted with stereotactic-encephalographic (sEEG) electrodes. All participants were under treatment for

medication-resistant epilepsy and undergoing an assessment period in preparation for resection surgery. Each participant was implanted with 5 to 14 electrodes, resulting in a total of 135 electrodes and 1520 recordable contacts over all participants. The implantation locations were determined solely by their clinical need, and were not influence in any way by this study.

Ethical Approval

The experimental protocol was approved by the institutional review board Maastricht University and Epilepsy Center Kempenhaeghe (METC20180451). All experiments were in accordance with local guidelines and regulations, and were under supervision of experience healthcare staff. All participants joined the study voluntarily and provided written informed consent.

Experiment

We developed a continuous 3D movement task where the participant had to capture targets on screen by moving the cursor to the target position (Figure 5.1f, i). The cursor was controlled by moving their preferred hand above a motion tracker. The tracker fitted a hand model on an infrared video of the hand. The coordinates of the hand palm were then translated from the tracker coordinate system to the experiment coordinate system, allowing the cursor to be moved. The x and y axis were left-right and up-down, respectively. The z-axis was forward-backward movement and changed the size of the cursor. In this way, the 3D space could be transformed to a 2D representation on screen. The smaller the cursor, the farther away the cursor was, thus the more forward the hand. If the hand of the participant was out of view for more than one second (more specifically, the tracker was not able to fit a hand model), the experiment paused and showed a red circle in the middle of the screen. To continue the experiment, the participant had to hold the cursor on the circle for one second. The experiment would then continue with the same target as before the hand went out of view. This also allowed the participant to take a break, as for some participants prolonged lifting of the arm was

tiresome.

To capture a target, the participant had to match the size of the cursor to the size of the target and hold it at that location for 1 second. If the cursor was on target (i.e. matching the size of the target) the cursor turned green. When the target was successfully captured, a new target immediately appeared on screen. The locations of the targets where placed such that the distances between locations where uniformly distributed. To make the task more engaging for our participants, we changed the visual elements into an underwater world, where a pufferfish (the cursor) had to pop the bubbles (targets). Each run included 50 targets. We captured as much data per participant as recording time and participant ability allowed. For quick and skillful participant, we were able to do multiple runs.

Data recordings

Participants were implanted with platinum-iridium sEEG electrodes (Microdeep intracerebral electrodes; Dixi Medical, Beçanson, France), where each electrodes contained 5 to 18 contacts. The contacts were 2mm long, 0.8mm in diameter and had an intercontact distance of 1.5mm. The neural activity was recorded using two stacked Micromed SD LTM amplifiers (Micromed, S.p.A., Treviso, Italy). Contacts were referenced by the epileptologist, who selected a contact in white matter that visually did not show epileptic activity. Throughout this work, we refer to electrode as the complete shaft, contact as the physical recording location on the shaft, and channel as the digitized data from a single contact. We recorded hand movements by using the UltraLEAP motion tracker (Ultraleap Limited, Bristol, England). The tracker records data varying sample rate (effective frame rate = 65 ± 14 Hz). Neural data, stimuli and hand tracking data were synchronized and recorded using T-Rex [22] and LabStreamingLayer [23].

Imaging & Visualisation

The anatomical locations of each contact were determined by coregistering a pre-implantation anatomical T1-weighted MRI scan with a

post-implantation CT scan. We parcellated the MRI using Freesurfer
(`https://surfer.nmr.mgh.harvard.edu/`) and labeled the
anatomical locations using img_pipe [24] according to the Destrieux at-
las [25]. All anatomical locations and brain renderings are constructed in
native space. In visualizations that require multiple electrode configura-
tions to be shown in a single brain, the electrodes are warped to the CVS
average-35 atlas in MNI512 space. The visualisations in Figure 5.1, 5.2
and 5.3d-f are based on perceptually uniform and color-vision deficiency
friendly colormaps developed by Crameri F. (2018) [26, 27].

Electrode coverage
In total 1520 recordable contacts covered 117 unique brain areas per De-
strieux atlas (Figure 5.1a). Most contacts where in left (463) or right (354)
white matter or labeled as unknown (102). Locations labeled as unknown
could not be labeled due to a variety of reasons, including electrodes not
entirely in the brain, electrodes in ressected areas or contacts between
brain tissues, for example in sulci. The most covered grey matter areas
were left hippocampus (36), superior temporal sulcus (24) and frontal su-
perior gyrus (23).

Data preparation
To prepare the recorded data for our decoder, we applied the following
steps: First, we removed irrelevant channels (e.g. empty marker chan-
nels) and applied a common electrode reference to the neural data. This
sEEG specific rereferencing scheme removes the average activity of the
contact from one electrode from each contact.. Then, the data was fil-
tered (finite impulse response filter using a hamming window, imple-
mented by the MNE python package) to extract delta, alpha-beta and
broadband high-gamma activity, using the following parameters: 1) a
low-pass filter < 5Hz, 2) a band pass filter from 8 to 30 Hz or 3) a band
pass filter from 55 to 200 Hz. For alpha-beta and broadband high-gamma,
we calculated the instantaneous power using a Hilbert transform.

   The hand tracking data and neural data were sampled at different
rates, and had to be aligned. First, the hand tracking data were split into

subsets, based on identified gaps in the tracking data (i.e. when the hand was out of view)). For each subset, we interpolated the hand tracking data to the same sample rate as the neural data. Then, we calculated the velocity and acceleration by differentiating the position, and extracted the non-directional velocity (speed) and acceleration by taking the norm of the directional components. Finally, we windowed the neural data and hand tracking data using 300ms long window and a 50ms window shift. The resulting windows from all subsets were then concatenated into a single dataset. If multiple runs were recorded for one participant, the same algorithm was applied and the different runs were concatenated as well.

Decoder

To continuously decode hand kinematics, we trained a preferential subspace identification (PSID) algorithm (Figure 5.1d) [21]. PSID extracts behaviorally relevant dynamics that are shared between behavior and neural activity, by projecting future behavior onto past neural activity. Using these latent dynamics, a Kalman filter predicts the movement trajectories based on new neural activity (see [21] for an extensive description of PSID). PSID requires three parameters to be set: Number of latent states N_x, number of behaviorally relevant states N_1 and the horizon i. If N_x and N_1 are different, then the remaining states (N_x - N_1) will capture the behaviorally irrelevant dynamics, that is, neural dynamics that are not related to movements. Since we were not interested in behaviorally irrelevant dynamics, we kept N_x and N_1 the same. First, we split the dataset using 5-fold cross-validation. Then, we selected the 30 channels with the highest summed correlation between the channels and all hand kinematics on the training set. To find the optimal PSID parameters, we split the training set using an 4-fold inner cross-validation, on which we performed an exhaustive grid search over $N_1 = [3, 5, 10, 20, 30]$ and $i = [5, 10, 25, 50]$. The parameter set with the highest average performance over the inner cross-validation was selected and used to train and test the model on the train and test set of the outer cross-validation. The performance was evaluated by the reconstruction correlation, that is, the
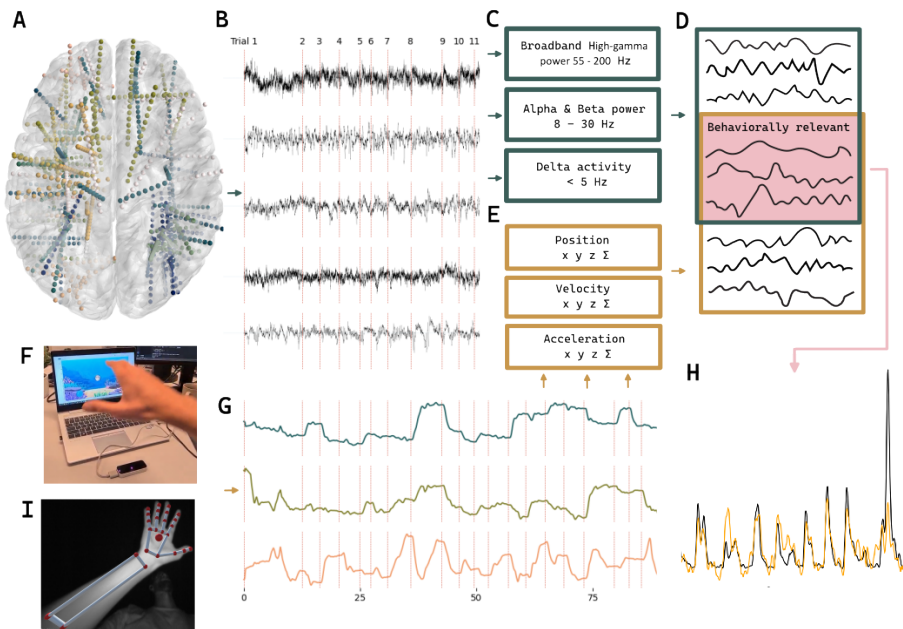
Figure 5.1: **A**) Electrode configurations for all participant warped onto an average brain. Each color represents the implantations for one participant. **B**) Raw EEG data labeled per trial. **C**) Frequency components extracted from the EEG. Delta activity is extracted by a low pass filter of 5 Hz. To extract alpha-beta and broadband high-gamma as band pass filter (8-30 and 80-200 Hz, respectively) and Hilbert transform was used. **D**) A PSID algorithm is used, which extract behaviorally relevant states. **E**) 12 Hand kinematics are extract from the 3D hand trajectories. The x, y, z coordinates of position, velocity and acceleration and the norm of each vector. **F**) (top) Gamified experiment used, a cursor (represented as a pufferfish) is controlled by a leap motion controller. The participant needed to acquire targets (represented as blue bubbles) by moving their hand to the position of the bubble. Depth coordinates (forward - backward) was represented as an increase or decrease of the cursor size. (bottom) The Leap Motion fits a hand model on images of the hand. The hand palm was used to control the cursor. **G**) 3D hand coordinates are recorded by the leap. The data is synchronized with the neural data (in **B**) using LabStreamingLayer. **H**) PSID reconstructs hand kinematics based on the extracted behaviorally relevant states (see panel **D**).

correlation between the actual behavior and the predicted behavior.

Chance level

To calculate whether the decoder is able to predict the kinematics better than chance, we performed a permutation test with 10.000 permutations. We randomly split the reconstructed kinematics between 10% and 90% of the time course, and then switched the two parts around. This way the temporal structure remains intact. Then, we calculated the correlation between the permuted reconstructed kinematics and the true kinematics. Finally, we determined chance level by the 95th percentile of the permuted correlations.

5.3 Results

We recorded 623 ± 322 seconds (mean, std) of data over 16 participants, capturing 95 ± 66 targets, leading to a total of 2 hours and 46 minutes of recorded data and 1512 targets. The participants completed each trial with varying speed, with a median of 3.4 seconds (Figure 5.2a). All participants were able to perform the experiment after a brief practice session or explanation. Based on observation, the general movement pattern between two targets was a large movement to the general location, followed by smaller corrections to adjust to the target position (Figure 5.2b, c). Usually the final correction was most prominent in r_z. The electrode configurations over all participants covered the whole brain (Figure 5.1a).

On average, $\vec{v}$ and $\vec{a}$ could be reconstructed significantly above chance for delta activity, alpha-beta power and broadband high-gamma power (Figure 5.2d). Delta activity was most predictive for $\vec{v}$ (0.39 ± 0.20 correlation coefficient, cc), followed by broadband high gamma. Alpha-beta (0.26 ± 0.14 cc) power performed worse than both delta activity and broadband high-gamma (0.36 ± 0.15 cc), but was still significantly above chance. The performance in $\vec{a}$ was generally lower than $\vec{v}$, but the same ratio between the frequency components was seen: (delta: 0.32 ± 0.20 cc, alpha-beta: 0.21 ± 0.14 cc and broadband high gamma: 0.32 ± 0.15 cc). For $\vec{r}$ (0.06 ± 0.14) cc and all directional kinematics ($r_x = 0.05 \pm 0.14$, $r_y = 0.02 \pm 0.19$, $r_z = 0.09 \pm 0.17$), the decoder was rarely able to reconstruct

the trajectory significantly above chance (Figure 5.2d). Only delta activity was sufficient for the decoder to reconstruct a directional hand speed above chance (v_x: 0.16 ± 0.13cc, v_y: 0.13 ± 0.11 cc, v_z: 0.23 ± 0.15 cc), although the reconstruction correlation remained low.

Zooming in on $\vec{v}$ and $\vec{a}$, decoder was consistently able to decode $\vec{v}$ above chance for all participants and all frequency inputs. For $\vec{a}$ this was true as well, except for three participant/frequency input combinations. Overall, the decoder was able to reconstruct $\vec{v}$ best using delta activity, with the highest performance reaching 0.75 ± 0.05 cc.

The best decodable kinematics, $\vec{v}$, is correlated throughout the brain. For delta activity, the strongest correlations, both positive (up to 0.69) and negative (down to -0.59) are found in many different brain areas (Figure 5.3a). The locations of the strongest correlations are bilateral and do not seem to converge to one or multiple regions. Deeper regions are highly correlated as well. For alpha-beta power, the general channel correlations were weaker (-0.35 to 0.17), and the negative correlations are wide-spread. Broadband high-gamma correlations were mostly positive (-0.16 to 0.41) and more localized than delta or alpha-beta frequencies. Deeper areas showed notable correlations as well.
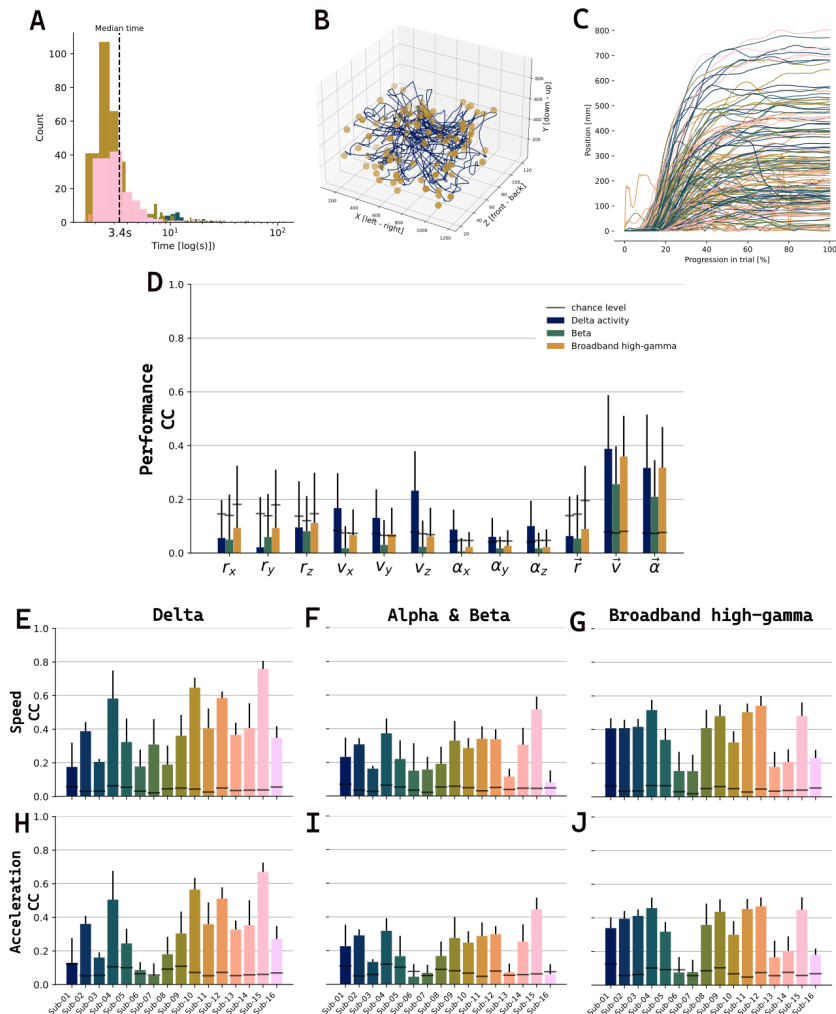
Figure 5.2: **A**) Average time to completion, colored by participant. **B**) Hand movement trajectory (blue) successfully capturing 100 targets (gold circles). **C**) Trajectories per trial for one participant. **D**) Mean performance per kinematic per frequency input. Only the non-directional derivatives speed $\vec{v}$ and acceleration $\vec{a}$ could be reconstructed significantly above chance level (95th percentile of 10.000 permutations.) **E**) Best reconstruction correlation ($\vec{v}$) per participant for delta activity. **F**) Same as **F**, but for alpha-beta power. **G**) Same as **F**, but for broadband high-gamma power. **H**) Best reconstruction correlation for $\vec{a}$ per participant for delta activity. **I**) Same as **I**, but for alpha-beta power. **J**) Same as **I**, but for broadband high-gamma power.
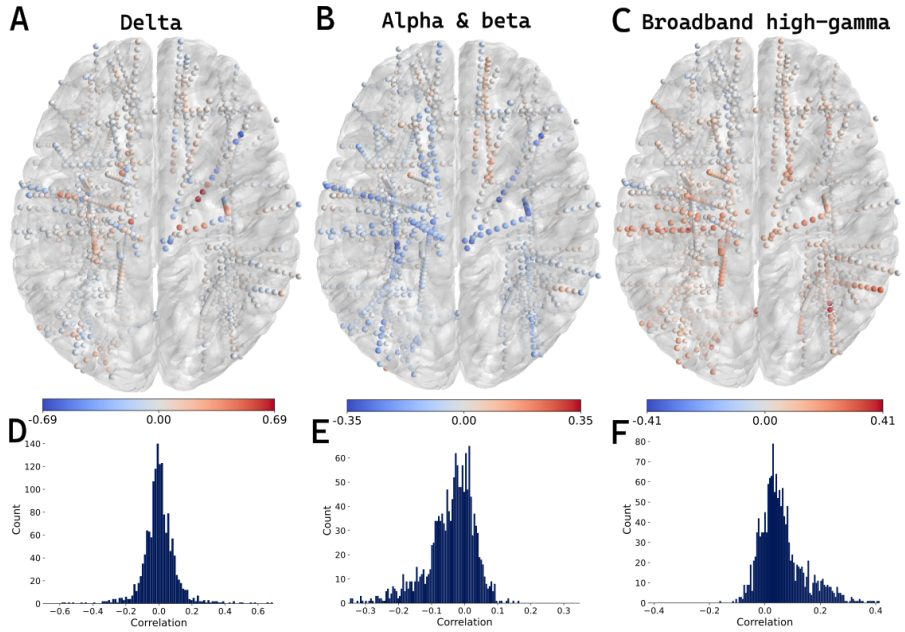
Figure 5.3: Correlations between frequency inputs per channel and $\vec{v}$. All electrode configurations are warped onto an average brain. For one participant the warped electrodes were not available. Colorscales are made symmetrical based on the highest absolute value. The limits of the histogram x-axes are equal to the color bars. **A**) Correlation between delta activity and $\vec{v}$. **B**) Correlation between alpha-beta and $\vec{v}$. **C**) Correlations between broadband high-gamma and $\vec{v}$. **D**) Histogram of channel correlations between delta activity and $\vec{v}$. **E**) Histogram of channel correlations between alpha-beta activity and $\vec{v}$. **F**) Histogram of channel correlations between broadband high-gamma activity and $\vec{v}$.

5.4 Discussion

Non-directional movement kinematics can be reconstructed from areas throughout the brain. Hand movement speed ($\vec{v}$) and acceleration ($\vec{a}$) can be reconstructed significantly above chance using delta activity, alpha-beta and broadband high-gamma power, where acceleration reconstruction correlation was slightly lower than speed.

We were able to reconstruct speed significantly above chance for all frequency components and participants. This means that regardless of implantation, all electrode configurations in our dataset capture enough information to reconstruct continuous hand movement speed, albeit with high variation between participants. This is in line with previous work [12], where we demonstrated that there exists stable global motor dynamics predictive across tasks and participants. Here, we extend the simple trial-based move-no-move task to continuous speed reconstructions, showing that the global motor dynamics relate to online motor control.

The results clearly show that our decoder was not able to reconstruct any directional kinematics, as most directional kinematics did not reach above chance reconstruction. Only the three velocity directions (v_x, v_y and v_z) reached above chance decoding, but with much lower correlation than its non-directional counterpart. While it seems like directionality is mostly encoded in the primary motor cortex [19], one sEEG study reports directional representation based on a trial-based center-out task [10]. The authors demonstrate classification scores ranging from 44% to > 80%, using similar frequency inputs as used in this work. Other similar (but not sEEG) studies [28, 29] also report a directional component in neural activity from non-motor areas, using a trial-based center-out task as well. The apparent discrepancy between these studies can be explained by the difference in paradigm. In this work, we use a less controlled and more naturalistic continuous trajectory decoding task, as opposed to the trial-based center-out paradigm. The directional neural representations reported in the center out-task might not be strong enough to be captured in the continuous data stream (in this case 300ms window length, with 50ms window shift. We believe that this highlights the imperative to move to continuous, naturalistic tasks in the context

of BCI research.

The most informative frequency component was low frequency information (delta activity, $< 5Hz$), followed by broadband high-gamma power ($55 - 200Hz$). The low frequency component correlated strongly with movement behavior in both negative and positive direction. The importance of a low-frequency component for continuous decoding has already been described in the motor cortex as the LMP [20], and our results extent the presence of the LMP to brain-wide areas. Broadband high-gamma power was mostly positively correlated with movement behavior, which has been associated with force control [15, 30].

In our decoding pipeline, channels are selected based on summed correlation with all hand kinematics. This might exclude some channels that are correlated with one specific parameter, but not with all others. Thus, perhaps some directional components are represented, but not captured by our pipeline. However, the low overall reconstructions make it unlikely that a channel strongly correlated with a specific kinematic is not in the 30 most correlated channels. Furthermore, position is currently based on the coordinates system of the bubble experiment space. A better representation might be a coordinate system that is centered on the individual, for example setting the center of the coordinate system to the eyes or body the participant. This does require a measurement of that position, which is not captured in this experiment.

5.5 Conclusion

In summary, we show for the first time that continuous non-directional hand-kinematics can be decoded from distributed brain-wide sEEG recordings, and demonstrate that hand speed trajectories can be decoded regardless of electrode configuration. We expand on previous work that motor related activity is widespread, and contains enough information for continuous hand speed or acceleration. While neural information related to direction seems to be limited to the motor cortex or only weakly represented throughout the brain, our results provide evidence that non-motor areas are essential targets for improved BCI control.

References

[1] Nicholas A. Steinmetz et al. "Distributed coding of choice, action and engagement across the mouse brain". en. In: *Nature* 576.7786 (Dec. 2019). Number: 7786 Publisher: Nature Publishing Group, pp. 266–273. DOI: 10.1038/s41586-019-1787-x.

[2] Peter Zatka-Haas et al. "Sensory coding and the causal impact of mouse cortex in a visual decision". In: *eLife* 10 (July 2021). Ed. by Martin Vinck, Joshua I Gold, and Karel Svoboda. Publisher: eLife Sciences Publications, Ltd, e63163. DOI: 10.7554/eLife.63163.

[3] International Brain Lab et al. *A Brain-Wide Map of Neural Activity during Complex Behaviour*. en. Pages: 2023.07.04.547681 Section: New Results. July 2023. DOI: 10.1101/2023.07.0 4.547681.

[4] Alexander P. Rockhill et al. "Stereo-EEG recordings extend known distributions of canonical movement-related oscillations". en. In: *Journal of Neural Engineering* 20.1 (Jan. 2023). Publisher: IOP Publishing, p. 016007. DOI: 10.1088/1741-2552/acae0a.

[5] Sarah K. Wandelt et al. "Decoding grasp and speech signals from the cortical grasp circuit in a tetraplegic human". en. In: *Neuron* (Mar. 2022). DOI: 10.1016/j.neuron.2022.03 .009.

[6] Richard A. Andersen, Tyson Aflalo, and Spencer Kellis. "From thought to action: The brain–machine interface in posterior parietal cortex". In: *Proceedings of the National Academy of Sciences* 116.52 (Dec. 2019). Publisher: Proceedings of the National Academy of Sciences, pp. 26274–26279. DOI: 10.1073/pnas.1902276116.

[7] Guangye Li et al. "Assessing differential representation of hand movements in multiple domains using stereo-electroencephalographic recordings". en. In: *NeuroImage* 250 (Apr. 2022), p. 118969. DOI: 10.1016/j.neuroimage.2022.118969.

[8] Meng Wang et al. "Enhancing gesture decoding performance using signals from posterior parietal cortex: a stereo-electroencephalograhy (SEEG) study". en. In: *Journal of Neural Engineering* 17.4 (Sept. 2020). Publisher: IOP Publishing, p. 046043. DOI: 10.1088/1741-25 52/ab9987.

[9] MacAuley Smith Breault et al. "Non-motor Brain Regions in Non-dominant Hemisphere Are Influential in Decoding Movement Speed". In: *Frontiers in Neuroscience* 13.JUL (July 2019), pp. 1–13. DOI: 10.3389/fnins.2019.00715.

[10] Etienne Combrisson et al. *Local field potentials in human motor and non-motor brain areas encode the direction of upcoming movements: An intracerebral EEG classification study*. en. Pages: 2023.09.07.556727 Section: New Results. Sept. 2023. DOI: 10.1101/2023.09.07.5567 27.

[11] Brian A. Murphy et al. "Contributions of subsurface cortical modulations to discrimination of executed and imagined grasp forces through stereoelectroencephalography". In: *PLoS ONE* 11.3 (2016), pp. 1–21. DOI: 10.1371/journal.pone.0150359.

[12] Maarten C. Ottenhoff et al. *Global motor dynamics - Invariant neural representations of motor behavior in distributed brain-wide recordings*. July 2023. DOI: 10.1101/2023.07.07.5481 22.

[13] Christian Herff, Dean J. Krusienski, and Pieter Kubben. "The Potential of Stereotactic-EEG for Brain-Computer Interfaces: Current Progress and Future Directions". English. In: *Frontiers in Neuroscience* 14 (2020). Publisher: Frontiers. DOI: 10.3389/fnins.2020.00 123.

[14] Mariska J. Vansteensel et al. "Fully Implanted Brain–Computer Interface in a Locked-In Patient with ALS". In: *New England Journal of Medicine* 375.21 (Nov. 2016). Publisher: Massachusetts Medical Society _eprint: https://doi.org/10.1056/NEJMoa1608085, pp. 2060–2066. DOI: `10.1056/NEJMoa1608085`.

[15] Xiaolong Wu et al. "Decoding Continuous Kinetic Information of Grasp from Stereo-electroencephalographic (SEEG) Recordings". en. In: *Journal of Neural Engineering* (2022). DOI: `10.1088/1741-2552/ac65b1`.

[16] Chad Bouton et al. "Decoding Neural Activity in Sulcal and White Matter Areas of the Brain to Accurately Predict Individual Finger Movement and Tactile Stimuli of the Human Hand". In: *Frontiers in Neuroscience* 15 (2021).

[17] Macauley Smith Breault et al. "Neural Correlates of Internal States that Capture Movement Variability". In: *2019 41st Annual International Conference of the IEEE Engineering in Medicine and Biology Society (EMBC)*. ISSN: 1558-4615. July 2019, pp. 534–537. DOI: `10.1109/EMBC.2019.8856778`.

[18] Syed Ahmar Shah et al. "Towards Real-Time, Continuous Decoding of Gripping Force from Deep Brain Local Field Potentials". In: *IEEE Transactions on Neural Systems and Rehabilitation Engineering* 26.7 (2018). Publisher: IEEE, pp. 1460–1468. DOI: `10.1109/TNSRE.2018.2837500`.

[19] K. Jerbi et al. "Inferring hand movement kinematics from MEG, EEG and intracranial EEG: From brain-machine interfaces to motor rehabilitation". en. In: *IRBM*. NUMÉRO SPÉCIAL : LE CERVEAU DANS TOUS SES ÉTATS 32.1 (Feb. 2011), pp. 8–18. DOI: `10.1016/j.irbm.2010.12.004`.

[20] G. Schalk et al. "Decoding two-dimensional movement trajectories using electrocorticographic signals in humans". en. In: *Journal of Neural Engineering* 4.3 (June 2007), p. 264. DOI: `10.1088/1741-2560/4/3/012`.

[21] Omid G. Sani et al. "Modeling behaviorally relevant neural dynamics enabled by preferential subspace identification". en. In: *Nature Neuroscience* 24.1 (Jan. 2021). Number: 1 Publisher: Nature Publishing Group, pp. 140–149. DOI: `10.1038/s41593-020-00733-0`.

[22] Joaquin Amigo-Vega et al. *T-Rex: sTandalone Recorder of EXperiments; An easy and versatile neural recording platform*. Oct. 2022. DOI: `10.1101/2022.10.26.513822`.

[23] C Kothe. *Lab Streaming Layer (lsl)*. 2014.

[24] Liberty S. Hamilton et al. "Semi-automated Anatomical Labeling and Inter-subject Warping of High-Density Intracranial Recording Electrodes in Electrocorticography". English. In: *Frontiers in Neuroinformatics* 11 (2017). Publisher: Frontiers. DOI: `10.3389/fninf.2017.00062`.

[25] Christophe Destrieux et al. "Automatic parcellation of human cortical gyri and sulci using standard anatomical nomenclature". eng. In: *NeuroImage* 53.1 (Oct. 2010), pp. 1–15. DOI: `10.1016/j.neuroimage.2010.06.010`.

[26] Fabio Crameri. *Scientific colour maps*. Language: eng. June 2023. DOI: `10.5281/zenodo.8035877`.

[27] Fabio Crameri, Grace E. Shephard, and Philip J. Heron. "The misuse of colour in science communication". en. In: *Nature Communications* 11.1 (Oct. 2020). Number: 1 Publisher: Nature Publishing Group, p. 5444. DOI: `10.1038/s41467-020-19160-7`.

[28] Seyyed Moosa Hosseini and Vahid Shalchyan. "Continuous Decoding of Hand Movement From EEG Signals Using Phase-Based Connectivity Features". In: *Frontiers in Human Neuroscience* 16 (2022).

[29] Aysegul Gunduz et al. "Differential roles of high gamma and local motor potentials for movement preparation and execution". In: *Brain-Computer Interfaces* 3.2 (Apr. 2016). Publisher: Taylor & Francis _eprint: https://doi.org/10.1080/2326263X.2016.1179087, pp. 88–102. DOI: 10.1080/2326263X.2016.1179087.

[30] Mariana P. Branco et al. "High-frequency band temporal dynamics in response to a grasp force task". eng. In: *Journal of Neural Engineering* 16.5 (Aug. 2019), p. 056009. DOI: 10.1088/1741-2552/ab3189.

5.6 Supplementary material

Figure 5.4: Anatomical locations covered by the electrode configurations of all participants. The insets show the contacts labeled as white matter or unknown.
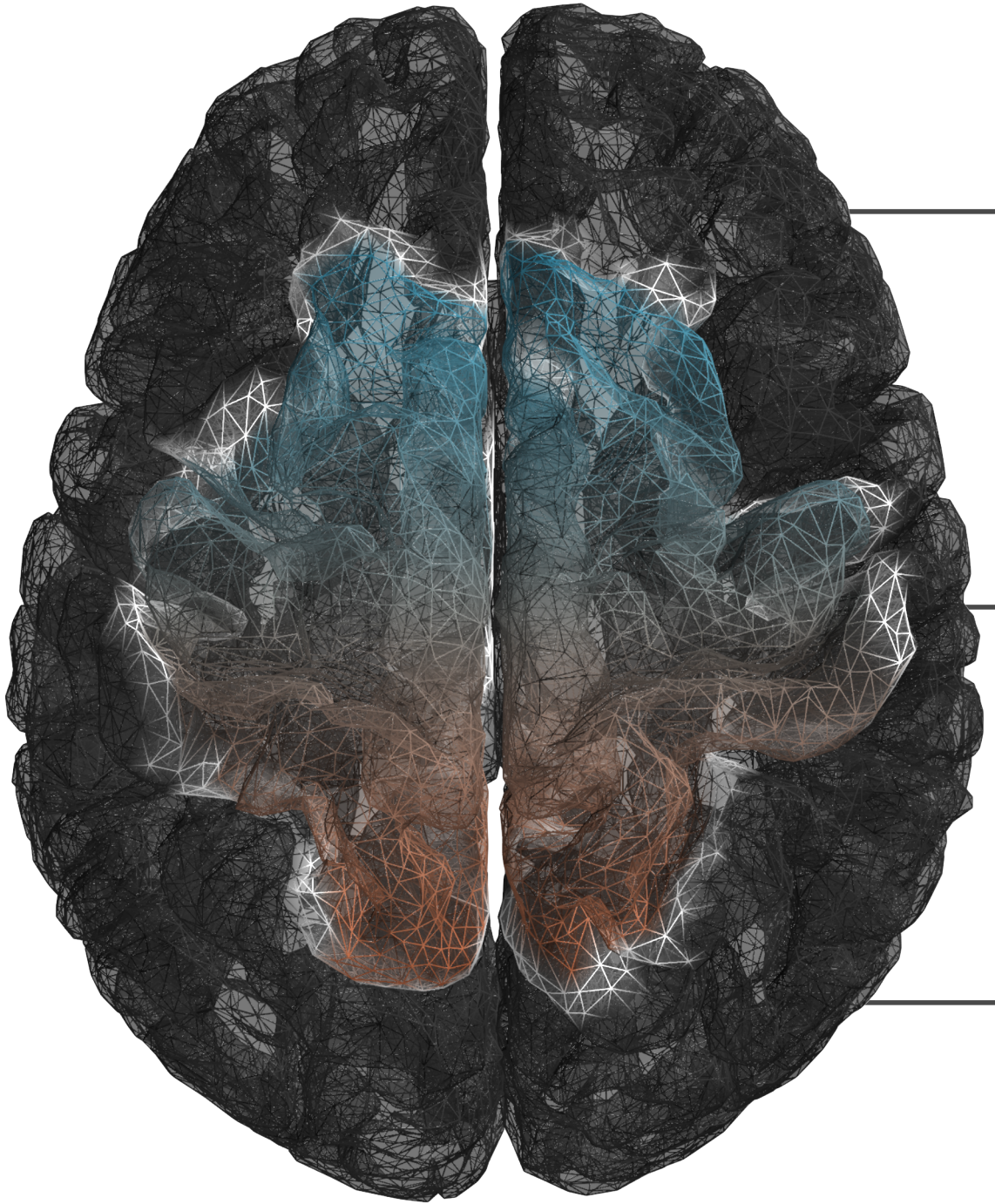
6

An Easy and Versatile Neural Recording Platform T-Rex (sTandalone Recorder of EXperiments): Design and Development Study

2023

J. Amigó-Vega*, M.C. Ottenhoff*, M. Verwoert, P. Kubben and C. Herff

* Both authors contributed equally

Abstract

Background: Recording time in invasive neuroscientific research is limited and must be used as efficiently as possible. Time is often lost due to a long setup time and errors by the researcher, driven by the number of manually performed steps. Currently, recording solutions that automate experimental overhead are either custom-made by researchers or provided as a submodule in comprehensive neuroscientific toolboxes, and there are no platforms focused explicitly on recording. **Objective:** Minimizing the number of manual actions may reduce error rates and experimental overhead. However, automation should avoid reducing the flexibility of the system. Therefore, we developed a software package named *T-Rex* (Standalone Recorder of Experiments) that specifically simplifies the recording of experiments while focusing on retaining flexibility. **Methods:** The proposed solution is a standalone webpage that the researcher can provide without an active internet connection. It is built using Bootstrap5 for the frontend and the Python package Flask for the backend. Only Python 3.7+ and a few dependencies are required to start the different experiments. Data synchronization is implemented using Lab Streaming Layer, an open-source networked synchronization ecosystem, enabling all major programming languages and toolboxes to be used for developing and executing the experiments. Additionally, *T-Rex* runs on Windows, Linux, and macOS. **Results:** The system reduces experimental overhead during recordings to a minimum. Multiple experiments are centralized in a simple local web interface that reduces an experiment's setup, start, and stop to a single button press. In principle, any type of experiment, regardless of scientific field (e.g. behavioral or cognitive sciences, and electrophysiology), can be executed with the platform. *T-Rex* includes an easy-to-use interface that can be adjusted to specific recording modalities, amplifiers, and participants. Because of the automated setup, easy recording, and easy-to-use interface, participants may even start and stop experiments by themselves, thus potentially providing data without the researcher's presence. **Conclusions:** We developed a new recording platform that is operating system independent, user friendly, and robust. We provide researchers with a so-

lution that can greatly increase the time spent on recording instead of setting up (with its possible errors).

6.1 Introduction

Recording high-quality electrophysiological human brain activity is notoriously difficult. The best quality signal has both high spatial and temporal resolution and is recorded with invasive electrodes [1, 2]. However, since implanting electrodes in humans for research purposes is a lengthy and challenging process with many safety and ethical concerns, scientists tend to use the clinical treatment of patients who receive implants for clinical purposes [3, 4] as a research vehicle. Some examples are patients with medication-resistant epilepsy undergoing presurgical monitoring for resection surgery [5] or patients qualified for deep brain stimulation [6].

Because recordings should not interfere with clinical treatment, the time to record data for neuroscientific experiments in these patient groups is severely limited. For implanted epilepsy patients, the recording windows are usually a few days to 2 weeks. In contrast, for patients with deep brain stimulation, the recording windows are during surgery using microelectrode recordings, and between surgery and when the stimulator is turned on. During these recording windows, patients need time to recover and have sufficient general well-being to participate. Moreover, time spent on clinical treatment and other assessments that require recording time can further reduce the already limited recording time.

Therefore, the brief remaining time window should be used as efficiently as possible. In practice, this means that the time spent on recording should be maximized, while the time spent on setup and solving errors should be minimized. Both the set-up time and error rate can be significantly reduced by automating as many manual actions as possible (eg, connecting to recording devices; starting experiments; selecting data streams; and starting, stopping, and synchronizing the recording). However, as experiments or recording setups change over time, it is often not worthwhile for research groups to invest in developing a more sophisticated system. It takes human resources, technical knowledge,

and substantial time investment to move beyond custom-made systems, which are often only used internally and unavailable to the public. Aside from custom-made setups, there exist multiple measurement platforms, including BCI2000 [7], OpenVIBE [8], FieldTrip [9], NFBlab [10], and ME-DUSA [11]. These systems can record data from many different amplifiers and include modules to design, analyze, and provide feedback during or after the experiments. While all these platforms also include good recording capabilities, they are more broadly focused on experimental design and analysis.

Additionally, these solutions limit the experiments that can be executed by the researcher in some way, either by targeting a specific type of experimental design or by imposing some hardware or software tool sets, such as programming language, input/output devices, or operating systems (OSs). Furthermore, not all platforms are open-source, which is not in the spirit of open science and impedes collective quality control and replicability. For example, FieldTrip requires the researcher to use the proprietary platform MATLAB, and BCI2000 and OpenVIBE impose the use of their tools and application programming interfaces. Additionally, the researcher must install a complete software package on the system, even when only the recording functionality is needed. Ashmaig et al. [12] developed and described a system exclusively focused on continuous data recording for neurosurgical patients. The system provides a good use case for naturalistic long-term recordings but has an extensive list of hardware requirements and limits the researcher to Linux. Furthermore, not all research groups have the opportunity to perform long-term recordings.

While all these platforms provide good solutions for their use case and cover a significant part of the neural recording space, we observed that none of these platforms are specifically tailored to the setup and recording of experiments. Here, we describe the *T-Rex* (Standalone Recorder of Experiments) platform that is specifically targeted to improve the recording of experiments. By automating the setup, start, and stop of experimental recordings, *T-Rex* reduces the error rate and time spent between recordings. *T-Rex* minimizes restrictions on hardware and software, is available on all major OSs, and is publicly available as an open-

source project. This work presents *T-Rex*'s system design, functionality, usage, and potential implications for the field.

6.2 Methods

Requirements

We determined 3 criteria that the system should meet to make *T-Rex* applicable to as many labs as possible. First, *T-Rex* should be as independent as possible of tools, paradigms, OSs, and programming languages. Each lab has its preferred tool set, and ensuring independence means that researchers do not need to port their existing experiments to fit *T-Rex*. Its only requirement is for the experiments to use Lab Streaming Layer (LSL) to stream data [13]. The backend of *T-Rex* uses LSL to synchronize data across sources (see the section Details of LSL). Second, *T-Rex* should be user friendly to both the researcher and the participant. Increasing simplicity will reduce error rates and time spent on setup, which can be achieved by automating multiple manual actions. Lastly, the system should be robust. This means that an experiment should only run when all requirements to run are met, and in case of technical problems, the experiment should retain the data up to that point and return to the Home screen.

System Outline

In brief, *T-Rex* acts as the middleman handling the experimental overhead for the researcher (Figure 6.1). When using *T-Rex*, the researcher can select an experiment by pressing a button on the main menu screen (Figure 6.2). *T-Rex* will then check the availability of all required data streams and connect to the streams. Examples of data streams are a hand-tracking device sending coordinates of a person's hands or an amplifier recording the participant's neural activity. *T-Rex* will then start the experiment user interface (UI) that instructs the participant on what task to perform. Upon successful start of the experiment UI, *T-Rex* starts recording all data streams and saves them to a folder specified by the researcher. All data are saved by LSL into a single `.xdf` file. After the experiment is completed, the UI prompts the participant on how the
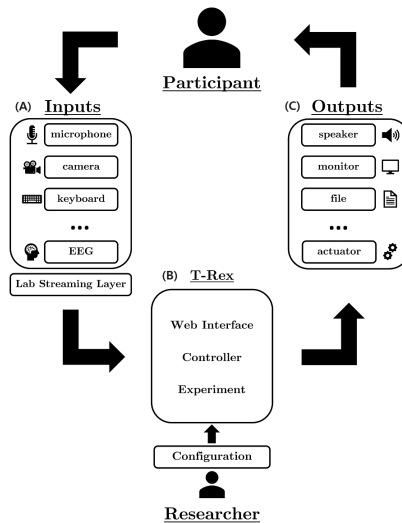
Figure 6.1: A schematic overview of the experiment loop of T-Rex (Standalone Recorder of Experiments). **A**) Data from the participants (eg, EEG, movement, and audio) are recorded by a variety of device inputs. Each input device should create a Lab Streaming Layer StreamOutlet to make the data available to record. **B**) T-Rex then provides a user interface for experiment selection. The backend finds the required data streams and records them. The rounded box shows the different software components (web interface, controller, and user configuration). **C**) Example outputs of the experiment. These components interact with the participant (experiment user interface and stimuli), or the recorded data are saved. EEG: electroencephalography.

experiment went and returns to the Home screen. During the full experiment loop, the actions that the researcher needs to perform are to start the required device data streams and select the experiment in the Home screen.

Materials, Software, and Technologies

T-Rex has multiple components, including a local web interface, a recording backend, and a controller interface connecting these 2 components. The web interface (Figure 6.2a-d) is built using Bootstrap5 for the frontend and the Python package Flask for the backend. The recording back-

end uses LSL and handles data stream synchronization and recording itself (information is provided in the section Details of LSL). *T-Rex* is compatible with Windows, Linux, and macOS. The controller interface (information is provided in the section Controller) is implemented in Python 3.7+ and a few dependencies found in `requirements.txt`.

Details of LSL

T-Rex uses LSL to synchronize the data streams from different devices, such as a variety of electroencephalography (EEG) amplifiers, audio streams, movement trackers, and cameras. The service handles "networking, time-synchronization, (near-) real-time access and optionally the centralized collection and recording of data." [13]. It is lightweight and has multi-language and multiplatform support, including Unity and Android. LSL allows the researcher to send data via a data stream to a local network server, which can be recorded. Basic usage involves defining a `Stream Outlet` that makes a time series data stream available on the network. The data are pushed per sample or per chunk into the outlet. By creating an outlet, the stream is made available to the local network of computers. The most basic usage (in Python) is represented in the following code block:

```python
from pylsl import StreamOutlet, StreamInfo
outlet = StreamOutlet(StreamInfo('my_marker_stream',
    'markers', 1, 0.0, str, 'my_unique_id'))
outlet.push_sample('Experiment_start')
```

This code creates a `StreamOutlet` object with a name (my_marker_-stream), type ("markers"), channel count (1), irregular sample rate (defined as 0.0), data type ("str"), and source ID ("my_unique_id"). Lastly, a sample containing "Experiment_start" is pushed to the outlet. Inversely, to receive data, one can instantiate a `StreamInlet` and use `inlet.pull_sample()`. For a comprehensive overview, see the official documentation [13]. For *T-Rex* to be able to record all data, the devices, and the experiments themselves must all create a `StreamOutlet` (like the example above). If no `StreamOutlet` is created, *T-Rex* will not

be able to find and record the device and start the experiment. By using LSL, *T-Rex* is able to connect to many popular experiment platforms, such as Psychopy, OpenSesame, and Presentation. In case a stream is listed in the requirements provided by the config in an experiment, but is not available, *T-Rex* will throw an error and return to the Home screen. Thus, no experiment can start while missing a data stream.

Trigger

In some recording setups, a trigger marks the start and end of an experiment. In these setups, participants' clinical data are recorded continuously and stored on a server. During an experiment, the data cannot be streamed directly and needs to be retrieved afterward by the responsible data steward. The data steward can locate the requested data files by identifying the trigger pattern sent by the experimenter. Depending on the manufacturer, a trigger can be delivered via the amplifier or with a separate device. If it can be delivered internally, the experimenter can directly send triggers from within the experiment, and the trigger functionality of *T-Rex* does not need to be used. *T-Rex* provides some basic functionality to send a trigger code if an external device is required. In short, *T-Rex* searches for a USB device with a name set in the main configuration file. It connects to this device and sets up an LSL stream. Then, if an experiment is started and the trigger flag in the main configuration file is set to True, the trigger class sends a user-defined code. When the experiment is finished, the trigger will be sent again, flagging the start and end of the complete experiment. The data steward can then retrieve the correct data with these trigger codes. At the same time as sending a trigger, the code also sends a marker to LSL, allowing for synchronization across data streams.

Software Components

The software consists of 2 main components: the web interface that handles the UI and the controller that sets up, starts, and stops all experiments (Figure 6.1b).
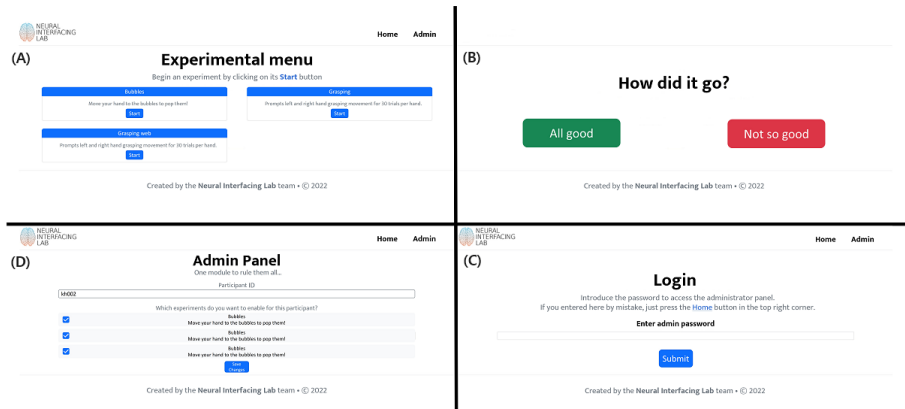
Figure 6.2: Representation of the main 4 windows of the web interface. **A**) The Home window contains all the experiments accessible to the researcher, represented on a grid configuration. **B**) The Experiment Feedback window allows obtaining feedback from the participants about their experience with the experiment. It is achieved through the green ("All good") and red ("Not so good") buttons. Participants can only continue after pressing one of these buttons. **C**) The Admin Login window allows access to the administration panel by entering the password. **D**) The Admin Configuration window allows the administrator to create new participants and modify their access to experiments.

Web Interface

The web interface includes 4 windows: Home, Experiment Feedback, Admin Login, and Admin Configuration (Figure 6.2).

The Home window (Figure 6.2a) displays all the experiments in a grid. Experiment cards are shown on that grid with a title, description, and start button. When the button is pressed, the controller executes a command that starts the selected experiment. The command is defined by the researcher and specified on the configuration of the experiment (more details are provided in the section User Configuration). During the experiment, the web interface is on stand-by awaiting the completion of the experiment.

After completion, the participant is redirected to the Experiment Feedback window, where the question "How did the experiment go?" is prompted (Figure 6.2). The participant or researcher is required to select a feedback option to continue. This allows the researcher to save a brief ex-

periment evaluation to assess data quality in later analysis. In potential future applications, the participants might perform the experiments by themselves. Then, this feedback is useful to flag the researcher to be aware of potential poor data quality. The feedback is stored under the file name `feedback.txt|` in the same folder as the most recent `.xdf` file (that contains the data recorded from the experiment).

The Admin Configuration provides the researcher with a closed environment where the participant identifier can be selected and a selection of all available experiments is available. To access the Admin Configuration, the researcher must first log in using the password that is configured in the main configuration file (Figure 6.2c; details are provided in the section User Configuration). When logged in, the researcher can see the configuration of the active experimental session, composed of an alphanumeric participant identifier and their access to experiments. A list of all the experiments included in the platform is visible from this window, but only those with checked marks are visible to the participant. The changes in this window are only applied after pressing the "Save" button at the end of the page.

The web UI has been tested with Firefox (version 105.0.1), Chrome (version 106), Safari (version 16), and Edge (version 106), although it should be compatible with higher versions and other mainstream browsers.

Controller

The `controller` handles everything related to running an experiment and has 3 main parts: setup, start, and stop (Figure 6.3). The related code can be found in the `./libs/` directory.

Setup   When an experiment is started by pressing the start button on the card, the `controller class` in *Controller.py* (Figure 6.3) is called, and it loads the main configuration file and extracts the information received from the UI about which experiment to run. With this information, an experiment instance is created, and its loading function is called.

`Experiment` loads the experiment-specific information and completes the setup in 3 steps. First, it checks for all devices and their LSL streams
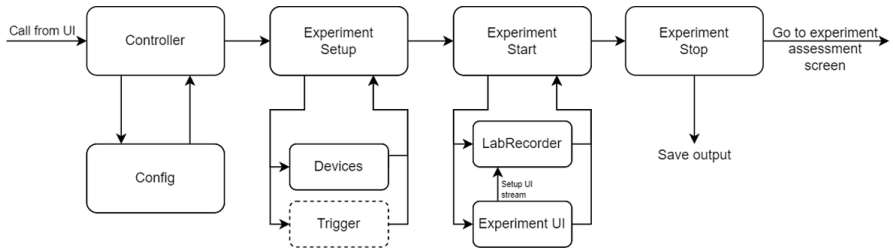
Figure 6.3: Backend flow of running an experiment. When an experiment is started by pressing the start button on the card, the controller is called, loading the main configuration file and extracting the information received from the user interface (UI) about which experiment to run. Then, an experiment instance is created, loading the experiment-specific information and completing the setup in 3 steps. First, it checks for all devices and their Lab Streaming Layer streams. Second, it initializes a recorder instance and adds all streams to the list of streams it should record. Lastly, if a trigger is required for the selected experiment, it will set up a trigger class that searches and connects to the trigger. Once the subprocess call is returned, experiment sends the final trigger and stops the recorder. The data is saved in the ./output/ folder, and the researcher or participant is redirected to the experiment assessment screen (Figure 6.2b).

as defined by the researcher in the experiment configuration under `device_inputs`. Subsequently, `experiment` initializes a recorder instance and adds all streams to the list of streams it should record. For a movement experiment [14–18], the streams recorded could be the neural amplifier and experimental triggers. Additionally, a movement tracker [19–21] or a force sensor [22] could be added. For speech perception [23–25] or auditory perception [26, 27], the audio stream, experiment triggers, and neural data need to be recorded. For speech production [28–31], the streams could be neural data, microphone, and triggers. In the Results section , we provide some example experiments. The last step is to check if a trigger is required for the selected experiment. If so, it will set up a trigger class that searches and connects to the trigger. All devices must be connected and available to LSL before the `experiment` instance is called. As all requested devices are essential for successful recording, *T-Rex* will raise an error and return to the UI if not all input devices are connected successfully.

Start   A user-defined command is called using Python's subprocess library to start the experiment UI. The command should be callable from the command line interface and can be set in the experiment-specific configuration. Because the experiment UI likely contains a stream that sends out experiment-related markers, `experiment` will start a loop on a user-defined timeout to search for the marker stream. Once found, usually almost instantly, the recorder will start recording all streams. Implementing the system this way does not restrict the research aside from using LSL. However, owing to the timeout, the experiment may start before the recording starts. This can only happen if the time between the setup of the experiment StreamOutlet and sending the first marker is shorter than the time that the recorder can find the stream and start the recording. Usually, finding the StreamOutlet and starting the recording is in the order of milliseconds. However, to entirely prevent the possibility of this happening, we recommend including a waiting screen in the experiment UI (eg, "Press button to start") or ensuring sufficient time (longer than the timeout set in the experiment configuration) between the setup of a StreamOutlet and the start of the experiment. Once connected to the experiment StreamOutlet, the experiment UI should start, and the experiment instance will wait until the called command is terminated and returned, which usually happens when the experiment UI window is closed.

Stop   Once the subprocess call is returned, experiment sends the final trigger and stops the recorder. The data are saved in the `./output/` folder, defined in the main configuration file (information is provided in the section User Configuration). An example of the created directory tree can be found in supplementary data 4.

Device Inputs

Each experiment can have multiple input devices, such as an amplifier measuring the neural data, a hand-tracking device, and a microphone. Any device can be included if it generates a StreamOutlet. Each device should send the data from the device to LSL, allowing it to be ac-

cessed by the other system components and to be recorded. The name, type, or source_id supplied to the StreamOutlet will be the values that *T-Rex* will search for during experiment setup (information is provided in the section Controller). In practice, this means that either the name, type, or source_id needs to be supplied under device_inputs in the experiment configuration file (information is provided in the section Experiment Configuration). Since devices can be used for multiple experiments, we included a separate destination for all device input files (`./exp_module/inputs`), although input devices can be stored anywhere as long as they generate a StreamOutlet.

User Configuration
There are 2 types of configuration files that the researcher can set: main configuration and experiment-specific configuration. All configuration files are formatted in Yet Another Markup Language (YAML).

Main Configuration
The file `config.yaml` in the root folder contains the system-wide configuration. This configuration file contains information containing general settings. Supplementary data 1 contains a description of the different available options, and supplementary data 2 contains an example of the main configuration file. The `main` option under `path` is the path all relative paths will be anchored to and should be set to the root folder. Most parameters are preset, but `out` and `trigger` configurations may vary between different recording setups and might need to be redefined.

Experiment Configuration
Each experiment included in *T-Rex* requires a separate folder in `./exp_module/experiments/` and must include at least 2 files: `config.yaml` and the file to start the experiment. A full description of all the fields and different options in the `config.yaml` can be found in the supplementary data 5. The `name` and `description` define the text shown in the UI, `command` sets the command line interface command made by the controller class to start the experiment, `exp_outlet` sets the name,

type, or source_id that the experiment class will search for. For example, if the experiment UI is a Python script that will create a Stream-Outlet named markers, the `command` to execute would be `python.\`
`exp_module\experiments\your_experiment_file.py` and `exp_outlet='markers'`.

6.3 Results
We have included 3 different example experiments to provide a practical view of how to use T-Rex. The examples can also serve as a quick start for researchers to create new experiments or adapt the ones included. A step-by-step explanation of adding a new experiment is described in the section 6.3 to the Platform.

Case 1: Simple Experiment in Python
This experiment is a simple text-based instruction for a grasping task (Figure 6.4a). The participant is prompted by text in a Python Tkinter window to continuously open and close either the left or right hand, as used previously [32]. The experiment requires neural data as the input device and generates a StreamOutlet to send markers that inform about the start and end of the experiment and of the trials. The neural data are acquired from a stream with `name=Micromed`, `type=EEG`, and `source_id=micm01`. These values are all set by the researcher. As *T-Rex* will search for all 3 options (name, type, and source_id), only 1 must be provided. Therefore, the option under `device\_inputs` in `grasping\config.yaml` is set to `eeg` (case insensitive). Next, the marker StreamOutlet that will be generated by the experiment has `source_id=emuidw22`. When the `experiment` class runs the experiment command (`command` field in `grasping\config.yaml`), it will search for these streams. Therefore, the `exp_outlet` field is set to 'emuidw22'. Finally, since the grasping experiment is Python-based, the `command` should use Python to call the script with the command: `python.\exp_module\experiments\grasping\grasping.py`. The configuration file used can be found in supplementary data 6.
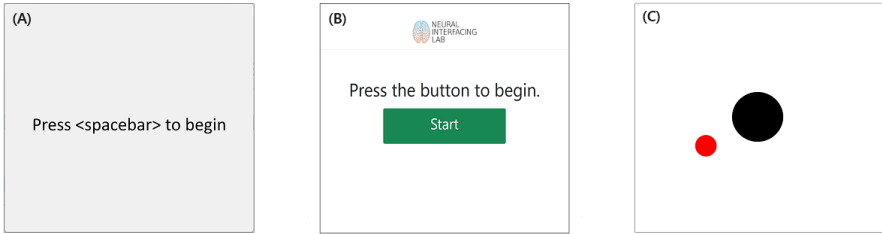
Figure 6.4: User interfaces for the 3 use case experiments included. **A**) Grasping: simple text-based experiment built using the Python package Tkinter. **B**) Grasping web experiment: reimplementation of the grasping experiment as a single page application (SPA) to allow its execution on any device with access to a web browser. **C**) 3D hand-tracking experiment: the hand-tracking is performed using the LeapMotion controller, and the experiment is implemented in Python using the package Tkinter.
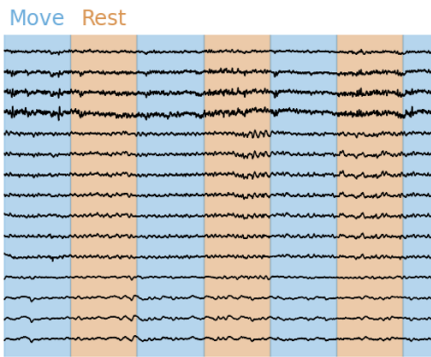
Figure 6.5: Neural data were recorded with the grasping experiment using T-Rex (Standalone Recorder of Experiments). Two streams were recorded during this experiment: an EEG stream and a marker stream. The data from the EEG stream is shown by the black lines, indicating the voltage over time in a selection of 15 neural electrodes. The marker stream sends the start and end of the experiment and the individual trials. These markers were used to determine the colored areas (blue and orange) shown. EEG: electroencephalography.

When these options are set, the experiment is ready to go and can be started by pressing the start button on the *Home* window. The Tkinter window opens and waits for the spacebar to be pressed. Once pressed, the experiment starts and is locked as the top viewed window until completion. When the experiment is finished and closed (i.e. the command call ends and returns to the experiment class), the `experiment` instance stops the recording and saves the data. In-depth details on how experiments are started and stopped are described in the section Controller.

Figure 5 shows a random selection of 15 channels of neural data recorded with T-Rex during the

grasping experiment. Two streams were used in this experiment. First a marker StreamOutlet that sends all experiment-related markers, such as the start and end of the experiments and the start and end of each trial, with the accompanying label (move or rest). Second, an EEG Stream-Outlet that streams the data from our Micromed Amplifier to LSL. With T-Rex, these streams were automatically identified and recorded. The start and end of the colored columns (identifying move and rest trials) were determined by the recorded markers sent through the marker StreamOutlet. The synchronization by LSL ensures that the EEG and marker stream timestamps are the same.

Case 2: Simple Experiment in a Web UI

We included the same grasping experiment as in Case 1 but implemented it in a web interface (Figure 6.4b). It uses a single page application (SPA) locally and thus can be created on any device with access to a web browser, like a laptop, tablet, and smartphone. The grasping web experiment also illustrates options other than a Tkinter window for experimenting. No internet connection is required, relieving some security concerns that could render execution on the web unsafe.

We constructed the experiment using HTML, CSS (Bootstrap5 for the responsiveness and other visual aspects), and JavaScript for the behavior. The device input is the same as in the Tkinter implementation of the experiment and the StreamOutlet containing the markers; thus, the `device_inputs` and `exp_outlet` are the same. The difference is in the command executed to start the experiment. In this case, start `./exp_module/experiments/graspingWeb/index.html` is used. The configuration file used can be found in supplementary data 7.

Once the experiment is started on the *Home* window, the `experiment` instance opens another tab on the browser displaying the "grasping_web" experiment. The experiment starts when the participant presses the green "Start" button. When the experiment is finished, the participant or researcher is prompted to press a red button to close the experiment. The GraspingWeb command call is finished at the button press and returns to the `experiment` instance, stopping the recording and saving

the data.

Case 3: Multiple Devices

Lastly, we included a 3D hand-tracking experiment, where the goal is to hold a cursor (a black circle) on a target (a red circle). The cursor can be moved in 3 dimensions, where the third dimension controls the size of the circle (Figure 6.4c). In this case, the hand-tracking is performed by the LeapMotion controller, but any other device can be used. We have provided a `.exe` file that reads the data from the tracker and sends it to an LSL StreamOutlet with `name=LeapLSL`, `type=Coordinates`, and `source_id=LEAPLSL01`. In addition to the hand-tracking information, we also need neural activity, for which we use the same StreamOutlet as described in Case 2. Lastly, the experiment is implemented in a Python Tkinter window and generates a marker stream similar to the streams described in the previous use case with `Source_id=BUBBLE01`. Thus, to set up the configuration for this experiment, we set the command to `python./exp_module/experiments/Bubbles/bubbles.py`, exp_outlet to `BUBBLE01`, and device_inputs to `LEAPLSL01` (the tracking information stream) and `eeg` (the neural data stream). To run the experiment, the researcher should start the device stream before the experiment is started in the Home screen (ie, run the `.exe` first). The configuration file used can be found in supplementary data 8.

Mix and Match

We have presented only 3 examples showing different possibilities. Different devices can be included by adding a StreamOutlet name, type, or source_id to the list of `device_outputs`. The only requirement to add a device is that the data from the device can be sent to a LabStreamingLayer StreamOutlet. This code is either supplied by the manufacturer or written by the researcher. If this requirement is met, any medical device or technology can be included, as T-Rex does not impose any further restrictions on technologies or types of experiments, including, but not limited to, speech production, audio or speech perception, movement, decision-making, and simple or naturalistic tasks [33, 34]. For
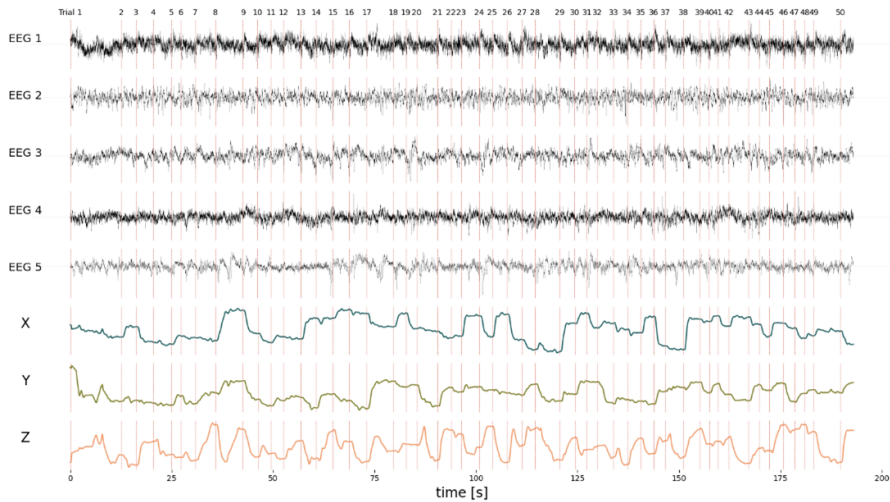
Figure 6.6: The combined data recorded from 3 different streams: an EEG stream, a marker stream, and a LeapMotion controller. The EEG channels are 5 channels randomly selected from 87 available channels. X, Y, and Z are the 3D coordinates of the palm of the hand, provided by a LeapMotion controller. The marker stream provides the shown trials (numbers on top with vertical dashed lines). To start and record this experiment, the LeapLSL stream has to be started, along with the EEG stream. Then, only the experiment needs to be started in T-Rex (Standalone Recorder of Experiments). T-Rex records all 3 streams (synchronized by Lab Streaming Layer), ultimately allowing to combine the 3 streams into this image. EEG: electroencephalography.

example, new experiments can also be built in Unity or PyGame to provide better graphical experiences.

Adding New Experiments to the Platform

The following steps describe how to add a new experiment from scratch to T-Rex:

1. Create the experiment folder inside the directory `./exp_module /experiments/`. An example of the directory tree for different example experiments can be found in supplementary data 3.

2. Create the experiment configuration file (`config.yaml`) inside the new folder. Information in supplementary data 9 can be used as the base example for creating this file, and the section Experiment Configuration contains a detailed description of each parameter.

3. Adjust the fields to the specific experiment.

After completing these initial steps, the experiment should be visible from the Admin Configuration panel. The researcher can set the experiment as "visible" from the admin panel by selecting its corresponding check mark. If configured as "visible," it should appear on the Home window, and it can be executed by clicking on its respective button. It is worth mentioning that when porting an already configured version of T-Rex to a different OS, some parameters might need to be revised. For example, regarding the parameter command, when used on Windows to start a Python experiment, the definition is the following:

```
command: python .\exp_module\experiments\example\example_experiment.py
```

However, when used on Unix or Unix-like systems, the definition changes to the following:

```
command: python ./exp_module/experiments/example/example_experiment.py
```

The difference comes because "/" is the path separator on Unix and Unix-like systems, and Microsoft uses "\".

There might be other scenarios where the parameter `command` might differ between OSs; thus, we recommend revising each experiment configuration file when porting the platform to a different OS.

Practical Experience

At the time of writing, we entirely switched to recording with T-Rex for our experiments at different recording sites. So far, we have recorded multiple experiments, involving speech, motor, and decision-making tasks. Furthermore, at one of the recording sites, we recorded using the trigger functionality included in T-Rex. We see no indications of different data quality in our neural decoding endeavors. We can decode speech [35, 36] and movement trajectories [37] with performance equal to that using our previous setup.

6.4 Discussion

We presented *T-Rex*, an independent, user friendly, and robust system that minimizes the setup time and error rate. *T-Rex* provides a simple UI and reduces the experimental setup to the press of a button. The software merges the LSL recording backend with a simple UI, automating experimental overhead for the researcher. *T-Rex* reduces the setup time and error rate, resulting in more time spent recording neural data. The simplicity of *T-Rex* reduces the number of actions that the researcher must perform to only 2: starting the required devices and starting the experiment. The fewer manual actions the researcher needs to perform, the lower the chance that an error is made. It improves reliability and increases total data volume and time spent on recording. The LSL software package fully handles synchronization and recording. We decided on LSL as it is lightweight, is easy to use, has submillisecond timekeeping, and has a proven track record [38]. The flexibility of *T-Rex* makes the system applicable in fields other than the neuroscientific context described here.

T-Rex provides benefits for both the researcher and participant. A streamlined process may have multiple benefits from the perspective of the participant. It leaves more time to interact with the participant, mak-

ing it more comforting and engaging. *T-Rex* may be particularly beneficial for participants who are anxious or nervous about participating. Furthermore, a streamlined process conveys more professionalism and may improve participation satisfaction, ultimately increasing the willingness to participate in future research. Moreover, if the start and recording of experiments are simplified enough, participants may be able to run experiments themselves. The introduction of engaging and fun experiments that enable participants to run them as they like provides the participants with an opportunity to alleviate boredom and do something meaningful by contributing to scientific research. Together, both the researcher (more data) and the participant (more engagement) are benefitted. While *T-Rex* has been developed with independent recording in mind, it is currently not being tested for that purpose.

In comparison with other available software platforms, *T-Rex* is the only solution specifically focused on recording experiments, allowing it to remain lightweight. Platforms like BCI2000 [7], OpenViBE [8], and MEDUSA [11] offer comprehensive functionalities spanning the 3 stages of a BCI system: signal acquisition, signal processing, and feedback presentation. However, they require complete software installation even if only the recording module is needed. *T-Rex* enhances the researcher experience by offering flexibility in the choice of programming language and technology for creating the experiments, unlike BCI2000 and OpenViBE, which mandate the use of C++; MEDUSA, which requires the use of Python; or NFBlab [10], which requires the use of its graphical UI. Regarding compatibility, *T-Rex* holds a distinct advantage, supporting all major OSs, including Windows, Linux, and macOS. This is in contrast with BCI2000's limited functionality outside Windows and MEDUSA's exclusive Windows availability, as well as the system presented by Ashmaig et al. [12], which is Linux-bound. Each of these platforms has its strengths and excels in its intended function. *T-Rex* provides a tailored solution for a specific part of neuroscientific research that allows it to remain simple and lightweight.

T-Rex aims for simplicity, setting up experiments in *T-Rex* requires basic knowledge of command line interface usage. Moreover, experiments and devices must use LSL to make data available. Although LSL is avail-

able for all mainstream OSs and programming languages, experiments already used by researchers may require adjustments to the experiment code structure for inclusion in *T-Rex*. Therefore, technical knowledge and usage of LSL may limit the applicability for some labs. Furthermore, *T-Rex* is available for all mainstream OSs but may not apply to all different versions. Specifically, the command line interface version of LabRecorder, including the script that records and stores the multiple data streams, had to be built for different chipsets (M1 and M2) for macOS. These are currently included, but other architectures likely require a different build of LabRecorder. As *T-Rex* matures, we expect more versions to become applicable. *T-Rex* is in ongoing development, and we have identified several potential future updates targeting an improved user experience. First, device streams currently need to be started manually, and this may be performed automatically at the start of an experiment.

This is also a requirement to enable participants to start recordings themselves, which is a main future improvement. Aside from ensuring that there are no manual actions except starting the experiments, allowing *T-Rex* for independent use may require improved internal logging and error handling. Combined, these updates would reduce even more actions for both the researcher and participant, and increase the robustness of *T-Rex*. In conclusion, *T-Rex* offers a flexible solution to record neuroscientific experiments. It streamlines setup and recording, and reduces error rates that increase the time spend on recordings. We envision *T-Rex* to help standardize and simplify recording experiments and eventually allow recordings by participants independently. This may improve the overall satisfaction of participation and increase the amount of data collected. The open-source nature of *T-Rex* is in the spirit of open science and increases its value through an increase in community knowledge.

6.5 Acknowledgments

project number VI.Veni.194.021.

Data Availability
The source code, installation guide, and example experiments can be found on GitHub: `https://github.com/neuralinterfacing lab/t-rex`. *T-Rex* is available under the permissive MIT License. As *T-Rex* will be in ongoing development, we kindly invite researchers to provide feedback or contribute to this open-source project.

Authors' Contributions
JAV, MCO, MV, PK, and CH conceptualized the study. JAV, MCO, and PK performed the investigation. JAV, MCO, PK, and CH participated in the methodology. JAV and MCO contributed to project administration. PK and CH managed the resources. JAV, MCO, and PK contributed to the software. PK and CH supervised the study. JAV, MCO, and MV contributed to validation. JAV and MCO contributed to visualization. JAV and MCO wrote the original draft. JAV, MCO, MV, PK, and CH reviewed and edited the manuscript.

Conflicts of Interest
The author PK is the Editor-in-Chief of JMIR Neurotechnology. PK was not involved in any decisions made regarding this manuscript. All other authors declare no conflicts of interest.

Abbreviations
EEG: electroencephalography LSL: Lab Streaming Layer OS: operating system T-Rex: Standalone Recorder of Experiments UI: user interface YAML: Yet Another Markup Language

References
[1] Christian Herff, Dean J. Krusienski, and Pieter Kubben. "The Potential of Stereotactic-EEG for Brain-Computer Interfaces: Current Progress and Future Directions". English. In: *Frontiers in Neuroscience* 14 (2020). Publisher: Frontiers. DOI: 10.3389/fnins.2020.00 123.

[2]   Joshua Jacobs and Michael J. Kahana. "Direct brain recordings fuel advances in cognitive electrophysiology". en. In: *Trends in Cognitive Sciences* 14.4 (Apr. 2010), pp. 162–171. DOI: 10.1016/j.tics.2010.01.005.

[3]   Ashley Feinsinger et al. "Ethical commitments, principles, and practices guiding intracranial neuroscientific research in humans". en. In: *Neuron* 110.2 (Jan. 2022), pp. 188–194. DOI: 10.1016/j.neuron.2021.11.011.

[4]   Manuel R Mercier et al. "Evaluation of cortical local field potential diffusion in stereotactic electro-encephalography recordings: A glimpse on white matter signal". In: *NeuroImage* 147 (2017). Publisher: Elsevier, pp. 219–232. DOI: 10.1016/j.neuroimage.2016.08.037.

[5]   Patrick Chauvel, Jorge Gonzalez-Martinez, and Juan Bulacio. "Chapter 3 - Presurgical intracranial investigations in epilepsy surgery". en. In: *Handbook of Clinical Neurology*. Ed. by Kerry H. Levin and Patrick Chauvel. Vol. 161. Clinical Neurophysiology: Diseases and Disorders. Elsevier, Jan. 2019, pp. 45–71. DOI: 10.1016/B978-0-444-64142-7.00040-0.

[6]   Andres M. Lozano et al. "Deep brain stimulation: current challenges and future directions". In: *Nature Reviews Neurology* 15.3 (2019). Publisher: Springer US, pp. 148–160. DOI: 10.1038/s41582-018-0128-2.

[7]   G. Schalk et al. "BCI2000: A General-Purpose Brain-Computer Interface (BCI) System". en. In: *IEEE Transactions on Biomedical Engineering* 51.6 (June 2004), pp. 1034–1043. DOI: 10.1109/TBME.2004.827072.

[8]   Yann Renard et al. "OpenViBE: An Open-Source Software Platform to Design, Test, and Use Brain–Computer Interfaces in Real and Virtual Environments". In: *Presence* 19.1 (Feb. 2010). Conference Name: Presence, pp. 35–53. DOI: 10.1162/pres.19.1.35.

[9]   Robert Oostenveld et al. "FieldTrip: Open Source Software for Advanced Analysis of MEG, EEG, and Invasive Electrophysiological Data". en. In: *Computational Intelligence and Neuroscience* 2011 (Dec. 2010). Publisher: Hindawi, e156869. DOI: 10.1155/2011/156869.

[10]   Nikolai Smetanin et al. "NFBLab—A Versatile Software for Neurofeedback and Brain-Computer Interface Research". In: *Frontiers in Neuroinformatics* 12 (2018).

[11]   Eduardo Santamaría-Vázquez et al. "MEDUSA©: A novel Python-based software ecosystem to accelerate brain-computer interface and cognitive neuroscience research". eng. In: *Computer Methods and Programs in Biomedicine* 230 (Mar. 2023), p. 107357. DOI: 10.1016/j.cmpb.2023.107357.

[12]   Omer Ashmaig et al. "A Platform for Cognitive Monitoring of Neurosurgical Patients During Hospitalization". In: *Frontiers in Human Neuroscience* 15 (2021).

[13]   Christian Kothe. *sccn/labstreaminglayer*. original-date: 2018-02-28T10:50:12Z. 2014.

[14]   Maarten C. Ottenhoff et al. "Continuously Decoding Grasping Movements using Stereotactic Depth Electrodes". In: *2021 43rd Annual International Conference of the IEEE Engineering in Medicine & Biology Society (EMBC)*. Nov. 2021, pp. 6098–6101. DOI: 10.1109/EMBC46164.2021.9629639.

[15]   Maarten C. Ottenhoff et al. *Executed and imagined grasping movements can be decoded from lower dimensional representation of distributed non-motor brain areas*. July 2022. DOI: 10.1101/2022.07.04.498676.

[16]   Guangye Li et al. "Assessing differential representation of hand movements in multiple domains using stereo-electroencephalographic recordings". en. In: *NeuroImage* 250 (Apr. 2022), p. 118969. DOI: 10.1016/j.neuroimage.2022.118969.

[17] Guangye Li et al. "Detection of human white matter activation and evaluation of its function in movement decoding using stereo-electroencephalography (SEEG)". eng. In: *Journal of Neural Engineering* (July 2021). DOI: 10.1088/1741-2552/ac160e.

[18] Timon Merk et al. "Electrocorticography is superior to subthalamic local field potentials for movement decoding in Parkinson's disease". In: *eLife* 11 (May 2022). Ed. by Nicole C Swann, Michael J Frank, and Kevin Wilkins. Publisher: eLife Sciences Publications, Ltd, e75126. DOI: 10.7554/eLife.75126.

[19] Valeria Mondini et al. "Continuous low-frequency EEG decoding of arm movement for closed-loop, natural control of a robotic arm". In: *Journal of Neural Engineering* 17.4 (2020). DOI: 10.1088/1741-2552/aba6f7.

[20] Christine Azevedo Coste et al. "Activating effective functional hand movements in individuals with complete tetraplegia through neural stimulation". eng. In: *Scientific Reports* 12.1 (Oct. 2022), p. 16189. DOI: 10.1038/s41598-022-19906-x.

[21] Seyyed Moosa Hosseini and Vahid Shalchyan. "Continuous Decoding of Hand Movement From EEG Signals Using Phase-Based Connectivity Features". In: *Frontiers in Human Neuroscience* 16 (2022).

[22] Syed A. Shah, Huiling Tan, and Peter Brown. "Continuous force decoding from deep brain local field potentials for Brain Computer Interfacing". In: *International IEEE/EMBS Conference on Neural Engineering, NER* (2017). ISBN: 9781538619162, pp. 371–374. DOI: 10.1109/NER.2017.8008367.

[23] Prachi Patel et al. "Interaction of bottom-up and top-down neural mechanisms in spatial multi-talker speech perception". en. In: *Current Biology* 32.18 (Sept. 2022), 3971–3986.e4. DOI: 10.1016/j.cub.2022.07.047.

[24] Kevin D. Prinsloo and Edmund C. Lalor. "General auditory and speech-specific contributions to cortical envelope tracking revealed using auditory chimeras". eng. In: *The Journal of Neuroscience: The Official Journal of the Society for Neuroscience* (Aug. 2022), JN-RM-2735-20. DOI: 10.1523/JNEUROSCI.2735-20.2022.

[25] Emmanuel Biau et al. "Left Motor δ Oscillations Reflect Asynchrony Detection in Multisensory Speech Perception". en. In: *Journal of Neuroscience* 42.11 (Mar. 2022). Publisher: Society for Neuroscience Section: Research Articles, pp. 2313–2326. DOI: 10.1523/JNEUROSCI.2965-20.2022.

[26] Lars Hausfeld et al. "Cortical processing of distracting speech in noisy auditory scenes depends on perceptual demand". eng. In: *NeuroImage* 228 (Mar. 2021), p. 117670. DOI: 10.1016/j.neuroimage.2020.117670.

[27] Lars Hausfeld et al. "Modulating Cortical Instrument Representations During Auditory Stream Segregation and Integration With Polyphonic Music". eng. In: *Frontiers in Neuroscience* 15 (2021), p. 635937. DOI: 10.3389/fnins.2021.635937.

[28] Miguel Angrick et al. "Speech synthesis from ECoG using densely connected 3D convolutional neural networks". In: *Journal of Neural Engineering* 16.3 (2019). Publisher: IOP Publishing. DOI: 10.1088/1741-2552/ab0c59.

[29] Christian Herff et al. "Generating Natural, Intelligible Speech From Brain Activity in Motor, Premotor, and Inferior Frontal Cortices". eng. In: *Frontiers in Neuroscience* 13 (2019), p. 1267. DOI: 10.3389/fnins.2019.01267.

[30] Miguel Angrick et al. "Real-time synthesis of imagined speech processes from minimally invasive recordings of neural activity". en. In: *Communications Biology* 4.1 (Sept. 2021). Bandiera_abtest: a Cc_license_type: cc_by Cg_type: Nature Research Journals Number: 1 Primary_atype: Research Publisher: Nature Publishing Group Subject_term: Brain–machine interface;Neural decoding Subject_term_id: brain-machine-interface;neural-decoding, pp. 1–10. DOI: 10.1038/s42003-021-02578-0.

[31] David A. Moses et al. "Neuroprosthesis for Decoding Speech in a Paralyzed Person with Anarthria". In: *New England Journal of Medicine* 385.3 (July 2021). Publisher: Massachusetts Medical Society _eprint: https://doi.org/10.1056/NEJMoa2027540, pp. 217–227. DOI: 10.1056/NEJMoa2027540.

[32] Maarten C. Ottenhoff et al. *Global motor dynamics - Invariant neural representations of motor behavior in distributed brain-wide recordings*. July 2023. DOI: 10.1101/2023.07.07.548122.

[33] Saurabh Sonkusare, Michael Breakspear, and Christine Guo. "Naturalistic Stimuli in Neuroscience: Critically Acclaimed". eng. In: *Trends in Cognitive Sciences* 23.8 (Aug. 2019), pp. 699–714. DOI: 10.1016/j.tics.2019.05.004.

[34] Liberty S. Hamilton and Alexander G. Huth. "The revolution will not be controlled: natural stimuli in speech neuroscience". eng. In: *Language, Cognition and Neuroscience* 35.5 (2020), pp. 573–582. DOI: 10.1080/23273798.2018.1499946.

[35] Joaquin Amigo-Vega et al. "Decoding articulatory trajectories during speech production from intracranial EEG". In: *Proceedings of the 10th International Brain-Computer Interface Meeting 2023*. 2023. DOI: 10.3217/978-3-85125-962-9-13.

[36] Maxime Verwoert et al. "Evaluating implant locations for a minimally invasive speech BCI". In: *Proceedings of the 10th International Brain-Computer Interface Meeting 2023*. 2023. DOI: 10.3217/978-3-85125-962-9-13.

[37] Ottenhoff, Maarten C. et al. "Decoding hand kinematics from brain-wide distributed neural recordings". In: *Proceedings of the 10th International Brain-Computer Interface Meeting 2023*. 2023. DOI: 10.3217/978-3-85125-962-9-113.

[38] Qile Wang et al. "A scoping review of the use of lab streaming layer framework in virtual and augmented reality research". en. In: *Virtual Reality* 27.3 (Sept. 2023), pp. 2195–2210. DOI: 10.1007/s10055-023-00799-8.

6.6 Supplementary material

```
1   path:
2     main: Path to the root directory of the project, when set to
3           "default" the value is obtained automatically.
4     exe:  Relative path to the Lab Recorder executable.
5     out:  Relative path to the output directory where the files
6           generated during the experiments will be saved.
7
8   log_file: Relative path to the log file.
9   password: Password to access the Admin Configuration window.
10  debug:    Used for debugging purposes, when "True" a testing
11            LSL stream under the name DBG01 will be created
12
13  trigger:
14    sequence: Binary sequence that the trigger will send to
15              the amplifier.
16    serial_com_name: Name of the trigger device that the
17                     recorder will search for.
```

Supplementary data 1 - This is the system-wide configuration file that must be placed inside the root folder of the project, which allows the researcher to configure the execution of T-Rex.

```
1       path:
2         main: default
3         exe: libs/labrecorder/LabRecorderCLI.exe
4         out: output
5       log_file: record.log
6       password: 'qwer'
7       debug: False
8       trigger:
9         sequence: [1, 0, 0, 1, 0, 0, 1]
10        serial_com_name: 'Prolific PL2303GT'
```

Supplementary data 2 - An example of a main configuration file example. Note that all paths are relative to the main parameter.

```
exp_module
├── inputs
└── experiments
    ├── EXPERIMENT_1
    │   ├── config.yaml
    │   └── experiment_1.py
    ├── EXPERIMENT_2
    │   ├── config.yaml
    │   └── experiment_2.html
    └── EXPERIMENT_3
        ├── config.yaml
        └── experiment_3.exe
```

Figure 6.7: Supplementary data 3 - The directory tree illustrates a system with 3 different folders each for a different experiment (/EXPERIMENT_1/ /EXPERIMENT_2/ and /EXPERIMENT_3/). Each experiment contains their own configuration file (config.yaml). The researcher can add any additional files to each folder.

```
output
└─PARTICIPANT_ID
   ├─access.yaml
   └─YYYY_MM_DD
      └─ID_OF_EXPERIMENT_HH_MM_SS
         ├─output.xdf
         ├─feedback.txt
         └─logs.log
```
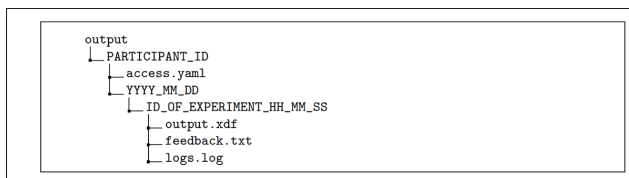
Supplementary data 4 - The directory tree illustrates the content of the ./output/ folder when saving the experimental data gathered with one experiment. The output.xdf file is created upon the experiment completion. It contains the recorded data from the pre-configured LSL streams. The feedback.txt file contains the feedback the participant inputted on the Experiment Feedback window and it is saved in the same folder as the most recent .xdf file.

```
1   name: Name of the experiment. This value will be used as the title for
2        the web interface buttons shown to the participants.
3   description: Short description of the experiment that will be shown
4              in the experiment "cards" in the user UI.
5   id: Unique identifier for the experiment. This name should match the
6       name of the folder where the experiment is stored inside the
7       directory "./exp_module/experiments".
8   command:  Command that is called by the Experiment instance. It must be able
9             to run from a command prompt.
10  timeout: Amount of seconds the recorder will search for a marker stream.
11  exp_outlet: Source id of the marker stream generated by
12             the user experiment (by calling "command").
13  device_inputs: List of devices that the recorder will search for.
14                The recorder will find matching streams based on name,
15                type, and source_id as defined by LabStreamingLayer.
16  trigger: Switch whether a trigger should be sent for this experiment.
```

Supplementary data 5 - The different options for the experiment configuration file. Each experiment must include this file. The parameter command might need to be modified when porting the platform to a different Operating System (from Windows to Linux or macOS, for example). It is up to the researcher to perform the redefinition.

```
1   name: 'Grasping'
2   description: 'Prompts left and right hand grasping movement for
3       30 trials per hand.'
4   id: grasping
5   command: python .\exp_module\experiments\grasping\grasping.py
6   timeout: 5
7   exp_outlet: emuidw22
8   device_inputs:
9     - EEG
10  trigger: False
```

Supplementary data 6 - Experiment configuration file used for the grasping experiment. This experiment presents simple instructions to the participant indicating continuous opening and closing of either their left or right hand. The visual interface was built using the Python Tkinter library.

130

```
1  name: 'Grasping Web'
2  description: 'Prompts left and right hand grasping movement for
3      30 trials per hand (using a web interface).'
4  id: graspingWeb
5  command: start .\exp_module\experiments\graspingWeb\index.html
6  timeout: 10
7  exp_outlet: GRASPWO1
8  device_inputs:
9    - EEG
10 trigger: False
```

Supplementary data 7 - Experiment configuration file used for the grasping-web experiment. This experiment presents simple instructions to the participant indicating continuous opening and closing of either their left or right hand. The visual interface was built using HTML, CSS (Bootstrap5 for the responsiveness and other visual aspects), and JavaScript for the behavior.

```
1  name: 'Bubbles'
2  description: 'Move your hand to the bubbles to pop them!'
3  id: bubbles
4  command: python .\exp_module\experiments\Bubbles\bubbles.py
5  timeout: 10
6  exp_outlet: BUBBLE01
7  device_inputs:
8    - LEAPLSLO1
9    - EEG
10 trigger: False
```

Supplementary data 8 - Experiment configuration file used for the 3D hand tracking experiment. The goal of the experiment is to hold the cursor on the target. The cursor can be moved in 3d, where the third dimension controls the size of the circle. In this case, the hand tracking is done by the LeapMotion controller.

```
1  name: 'NAME OF THE EXPERIMENT'
2  description: 'DESCRIPTION OF THE EXPERIMENT'
3  id: 'ID OF THE EXPERIMENT, IT MUST MATCH THE FOLDER NAME'
4  command: 'COMMAND THAT EXECUTES THE EXPERIMENT'
5  timeout: 'TIMEOUT FOR STOP SEARCHING THE STREAMS (SECONDS)'
6  exp_outlet: 'ID OF STREAM GENERATED WITH COMMAND'
7  device_inputs:
8    - 'DEVICE THE RECORDER WILL SEARCH'
9    - 'DEVICE THE RECORDER WILL SEARCH'
10 trigger: 'True FOR USING TRIGGER, False OTHERWISE'
```

Supplementary data 9 - Template that can be used for creating some experiment configuration file.

131
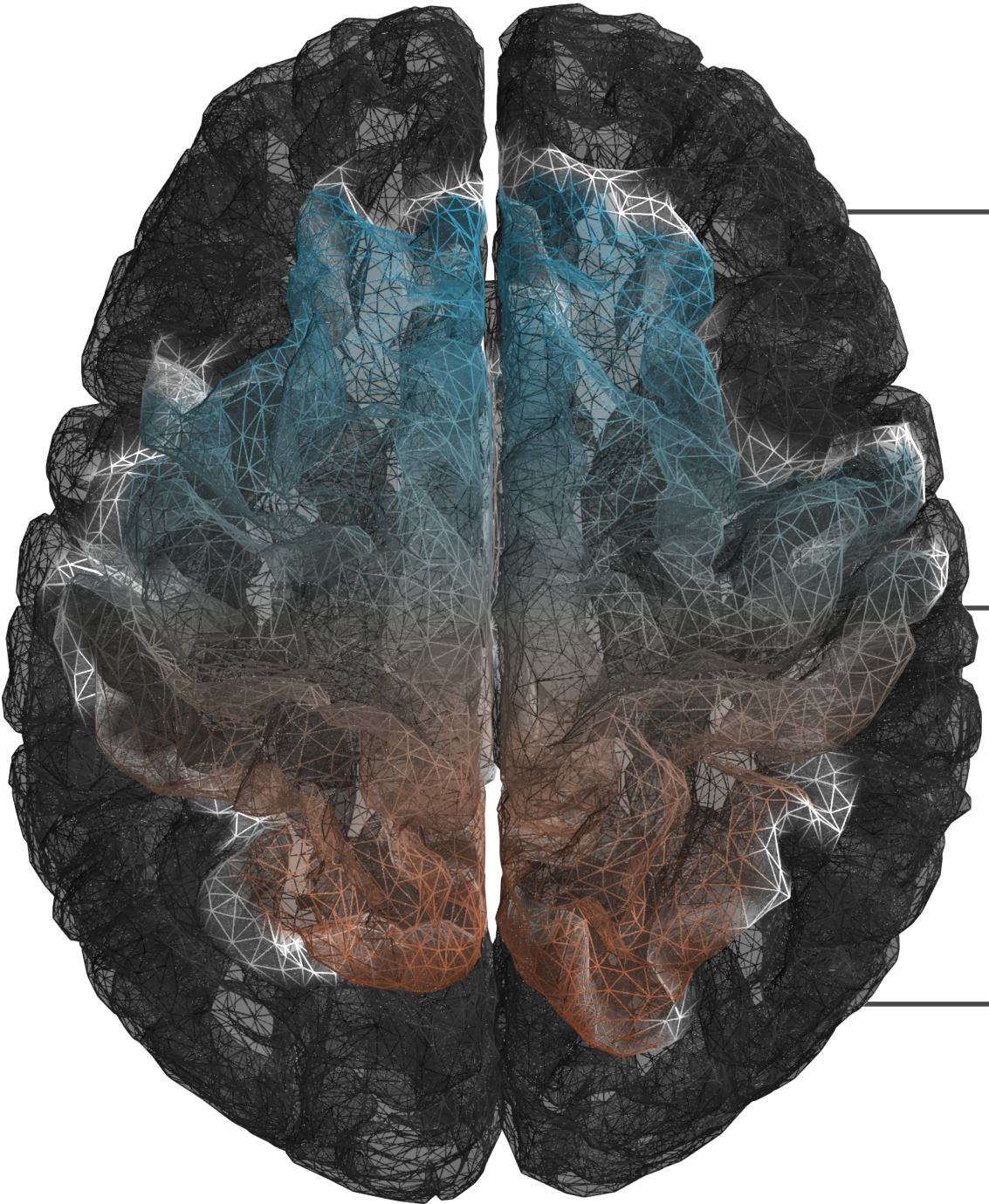
7

Predicting mortality of individual patients with COVID-19: a multicentre Dutch cohort

2021

M.C. Ottenhoff, L.A. Ramos, W. Potters, M.L.F. Janssen, D. Hubers et al. on behalf of The Dutch COVID-PREDICT research group

Abstract

Objective: Develop and validate models that predict mortality of patients diagnosed with COVID-19 admitted to the hospital. **Design:** Retrospective cohort study. **Setting:** A multicentre cohort across ten Dutch hospitals including patients from February 27 to June 8 2020. Participants: SARS-CoV-2 positive patients (age $\geq$ 18) admitted to the hospital. **Main Outcome Measures:** 21-day all-cause mortality evaluated by the area under the receiver operator curve (AUC), sensitivity, specificity, positive predictive value and negative predictive value. The predictive value of age was explored by comparison with age-based rules used in practice and by excluding age from the analysis. **Results:** 2273 patients were included, of whom 516 had died or discharged to palliative care within 21 days after admission. Five feature sets, including premorbid, clinical presentation and laboratory & radiology values, were derived from 80 features. Additionally, an ANOVA-based data-driven feature selection selected the ten features with the highest F-values: age, number of home medications, urea nitrogen, lactate dehydrogenase, albumin, oxygen saturation (%), oxygen saturation is measured on room air, oxygen saturation is measured on oxygen therapy, blood gas pH and history of chronic cardiac disease. A linear logistic regression (LR) and non-linear tree-based gradient boosting (XGB) algorithm fitted the data with an AUC of 0.81 (95% confidence interval 0.77 to 0.85) and 0.82 (0.79 to 0.85), respectively, using the ten selected features. Both models outperformed age-based decision rules used in practice (AUC of 0.69, 0.65 to 0.74 for age $>$ 70). Furthermore, performance remained stable when excluding age as predictor (AUC of 0.78, 0.75 to 0.81). **Conclusion:** Both models showed good performance and had better test characteristics than age-based decision rules, using ten admission features readily available in Dutch hospitals. The models hold promise to aid decision-making during a hospital bed shortage.

7.1 Introduction

The first wave of the COVID-19 pandemic had a dramatic effect on our society and severely disrupted our daily lives, economies and healthcare systems. During the peak of the first wave, hospitals and intensive care units (ICU) throughout Europe were overwhelmed and resources were exhausted. Implementation of public health policies reduced the infection rate; however, there is a considerable risk that relaxation of these policies leads to a next pandemic wave, which is already seen throughout European countries. Given the novelty of the virus, accurate information about the clinical course and prognosis of individual patients is still largely unknown, which led to the use of crude limits to unilaterally withhold advanced life support measures to face the large numbers of pulmonary insufficient patients during the first wave. Although criticized, several hospitals in Europe have already solely used age as a triage criterion [1]. Many publications have developed and evaluated triage selection criteria, but there remains a significant knowledge gap and the final criteria are subject to socio-ethical debate [2–4]. Preferably, triage is averted, but when necessary, the decision should be guided by evidence-based medical criteria. Since March 2020, many studies have been published regarding the clinical characteristics of patients suffering from a SARS-CoV-2 infection in both smaller (n=58 [5], n=200 [6]) and larger cohorts (n > 5000 [7–9]). However, these studies have reported notable differences in clinical characteristics that were associated with an adverse outcome. Importantly, these studies only provide information about clinical characteristics and risk factors on the group level and therefore do not provide information about the prognosis for individual patients. Prognostics models using multivariable analysis, such as [7] and [9] could be of great value during triage, especially when tailored towards individual prediction. These models can provide information about the individual patients' chance of survival, despite largely unknown underlying risk factors. Within the ongoing socio-ethical debate in the Netherlands, whether age should be included in the triage selection criteria, a predictive model could allow to exclude age or to include it together with clinical characteristics. Wynants et al. 2020 [10],

reviewed COVID-19 prediction models, identifying 145 prediction models of which 23 were tailored towards predicting mortality. The authors identified that all studies were at high risk of bias and are likely to underperform in clinical practice. However, a recent paper, not yet reviewed by Wynants et al., showed promising results on predicting mortality with excellent performance, using a very large cohort (n > 50.000) from the United Kingdom [11]. The uncertainty and risk of bias in almost all published COVID-19 related prognostic models, stresses the importance of thorough methodology in variable selection, internal and external model validation and performance evaluation [10]. In addition, a constant interplay between data scientists and clinicians must be in place during model development. Furthermore, studies developed and performed independently with similar methodology are more valuable than ever to reduce the uncertainty of published models and the risk of spurious publications [12, 13]. Therefore, a prognostic model was developed and evaluated that predicts 21-day all-cause mortality; utilizing data from 2273 SARS-CoV-2 infected patients from 10 hospitals across the Netherlands.

7.2 Materials and Methods

Data collection

Data were included from 10 Dutch hospitals varying from small to large peripheral hospitals to large academic centres. For an up-to-date overview of the including centres, see www.covidpredict.org. Clinical data were derived from electronic health records, pseudonymised and stored in the database (Castor EDC, Amsterdam, The Netherlands) by each hospital independently. Data collection started with the first admitted patients in the included centres. This was after the first confirmed case in the Netherlands on February 27, 2020. Records were included up to an admission date up until June 8th when the Dutch admission rates sharply decreased [14]. Inclusion criteria were admission in a hospital, age $\geq$ 18 years, a positive SARS-CoV-2 PCR before or during admission, or a CO-RADS CT thorax score $\geq$ 4 at admission. All patients were included consecutively. Retrospective data collection was based on the rapid COVID-19 case report form (rCCRF) developed by the WHO [15]. After consulta-

tion with several specialist consultants and an evaluation of the COVID-19 literature (mainly from China and Italy), additional clinical and laboratory features were added to the rCCRF. All included variables can be found in supplementary table 1. The study protocol was reviewed by the medical ethics committees of the Amsterdam University Medical Centers (Amsterdam UMC; 20.131) and Maastricht University Medical Center (MUMC; 2020-1323). Given the exceptional circumstances related to the COVID-19 crisis and in accordance with national guidelines and European privacy law, the need for informed consent was waived and an opt-out procedure was communicated by press release. Despite this, individual centres used local guidelines to obtain consent retrospectively from patients or representatives. In all centres, measures were taken to ensure adequate and safe data pseudonymisation and storage.

Outcome definition

To support the decision of (ICU) treatment during scarcity at hospital admission, we aim to predict the unfavourable outcome of COVID-19 patients at hospital admission. Given the amount of data, predicting each possible outcome, such as mortality, palliative care, discharge, and hospitalization, could increase the risk of biased models and overfitting. Therefore, the prediction goal was modelled as a binary classification problem, where an unfavourable outcome corresponds to patients that either died or were discharged for palliative care within 21 days after hospital admission. Palliative discharge is end-of-life care that focuses on patient comfort rather than treatments with curative intentions. A favourable outcome corresponds to patients that are discharged to home, nursing homes or rehabilitation units within 21 days and patients that are alive and still hospitalized at 21 days after hospital admission. Patients that were still hospitalized but shorter than 21 days, transferred to other hospitals (including transfers to participating hospitals), re-admitted or have an unknown outcome were excluded from further analysis.

Data processing and quality

The rCCRF was filled in manually by a large team of researchers and doctors because the electronic patient dossiers in the different hospitals could not be coupled to the Castor database. The rCCRF and additional features resulted in a large number of features (> 400). A consensus meeting with clinicians was held (April 18th, 2020) to remove features that were not available at hospital admission, not within the standard admission laboratory values or at risk of bias. This resulted in a feature set of 80 features. These 80 features were then divided into 6 sets: (1) premorbid characteristics (age, gender, occupation and past medical history, n=24), (2) clinical characteristics at admission (n=14), (3) laboratory and radiology findings at admission (n=42), (4) the combination of set 1 and 2 (n=38), (5) all features (n=80) and (6) a data-driven selection from all features (n=10). The process of data-driven selection is described further in the modelling process section. The decision to use 10 variables was a practical one, in an attempt to balance fewer variables for easier application in practice and more variables to inform about important features. A complete overview of all features per set is shown in supplementary Table 1 and numerical characteristics per set are shown in supplementary Table 2. The resulting features were checked for physiologically implausible outliers by two authors (MA/DH). Some features contained high but plausible values and were therefore not removed (e.g. creatinine kinase). Furthermore, collinearity was assessed by a Pearson correlation matrix (supplementary Figure 1). No variables were removed due to high collinearity.

Predictive modelling

Ultimately, the obtained models could change the clinicians' decision and thus could directly influences the life of a patient. It is therefore of utmost importance that the obtained models are both robust and interpretable [16]. To comply with these requirements, two models with a fundamentally different modelling approach were selected: a logistic regression (LR) that fits the data linearly, and a tree-based gradient boosting algorithm that fits the data non-linearly. The models were im-

plemented using the Python 3 libraries Scikit-learn [17] and XGBoost (XGB) [18], respectively. Both models can be interpreted relatively easy and XGB often shows state-of-the-art results in multiple tasks. The models were trained and validated using leave-one-hospital-out cross-validation (LOHO-cv). By iteratively training the models on all but one hospital and performance testing on the left-out hospital, the performance of the model represents the ability to predict the outcome on independent data and thereby incorporate possible data heterogeneity between hospitals. To prevent skewed performance on individual folds due to a small number of samples, we combined the data from the two hospitals with the smallest number of samples and considered them as a single hospital in LOHO-cv for further analysis. Additional to LOHO-cv, internal 10-fold random sub-sampling cross-validation using data from all hospitals was performed to facilitate a comparison of the results to other studies that typically only perform internal cross-validation.

Modelling process

Features that had more than 50% missing values and subsequently patient records that had more than 80% missing values were removed. The remaining missing values were imputed using Bayesian ridge regression, which is inspired by the MICE method [19], and implemented using the IterativeImputer from the Sci-Kit Learn library. Only one dataset per imputation was used since the disadvantages of single imputation are most apparent in small datasets with less than 100 events [20]. This imputation method models the missing values in each feature as a function of all other features and therefore provides a more sophisticated approach than the traditional imputation methods, such as using mean, median or mode imputation [19]. After imputation, each feature was scaled to its interquartile range (IQR). IQR scaling is known to be robust to outliers and often gives better results than z-score or minmax scaling [21]. Non-linear interactions between continuous variables can be taken into account by a non-linear model like XGB, thus splines were not included to prevent an unnecessary increase of the feature space [22]. The data was then split into folds using LOHO-cv, where each iteration consists of a training

fold with eight hospitals and a test fold with one hospital. The data-driven feature selection of set (6) was performed on the training fold by selecting the ten features showing the highest ANOVA F-value. Because for each iteration, the training fold consists of eight different hospitals, the selected features with the highest F-values can differ due to heterogeneity between hospitals. To be able to describe the ten most predictive features in further analysis, the features selected most often over all iterations are presented. If two feature sets are selected equally often, the set with the highest summed F-values was chosen. Both missing value imputation and feature selection were performed independently on the training and test set. After feature selection, both models were fitted and parameters optimized by a 50-iteration randomized grid search using a stratified shuffle split cross-validation. A schematic overview of all the processing steps is shown in Figure 1 and the grid search parameters are shown in supplementary Table 3. All code in the pipeline was implemented using the Scikit-learn python package [17]. To adhere to guidelines on transparent reporting of multivariable prediction models, the TRIPOD checklist is included in supplementary table 4 [23]. All code used in this paper, the final model and a calculator is available at DOI:10.5281/zenodo.4077342. A screenshot of the calculator is shown in supplementary Figure 2.

Performance analysis

Model discrimination was assessed by area under the curve (AUC), sensitivity, specificity, positive predictive value (PPV) and negative predictive value (NPV). Except for AUC, the metrics require a binary classification instead of likelihood and therefore the cut-off threshold was tuned to the shortest distance to the upper-left corner in the receiver operating curve (ROC) plot, which was named as the 'optimal' threshold in further analysis. In addition, a confusion matrix was derived over the complete dataset and for each centre, also tuned to the optimal threshold. Furthermore, model calibration is shown in supplementary Figure 3.
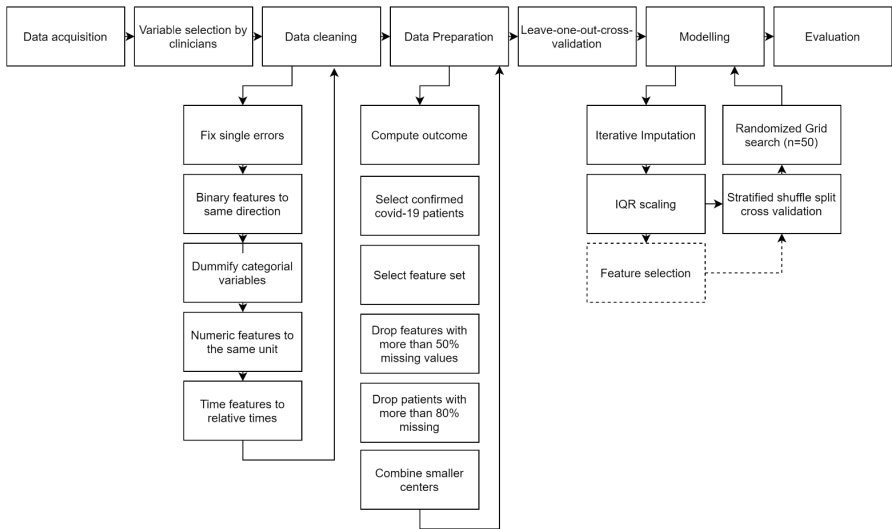
Figure 7.1: A schematic overview of all steps involved data acquisition to model evaluation. The dotted line depicts the step only used during feature selection of the 10 best features.

Feature importance

Feature importance of models is described using SHAP (SHapley Additive exPlanations) [24], a game-theoretic approach to explain the output of any machine learning model. SHAP computes the average contribution of all features by permuting all of them and subsequently evaluating the error in the prediction for when a given feature is either included or not in the model. With SHAP, the impact of low and high values of a given feature on the models' predictions can be evaluated, as well as how impactful the feature is in predicting the correct class [24].

Subgroup analysis for ICU admitted patients

During a large influx of patients suffering from life threatening lung infections, it is most likely that the ICU is exhausted first due to the low bed count and invasive ventilation capacity. It is therefore important to analyse whether the model also performs well on ICU admitted patients,

as triage might be dependent on ICU capacity. In the Netherlands, triage was prevented by distributing patients to districts with fewer admissions or German hospitals. However, possible bias may already be present in the selection of patients, because, for example, certain patients might not be admitted to the ICU because of old age, premorbid characteristics, presentation with multi-organ failure and patients' own treatment restraints wishes. For these reasons, both LR and XGB performances were assessed by training on the complete dataset and the ICU patient subgroup.

Age as feature

To compare the models to clinical practice, the performance was compared with two age-based decision rules that have been applied in practice during the crisis [1]. The rules were translated as follows: 1) If age is above 70 then the outcome is considered unfavourable and 2) If age is above 80 then the outcome is considered unfavourable. Furthermore, it was assessed whether age is important for the final prediction to be able to contribute to the ongoing socio-ethical debate in the Netherlands. In July 2020, a discussion between ethicists, medical professionals and policy-makers was started about criteria for triage to decide which patients receive ICU care during acute hospital care shortage. The main point of discussion was that the Dutch government was firmly opposed to using an age-based decision rule because it violates the Dutch constitution, which states that everyone should be treated equal and discrimination on any ground is illegal. To contribute to this discussion, the effect of age on the best performing model was assessed, by retraining the model on the same feature set, while excluding age as a feature.

Patient and Public involvement

This study was a rapid response to an international public health emergency. Patients were not involved in any stage of this study.

7.3 Results

Patient population

The database included 2527 patients from ten different hospitals on June 8, 2020. 223 patients were excluded because it was not possible to retrieve an outcome for these patients: patients that were still in the hospital, but less than 21 days (n=53), patients transferred to another hospital (n=113), patients that were discharged and re-admitted (n=55) and patients where the outcome was listed as unknown (n=2). In addition to these 223 excluded patients, 31 patients were excluded because they did not have a confirmed COVID-19 infection. After exclusion, 2273 patient remained to be included in further modelling and analysis.
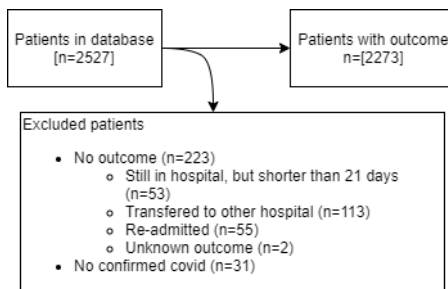
Figure 7.2: Flow diagram of patients excluded for further analysis.

Of these 2273 included patients, 1757 had a favourable outcome and 516 had an unfavourable outcome. Of the 1757 patients with a favourable outcome, 1195 were discharged home and not re-admitted patients, 76 were discharged to a nursing home, and 232 were discharged to a rehabilitation unit. In addition, 254 were still in the hospital at 21 days after admission (112 at the ward or medium care and 142 in the ICU). Of the 516 patients with an unfavourable outcome, 509 patients died and 7 patients were discharged to palliative care. See Figure 2 for an overview. To better balance the samples per hospital, the two smallest hospitals (n=59 and n=70) were combined. The resulting ratio of unfavourable outcome / total patients per hospital is 19% (n=261), 14% (n=169), 10% (n=118), 31% (n=317), 14% (n=113), 21% (n=401), 27% (n=325), 27% (n=440) and 19% (n=129).

Feature description

Two features, history of smoking and alcohol abuse, were removed because of multi-interpretable questions in the rCCRF. One feature was

removed from the Clinical presentation feature set and eleven features were removed from Laboratory & Radiology feature set for missing more than 50% values. No patient records were excluded for missing more than 80% values. After preprocessing, Premorbid and Clinical presentation features had 2.8% and 4.0% missing values, respectively. The admission Laboratory and Radiology features showed 21.6% missing values. See supplementary table 1 and 2 for a complete overview of features and missing values. Descriptive statistics of a selection of features are shown in table 1.

Variables		Missing	Overall	Favourable outcome	Unfavourable outcome	Adjusted p-value
Total Patients			2273	1758	516	
Age, median [Q1, Q3]		19	69.0 [58.0,78.0]	65.0 [55.0,75.1]	77.1 [71.0,83.1]	p<0.001***
Gender, n (%)		0				
	Female		858 (37.7)	690 (39.3)	168 (32.6)	
	Male		1415 (62.3)	1067 (60.7)	348 (67.4)	
History of Hypertension, n (%)		30				p<0.001***
	No		1207 (53.8)	998 (57.7)	209 (40.8)	
	Yes		1036 (46.2)	733 (42.3)	303 (59.2)	
History of Diabetes with complications, n (%)		64				p<0.001***
	No		2044 (92.5)	1608 (94.4)	436 (86.3)	
	Yes		165 (7.5)	96 (5.6)	69 (13.7)	
History of Diabetes without complications, n (%)		69				p<0.001***
	No		1789 (81.2)	1412 (83.0)	377 (75.1)	
	Yes		415 (18.8)	290 (17.0)	125 (24.9)	
History of asthma, n (%)		55				p>0.05
	No		1988 (89.6)	1524 (89.0)	464 (91.7)	
	Yes		230 (10.4)	188 (11.0)	42 (8.3)	
History of liver disease, n (%)		57				p>0.05
	No		2194 (99.0)	1693 (99.0)	501 (99.0)	
	Yes		22 (1.0)	17 (1.0)	5 (1.0)	
History of rheumatologic disorder, n (%)		43				p<0.05*
	No		1981 (88.8)	1549 (89.9)	432 (85.2)	
	Yes		249 (11.2)	174 (10.1)	75 (14.8)	
History of autoimmune and/or inflammatory diseases, n (%)		62				p<0.05
	No		2027 (91.7)	1559 (91.5)	468 (92.3)	
	Yes		184 (8.3)	145 (8.5)	39 (7.7)	
History of chronic cardiac disease, n (%)		36				p<0.001***
	No		1539 (68.8)	1271 (73.6)	268 (52.4)	
	Yes		698 (31.2)	455 (26.4)	243 (47.6)	
History of chronic hematologic disease, n (%)		50				p<0.05
	No		2133 (96.0)	1648 (96.0)	485 (95.7)	
	Yes		90 (4.0)	68 (4.0)	22 (4.3)	
History of chronic kidney disease, n (%)		45				p<0.001***
	No		1987 (89.2)	1566 (91.3)	421 (82.2)	
	Yes		241 (10.8)	150 (8.7)	91 (17.8)	
History of chronic neurological disorder, n (%)		45				p<0.001***
	No		1921 (86.2)	1519 (88.4)	402 (79.0)	
	Yes		307 (13.8)	200 (11.6)	107 (21.0)	
History of chronic pulmonary disease (not asthma), n (%)		47				p<0.001***
	No		1790 (80.4)	1419 (82.5)	371 (73.2)	
	Yes		436 (19.6)	300 (17.5)	136 (26.8)	

Table 7.1: Patients characteristics per outcome group and a selection of features. P-values were calculated using a t-test and corrected for multiple comparisons by Bonferroni correction. ***: p<0.001, **: p<0.01, *: p<0.05

Overall model performance

XGB and LR performed equally on the premorbid set with an AUC of 0.77 (95%-CI, 0.73 to 0.81) and 0.77 (0.72 to 0.81), respectively. On all

other feature sets, XGB performed better than LR, although most 95% confidence intervals overlapped. Both XGB and LR achieved the highest AUC on the 10 best features (0.82, 0.79 to 0.85 and 0.81, 0.77 to 0.85, respectively). Figure 3a shows a comparison of the AUCs per feature set, and Figure 3b the confusion matrix of XGB trained on the 10 best features. Sensitivity and specificity were comparable between the algorithms. Overall, the NPV was high and the PPV was low, as the number of patients with a favourable outcome was considerably higher than the number of patients with an unfavourable outcome. This implies that the model can make accurate predictions of favourable outcomes, but less accurate predictions of unfavourable outcomes. All results are shown in table 2. For an in-depth overview of the results per fold, see supplementary table 5. The results from internal cross-validation were comparable and shown in supplementary table 6. The between-hospital performance variation was small for both algorithms, shown by the small 95% confidence intervals in AUC of 0.02 to 0.06 and a low standard deviation (0.01). LR showed larger confidence intervals (0.04 to 0.07) with equal standard deviation (0.01). The overall standard deviation for all folds is small, and the comparison between internal cross-validation and LOHO-cv shows only minor differences in results between these approaches, reducing the risk of over-optimistic results. Between models, XGB fitted the data more robustly than LR, supported by the relatively equal ratios between correct and incorrect predictions, as shown in Figure 4, which shows the confusion matrix per hospital for XGB-10 best predicting features using the optimal threshold derived from the complete dataset.

Performance stability over time

With increased duration of stay within the hospital, the uncertainty of the patients' outcome may also increase. The patient's chance of survival might change because patients that have a longer hospital stay are likely to have a more complicated clinical course and/or get different types of treatments. Additionally, prolonged hospital stay simply allows more events to happen. To assess whether the models' performance changes based on the duration of hospital stay, the patients were split per dura-
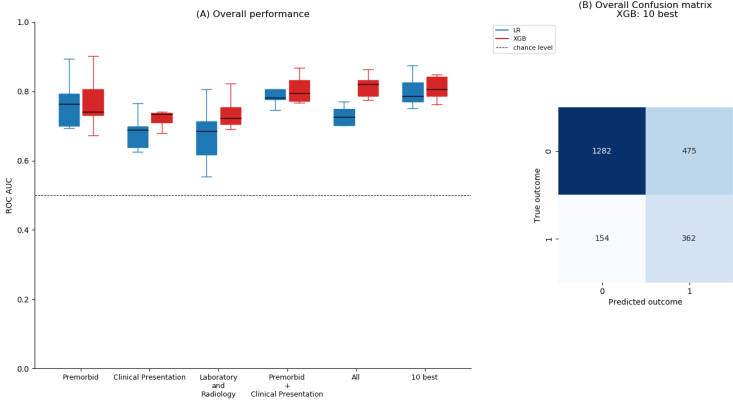
Figure 7.3: Panel A: Overall performance of both models per feature set. All models perform well above chance level. XGB generally performs better than LR, except on the premorbid feature set, where both models performed equally. The highest performance was achieved by XGB on both all features and the 10 selected features. Panel B: The confusion matrix of the best performing models, XGB trained on the 10 selected features. The prediction threshold was tuned to the shortest distance to the upper left corner of the AUC plot to create the 'optimal' binary prediction.

tion of stay and subsequently, the performance per group was assessed. The result, presented in Figure 5, shows that model performance does not deteriorate as the hospital duration increases, as the relative correct predictions remain between 0.6 and 0.9 and no trend is shown.

Feature importance

The 10 features selected most often were, in order of highest f-value to lowest f-value: age, urea nitrogen, number of home medications, oxygen saturation (%), history of chronic cardiac disease, oxygen saturation is measured on room air, oxygen saturation is measured on oxygen therapy, blood Lactate Dehydrogenase (LDH), blood albumin and blood gas pH value. Blood gas pH is measured from arterial, venous and capillary samples, of which 90.7% of the pH values are arterial measurements. The two 'oxygen is measured on' features are binary features that de-
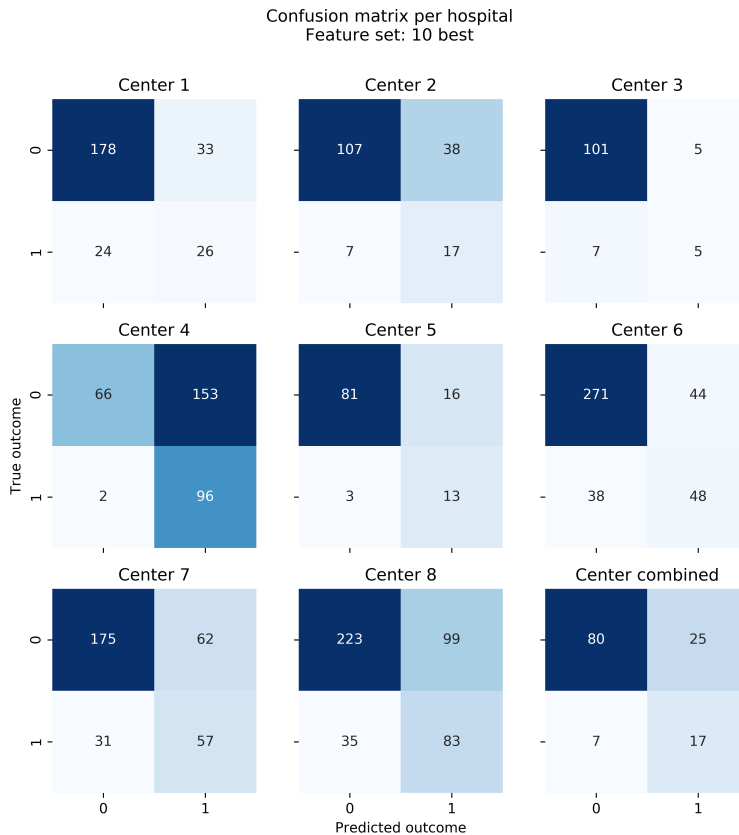
Figure 7.4: Confusion matrix per centre as predicted by XGB trained on the 10 selected features. The prediction threshold is optimized by the shortest distance to the upper-left corner in the ROC plot of the complete dataset. All matrices show comparable distributions, though centre 4 shows relatively many false positives.
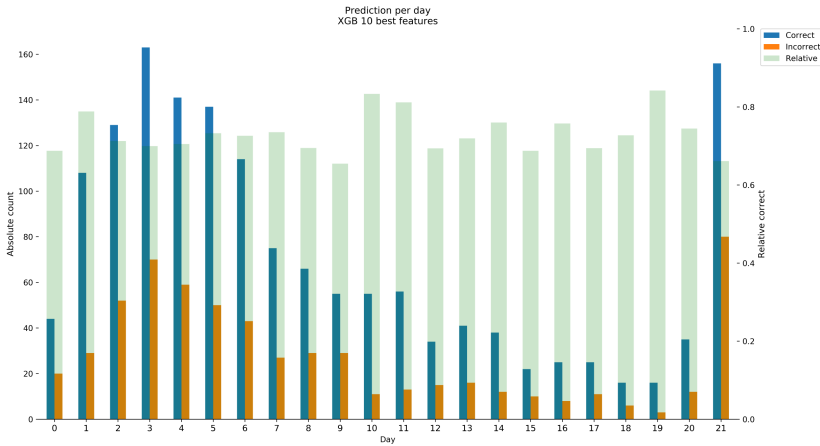
Figure 7.5: Performance per day for the XGB trained on the 10 selected features. The left y-axis shows the absolute number of correct predictions and the right y-axis the relative number of correct predictions. Relative performance was calculated by correct / (correct + incorrect) and was well above chance level (0.5) for all days. The results indicate robust performance as the relative performance showed no decrease over time while varying between 0.6 and 0.9. The absolute performance shows that most patients have an outcome (both favourable and unfavourable within one week after admission. A high number of patients is seen on day 21, which is caused by the aggregation of all patients that are in the hospital 21 days or longer. LR on the 10 best features shows similar performance (Figure not shown).

termine whether the oxygen saturation (%) is measured on room air or during oxygen therapy. The features were chosen independently of the choice of the model; therefore, the selected features were the same for both LR and XGB. Figure 6a and 6b show the SHAP values per feature based on XGB trained on all features. For readability, only the top 20 features are shown. The features selected by the ANOVA in pre-training are also present in the top features computed by the SHAP values in post-training, which strengthens the likelihood of these features being the most important features within this dataset. This is also shown by the fact that LR scored notably higher by using the 10-best features than using all features and XGB showing equal performance using 10-best or all

Classifiers	Feature set	AUC	Sensitivity	Specificity	PPV	NPV
LR	Premorbid	0.77 (0.72-0.81)	0.73 (0.61-0.84)	0.71 (0.64-0.78)	0.39 (0.35-0.44)	0.91 (0.88-0.95)
	Clinical Presentation	0.67 (0.62-0.71)	0.60 (0.51-0.68)	0.63 (0.57-0.69)	0.30 (0.22-0.38)	0.86 (0.83-0.90)
	Laboratory and Radiology	0.66 (0.59-0.73)	0.65 (0.47-0.83)	0.54 (0.34-0.73)	0.25 (0.16-0.34)	0.83 (0.74-0.91)
	Premorbid + Clinical Presentation	0.79 (0.75-0.83)	0.71 (0.62-0.80)	**0.71 (0.66-0.75)**	0.38 (0.32-0.43)	0.91 (0.89-0.93)
	All	0.71 (0.67-0.76)	0.62 (0.52-0.73)	0.70 (0.62-0.78)	0.36 (0.28-0.44)	0.88 (0.85-0.92)
	10 best	**0.81 (0.77-0.85)**	**0.77 (0.68-0.85)**	0.71 (0.65-0.77)	**0.41 (0.36-0.45)**	**0.93 (0.90-0.95)**
XGB	Premorbid	0.77 (0.73-0.81)	0.68 (0.54-0.81)	0.60 (0.39-0.82)	0.36 (0.29-0.43)	0.68 (0.44-0.92)
	Clinical Presentation	0.73 (0.71-0.74)	0.69 (0.61-0.77)	0.64 (0.59-0.69)	0.33 (0.26-0.40)	0.89 (0.87-0.92)
	Laboratory and Radiology	0.72 (0.66-0.77)	0.68 (0.60-0.75)	0.63 (0.57-0.68)	0.31 (0.27-0.35)	0.88 (0.84-0.92)
	Premorbid + Clinical Presentation	0.81 (0.78-0.83)	**0.76 (0.67-0.85)**	0.62 (0.47-0.78)	0.36 (0.29-0.44)	0.81 (0.62-1.00)
	All	**0.82 (0.79-0.85)**	0.66 (0.54-0.78)	0.77 (0.65-0.89)	**0.47 (0.42-0.52)**	0.91 (0.88-0.95)
	10 best	**0.82 (0.79-0.85)**	0.67 (0.57-0.77)	**0.75 (0.63-0.86)**	0.44 (0.40-0.48)	**0.91 (0.88-0.94)**

Table 7.2: Evaluation metrics for both classifiers for each feature set. The average and 95% confidence intervals over all LOHO-cv iterations are presented. Values in bold represent the best performance for each metric per classifier. The premorbid feature set includes age, gender, occupation and past medical history. AUC: area under the curve; PPV: positive predictive value; NPV: negative predictive value; LR: logistic regression; XGB: extreme gradient boosting.

features. Analysis of SHAP values for LR on all features (supplementary Figure 4) showed that the linear LR model was not able to capture the non-linear predictive value of the age feature, as it was ranked as 4th. Nonetheless, the highest-ranked features for LR show importance and a direction of association consistent with the literature [25, 26].

Subgroup analysis for ICU patients

Of the 2273 included patients, 384 (17%) were admitted to the ICU at any time during the hospitalization. LR showed the highest overall performance on ICU patients with an AUC of 0.71 (0.65 to 0.78). XGB showed the highest performance on both Premorbid and Premorbid + Clinical presentation features (0.69, 0.59 - 0.79). See table 3 for all results. For non-ICU patients, LR showed highest performance on the 10-best features (AUC 0.85, 0.81 - 0.88) and XGB on all features (AUC 0.86, 0.82 - 0.89). Compared with the results on the complete dataset, the performance dropped notably on ICU patients, decreasing in AUC by 0.04 to 0.20. The confidence intervals also increased, overall ranging from 0.03 to 0.18. The decreased discriminative power of the models is considered acceptable, as the initially best-performing feature sets decreased only slightly and retained small confidence intervals. The decrease was expected, given that performance on a smaller subgroup is inevitably

Variable impact on model output
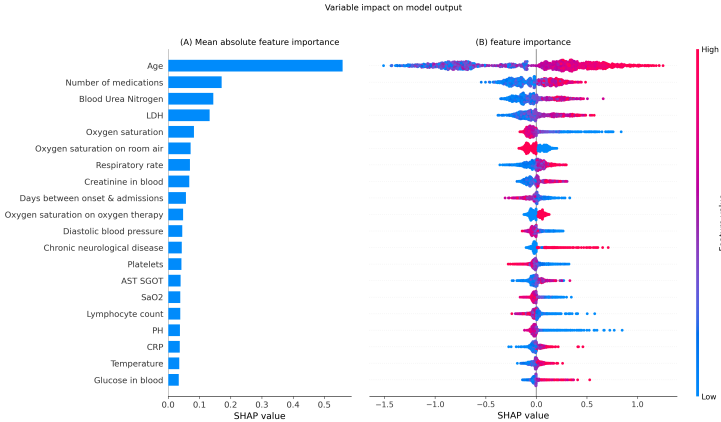
Figure 7.6: SHAP values of XGB trained on all features. To prevent readability issues, only the top 20 features are shown and the SHAP value range is set from -1.5 to 1.5, visually cutting of a few outliers. The colour of each data points depicts the height of the value, where red corresponds to high values and blue to low values. SHAP values above 0 suggest a positive association with the outcome. Given the outcome is defined as mortality within 21 days, the positive SHAP values translate to association with higher mortality.

lower. In addition, the prognosis of the outcome of ICU admitted patients might change, for example, due to receiving distinct interventions only available at the ICU. Inspection of sensitivity and specificity indicates that the lower performance was due to a decrease in sensitivity rather than specificity (see supplementary table 6). The main objective in times of ICU admission at the time of ICU bed shortage is to correctly identify those patients that would benefit from intensive care. Therefore, the models may still be considered for application in practice, despite lower overall performance. Nonetheless, a more tailored approach might capture the unique characteristics of ICU patients better.

Comparison with age-based rules for whole cohort
Of the 2273 patients, the age of 19 patients was missing and these were thus excluded for this analysis. Of the remaining 2254 patients, 1061

Classifiers	Feature set	AUC - ICU patients	AUC - non-ICU patients
LR	Premorbid	**0.71 (0.66-0.76)**	0.81 (0.77-0.84)
	Clinical Presentation	0.51 (0.37-0.66)	0.68 (0.64-0.72)
	Laboratory and Radiology	0.54 (0.45-0.63)	0.69 (0.61-0.76)
	Premorbid + Clinical Presentation	0.60 (0.42-0.78)	0.83 (0.80-0.86)
	All	0.63 (0.50-0.76)	0.75 (0.72-0.79)
	10 best	0.62 (0.44-0.80)	**0.85 (0.81-0.88)**
XGB	Premorbid	**0.69 (0.59-0.79)**	0.80 (0.76-0.83)
	Clinical Presentation	0.57 (0.41-0.72)	0.75 (0.72-0.77)
	Laboratory and Radiology	0.59 (0.52-0.66)	0.76 (0.69-0.83)
	Premorbid + Clinical Presentation	**0.69 (0.59-0.79)**	0.84 (0.81-0.87)
	All	0.68 (0.58-0.78)	**0.86 (0.82-0.89)**
	10 best	0.68 (0.57-0.79)	0.85 (0.82-0.88)

Table 7.3: Model performance on (non-)ICU subgroup. Values in bold represent the best performance per classifier per subgroup. The premorbid feature set includes age, gender, occupation and past medical history. AUC: Area under the curve, ICU: Intensive care unit, LR: Logistic regression, XGB = Extreme Gradient Boosting

were older than 70 and 415 were older than 80. The age-based decision criteria therefore 'predicted' that of age > 70, 1193 will survive and 1061 will die. For age > 80 the prediction was 1839 and 415, respectively. Age > 70 showed an AUC of 0.69 (0.65 to 0.74) whereas age > 80 showed a lower AUC (0.61, 0.57 to 0.65). Figure 7 shows the confusion matrices of LR and XGB trained on the 10-best features and both age-based decision criteria. To compare both models with the age-based rules, the results were tuned to the shortest distance to the upper left corner in the ROC plot. Both LR and XGB show a higher AUC than either age-based decision criteria. The results show that the presented models can outperform earlier applied triage rules during crises and can thus provide better information based on individual medical data.

Sensitivity analysis of age as feature

The best performing model, XGB-10, was retrained and evaluated without age as a feature. While expecting the performance to drop significantly, given that age was the most predictive feature by both the feature selection and SHAP analysis (Figure 6), the performance decreased only slightly from an AUC of 0.82 (0.79 - 0.85) to 0.78 (0.75 - 0.81). Even though there were no signs of troublesome collinearity (supplementary

Performance compared with age-based decision rule
Featureset: 10 best

LR
AUC: 0.81 (0.77 to 0.85)

XGB
AUC: 0.82 (0.79 to 0.85)

0	1218	526
1	111	399

0	1269	475
1	151	359

Age > 70
AUC: 0.69 (0.65 to 0.74)

Age > 80
AUC: 0.61 (0.57 to 0.65)

0	1073	671
1	120	390

0	1516	228
1	323	187
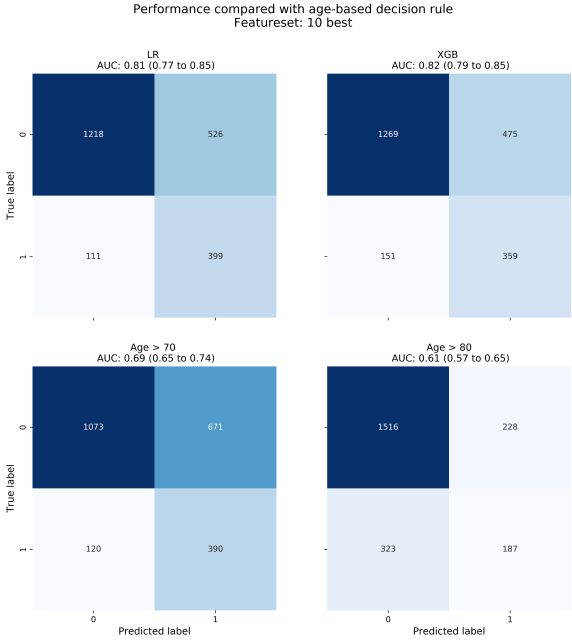
Figure 7.7: LR and XGB trained on the 10 selected features compared with two age-based decision rules. Both LR and XGB showed a higher AUC than both age-based rules. 19 patients did not have a value for age and were excluded for this analysis.

Figure 1), age did show high multicollinearity (variance inflation factor; VIF > 20). However, during model development, it was decided not to exclude features beforehand. Nonetheless, the high VIF indicates that the information present in age is latently present in two or more other features, which could explain the retained performance.

7.4 Discussion

We have shown that the mortality of individual COVID-19 patients can be predicted at hospital admission with good discrimination using both linear (LR; AUC 0.81, 0.77 to 0.85) and nonlinear (XGB; 0.82, 0.79 to 0.85) models with 10 features that are readily available in most hospitals. Both

models showed improved discrimination over age-based decision rules, used in practice during acute hospital bed shortage [2]. XGB trained on all 80 features and the 10 best features performed comparable, but the latter model may be preferred for easier translation to clinical practice. The presented models were trained on a large cohort, representing approximately 16% of the total COVID-19 related hospital admissions in the Netherlands during the first wave. [NICE, consulted October 7th][24]. Wynants et al. reported that most models were at severe risk of bias due to poor patient selection, predictor description and methodology [10]. The present study has addressed these issues by aiming to clearly describe the patient inclusion process of a large cohort, clearly defining an outcome measure and by using a standardized predictor format (rCCRF) from the WHO, expanded with potentially predictive variables curated by clinicians working in the COVID field. The models were calibrated by using nested cross-validation to prevent data leakage and validated by leave-one-hospital-out cross-validation. This location-based external cross-validation shows better results than classic cross-validation [27], although validation on an independent dataset remains preferred. Additional to LOHO-cv, the risk of overfitting was further reduced by regularizing both models, where regularization parameters were optimized using nested cross-validation on the training set. Furthermore, the internal cross-validation results shown in supplementary table 6 are similar to the results of LOHO-cv validation, indicating that the risk of overfitting on specific centres is low. An important note is that a good model fit was not shown on all feature sets, e.g. Laboratory & Radiology features or LR on all features. Additionally, analysis of the SHAP values of LR (supplementary Figure 4, showed that the predictive value of age was not well captured by LR, as the feature was only ranked as the fourth most predictive feature. Combined, XGB-10 is the recommended model, as it showed a good fit and capture the non-linear predictive value of age well.

The results shown in this study are similar to a large-scale study by knight et al 2020 that utilized a UK cohort ten-fold larger than this cohort and external validation [11]. The authors presented similar methods with similar results as this study, which strengthens the reliability

of both models and reducing the risk of reporting over-optimistic results. However, before application in practice the models need to be validated by an independent research group and for data in other countries. We have identified several uncertainties that may limit the current reliability of the models. Firstly, the skewed outcome distribution (516 events over 2273 records) in our cohort limits the calibration of our models (supplementary Figure 3). This becomes apparent in the decreased calibration for higher-risk patients, though it must be noted that the recommended model (XGB-10) retains good calibration. Secondly, the cohort represents Dutch hospitalized COVID-19 patients during the first wave of infections and might differ from current COVID-19 patients due to the availability of therapies like steroids or vaccination. The included features could be improved by adding some features that are known to be highly predictive such as d-dimer, presence of infiltrates on the chest x-ray and duration of symptoms before hospital admission. These variables were initially included in our data but had to be removed due to too many missing values. Additionally, the duration of symptoms before admission was anamnestic, decreasing its reliability due to the retrospective data collection. Lastly, some uncertainties arise from the outcome definition, defined as the chance of death or discharge to palliative care within 21 days after hospital admission. The outcome was defined as all-cause mortality instead of COVID-19 related mortality, and this might result in an overestimation of the predictive power of specific comorbidities. Furthermore, the cut-off point of 21 days was considered as a balanced choice between early outcome and eventual outcome. A shorter time frame might result in inaccurate outcomes and extending it would not have resulted in many more cases. However, some patients that were still at the hospital on day 21 might have an unfavourable outcome shortly after, resulting in a mislabelling of the patient, which overall might lead to an underestimation of mortality. Moreover, no follow-up of patients discharged to palliative care was implemented, possibly labelling patients with an erroneous unfavourable outcome. However, given that only seven patients (0.3% of all patients) were discharged to palliative care, we consider the risk negligible. Lastly, no bed shortage was experienced in the Netherlands and it is therefore unlikely that pri-

oritization towards specific patients biased the cohort.

Implications for clinicians and policymakers

The presented models show that a reliable prediction can be made based on ten features readily available in all Dutch and most worldwide hospitals: age, number of home medications, admission blood values urea nitrogen/LDH/albumin, oxygen saturation (%), blood gas pH and history of chronic cardiac disease. The models are thus easily applicable in practice and can improve the triage decision by providing a more objective medical foundation. We also showed that age as a feature is contributing towards a better prediction, but is not crucial. This implicates that policymakers can decide to exclude age when utilizing these models.

Unanswered questions and future research

This work shows a promising step towards a triage tool during a hospital bed shortage. However, given the rapidly improving medical care for COVID-19 patients and the lack of external validation, the data used during development are likely less representational of the current hospitalized COVID-19 patients. Additionally, the models are trained on a Dutch cohort and cannot be generalized to other countries. Lastly, it should be evaluated how the prediction of the models compare with the clinician expertise. Altogether, a validation study evaluating these unanswered questions would be the next step towards clinical implication.

7.5 Conclusion and Recommendation

Both LR and XGB showed good performance using the 10 best features, and outperformed age-based rules, with or without age included in the features. The results suggest that XGB using the 10 best features can improve decision making during an acute hospital bed shortage during a COVID-19 crisis and this model holds promise to be developed into a clinical tool.

7.6 Ethics approval

The ethical boards of the Amsterdam University Medical Centers (20.131) and Maastricht University Medical Center approved the study protocol (MUMC: 2020-1323)

7.7 Contributorship statement

Conceptualization: MO, LR, WP, MJ, RT, DP, CH, PK, PE, MS, JW, GW, MA, MB Data curation: MO, LR, WP, MJ, DH, DP, SS, MK, TD, MS, PN, JB, CW, DB, EH, AR, DR, KS, RD, LH, NG, GW, MA, MB Formal Analysis: MO, LR, WP, SH, EF, RT, CH, HM, MW, GW, MA, MB Investigation: MO, LR, SH, EF, WP, GW, MA, MB Methodology: MO, LR, SH, EG, RT, WP, GW, MA, MB Project Administration: WP, MJ, PK, PE, LF, MS, GW, MA, MB Software: MO, LR, WP Supervision: GW, MA, MB Validation: MO, LR, GW, MA, MB Visualization: MO, LR Writing – Original draft: MO, LR, WP, MJ, GW, MA, MB Writing – Review and Editing: MO, LR, IH, DP, CH, PK, PE, HM, SS, MK, TD, PN, JB, CW, JW, EH, AR, DR, KS, RD, LH, NG, RR, GW, MA, MB

7.8 Competing Interests

7.9 Funding

7.10 Data sharing statement

Not all patients provided active informed consent, and therefore data cannot be shared. The code used in this study is made publicly available and can be found at DOI:10.5281/zenodo.4077342

7.11 Transparency Statement

The lead author (MB) affirms that the manuscript is an honest, accurate, and transparent account of the study being reported; that no important aspects of the study have been omitted; and that any discrepancies from the study as originally planned (and, if relevant, registered) have been explained.

References

[1] Benjamin Herreros, Pablo Gella, and Diego Real De Asua. "Triage during the COVID-19 epidemic in Spain : better and worse ethical arguments". In: *Journal of medical ethics* 46 (2020), pp. 455–458. DOI: 10.1136/medethics-2020-106352.

[2] René Robert et al. "Ethical dilemmas due to the Covid-19 pandemic". In: *Annals of Intensive Care* 10.84 (2020). Publisher: Springer International Publishing, pp. 1–9. DOI: 10.1186/s13613-020-00702-7.

[3] Joseph Dahine, Daniela Ziegler, and Nicolay Ferrari. "Practices in Triage and Transfer of Critically Ill Patients: A Qualitative Systematic Review of Selection Criteria". In: *Critical Care Medicine* 8 (2020). ISBN: 0000000000, pp. 1–11. DOI: 10.1097/CCM.0000000000004624.

[4] Charles L Sprung et al. "Adult ICU Triage During the Coronavirus Disease 2019 Pandemic: Who Will Live and Who Will Die? Recommendations to Improve Survival*". In: *Critical Care Medicine* 48.8 (2020). ISBN: 0000000000, pp. 1196–1202. DOI: 10.1097/CCM.0000000000004410.

[5] Xiaobo Yang et al. "Clinical course and outcomes of critically ill patients with SARS-CoV-2 pneumonia in Wuhan, China : a single-centered, retrospective, observational study". In: *The Lancet Respiratory* 8.5 (2020). Publisher: Elsevier Ltd, pp. 475–481. DOI: 10.1016/S2213-2600(20)30079-5.

[6] Fei Zhou et al. "Clinical course and risk factors for mortality of adult inpatients with COVID-19 in Wuhan , China : a retrospective cohort study". In: *The Lancet* 395.10229 (2020). Publisher: Elsevier Ltd, pp. 1054–1062. DOI: 10.1016/S0140-6736(20)30566-3.

[7] Christopher M Petrilli et al. "Factors associated with hospital admission and critical illness among 5279 people with coronavirus disease 2019 in New York City : prospective cohort study". In: *British Medical Journal* 369.1966 (2019). ISBN: 0000000318006. DOI: 10.1136/bmj.m1966.

[8]   Safiya Richardson et al. "Presenting Characteristics, Comorbidities, and Outcomes Among 5700 Patients Hospitalized With COVID-19 in the New York City Area". In: *Journal of American Medical Association* 323.20 (2020), pp. 2052–2059. DOI: 10.1001/jama.2020.6775.

[9]   A B Docherty et al. "Features of 16 , 749 hospitalised UK patients with COVID-19 using the ISARIC WHO Clinical Characterisation Protocol". In: *Preprint* (2020).

[10]   Laure Wynants et al. "Prediction models for diagnosis and prognosis of covid-19 : systematic review and critical appraisal". In: *British Medical Journal* 19.369 (2020), p. 1328. DOI: 10.1136/bmj.m1328.

[11]   Stephen R Knight et al. "Risk stratification of patients admitted to hospital with covid-19 using the ISARIC WHO Clinical Characterisation Protocol : development and validation of the 4C Mortality Score". In: 2.September (2020). DOI: 10.1136/bmj.m3339.

[12]   Mandeep R Mehra et al. "Cardiovascular Disease, Drug Therapy, and Mortality in Covid-19". In: *The new England Journal of medicine* 102.1 (2020), pp. 1–7. DOI: 10.1056/NEJMoa2007621.

[13]   Mandeep R Mehra et al. "Hydroxychloroquine or chloroquine with or without a macrolide for treatment of COVID-19: a multinational registry analysis". In: *The Lancet* (2020). Publisher: Elsevier Ltd. DOI: 10.1016/S0140-6736(20)31180-6.

[14]   Yicheng Fang et al. "Sensitivity of Chest CT for COVID-19: Comparison to RT-PCR Yicheng". In: *Radiology* ().

[15]   World Health Organization. *Novel coronavirus (covid-19) - Rapid version*. 2020.

[16]   U K Biobank and Moofields Eye Hospital. "Towards trustable machine learning". In: 2.October (2018), pp. 709–710. DOI: 10.1038/s41551-018-0315-x.

[17]   Fabian Pedregosa, Ron Weiss, and Matthieu Brucher. "Scikit-learn : Machine Learning in Python". In: *Journal of machine learning research* 12 (2011), pp. 2825–2830.

[18]   Tianqi Chen and Carlos Guestrin. "XGBoost : A Scalable Tree Boosting System". In: *KDD '16: Proceedings of the 22nd ACM SIGKDD International Conference on Knowledge Discovery and Data Mining* (2016). ISBN: 9781450342322.

[19]   Karin Groothuis-oudshoorn. "mice : Multivariate Imputation by Chained". In: *Journal of statistical software* 45.3 (2011).

[20]   Teresa Neeman. "Clinical Prediction Models: A Practical Approach to Development, Validation, and Updating by Ewout W. Steyerberg". en. In: *International Statistical Review* 77.2 (2009). _eprint: https://onlinelibrary.wiley.com/doi/pdf/10.1111/j.1751-5823.2009.00085_22.x, pp. 320–321. DOI: 10.1111/j.1751-5823.2009.00085_22.x.

[21]   B Iglewicz et al. "Robust scale estimators and confidence intervals for location". In: *Understanding Robust and Exploratory Data Analysis*. 1983.

[22]   Jerome H. Friedman. "Multivariate Adaptive Regression Splines". In: *The Annals of Statistics* 19.1 (Mar. 1991). Publisher: Institute of Mathematical Statistics, pp. 1–67. DOI: 10.1214/aos/1176347963.

[23]   Gary S Collins et al. "Transparent reporting of a multivariable prediction model for individual prognosis or diagnosis (TRIPOD): the TRIPOD Statement". In: (2015), pp. 1–10. DOI: 10.1186/s12916-014-0241-z.

[24] Scott M Lundberg et al. "From local explanations to global understanding with explainable AI for trees". In: *Nature Machine Intelligence* 2.January (2020). ISBN: 4225601901389 Publisher: Springer US, pp. 56–67. DOI: 10.1038/s42256-019-0138-9.

[25] Ewout W. Steyerberg and Frank E. Harrell. "Prediction models need appropriate internal, internal-external, and external validation". eng. In: *Journal of Clinical Epidemiology* 69 (Jan. 2016), pp. 245–247. DOI: 10.1016/j.jclinepi.2015.04.005.

[26] Geoffrey D. Wool and Jonathan L. Miller. "The Impact of COVID-19 Disease on Platelets and Coagulation". In: *Pathobiology* 88.1 (Oct. 2020), pp. 15–27. DOI: 10.1159/000512007.

[27] I. R. König et al. "Practical experiences on the necessity of external validation". en. In: *Statistics in Medicine* 26.30 (2007). _eprint: https://onlinelibrary.wiley.com/doi/pdf/10.1002/sim.3069, pp. 5499–5511. DOI: 10.1002/sim.3069.

7.12 Supplementary materials

Premorbid	Clinical presentation	Laboratory / Radiology findings
Age	Bleeding (Haemorrhage)	Adenovirus PCR positive
AIDS / HIV	Days since infection before hospital admission	ALT
Asthma (physician diagnosed)	Diastolic blood pressure	aPTT
Autoimmune andor inflammatory diseases	Disturbed capillary refill	AST
Chronic cardiac disease, including congenital heart disease (not hypertension)	Heart rate	Bacteria in sputum cultured
Chronic hematologic disease	History of fever	Blood Albumin
Chronic kidney disease	Irregular heart rhythm	Blood cultures positive
Chronic neurological disorder	Respiratory rate	Blood Urea Nitrogen
Chronic pulmonary disease (not asthma)	Seizures	CO-RADS CT thorax score
Diabetes with complications	Shortness of breath (Dyspnea)	Blood Creatinine kinase
Diabetes without complications	Systolic blood pressure	Blood Creatinine value
Gender	Temperature	Blood CRP
Healthcare worker	Oxygen saturation	Blood D-dimer
Hypertension	Oxygen saturation measured on room air	Blood Ferritine
Immunosuppressive medication	Oxygen saturation on oxygen therapy	Blood Fibrinogen
Malignant neoplasm		FiO2 supplied
Microbiology worker		Blood Glucose
Mild liver disease		Blood Haemoglobin
Moderate or severe liver disease		Influenza PCR positive
Number of different medicine patient uses		Blood INR
Regular medicine use at home		Blood Lactate value
Rheumatologic disorder		Blood LDH
		Other Infectious Respiratory diagnosis confirmed
Rheumatologic disorder		PaO2 – Arterial blood gas
		PaO2 – Capillary blood gas
		PaO2 – Venous blood gas
		PaCO2 – blood gas
		PH value – blood gas
		Blood Platelets value
		Blood Potassium
		Blood PT
		SaO2 – Blood gas
		Blood Lymphocyte count
		Blood Neutrophil Count
		Blood Sodium
		Thoracic CT findings
		Blood Total Bilirubin
		Blood Total calcium
		Blood White blood cell count value
		Presence of infiltrates on lung imaging

Supplementary table 1 – Individual features per feature set (adapted from the rapid COVID-19 case report form. Removed values due to missing more than 50% of values are underlined. Blood gas pH values are measured from arterial (90.7%), venous (7.0%) and capillary (0.4%) samples. For 1.8% pH samples, the location is unknown.

Feature set	N features	N Features after preprocessing	Average absolute missing	Average relative missing (%)	Min missing	Max missing
Premorbid	24	22	63	2.8	0	349
Clinical presentation	14	15	92	4.0	0	336
Laboratory & radiology	42	33	490	21.6	0	1023
Premorbid + clinical presentation	38	37	75	3.3	0	349
All	80	70	271	11.9	0	1023

Supplementary table 2 – Feature set description before and after preprocessing. The average absolute missing, average relative missing, minimum missing per feature and maximum missing per feature are described after preprocessing. The Laboratory & Radiology feature set shows notably higher amount of missing values, likely because no all laboratory values are measured for each patient. In addition, some features were added at a later stage in development, resulting in missing values for patients already included. The degrees of freedom are equal to the amount of estimated parameters, which might vary from the initial amount of features due to removal and dummification of features.

Classifier	Parameter Name	Parameter Value
XGB	[Learning rate]	[0.1, 0.01, 0.001]
	[Gamma] Minimum loss reduction required to make a further partition on a leaf node of the tree	[0.1, 0.01, 0.001]
	[N estimators]	[100, 200, 300, 500, 700]
	[Subsample] Subsample ratio of the training instances	[0.5, 0.7, 0.9]
	[Colsample by tree] Parameters for subsampling the columns	[0.5, 0.6, 0.7, 0.8]
	[Max depth] Maximum depth of a tree	[2, 4, 6, 8]
LR	[Solver]	[Saga]
	[Penalty] Regularization penalty type	[Elasticnet, L2]
	[L1 Ratio] Ratio between L1 and L2 regularization	[0.0, 0.2, 0.4, 0.6, 0.8, 1.0]
	[C] Inverse regularization strength	[0.0, 0.001, 0.006, 0.046, 0.359, 2.783, 21.544, 166.81, 1291.55, 10000.0]

Supplementary table 3 - Hyper-parameters used for optimizing LR or XGB models. A 50-iteration randomized grid-search was used for both models. The values in square brackets under parameters name are the parameter names as per function in the code.

Section/Topic			Checklist Item	Page
Title and abstract				
Title	1	D;V	Identify the study as developing and/or validating a multivariable prediction model, the target population, and the outcome to be predicted.	4
Abstract	2	D;V	Provide a summary of objectives, study design, setting, participants, sample size, predictors, outcome, statistical analysis, results, and conclusions.	4
Introduction				
Background and objectives	3a	D;V	Explain the medical context (including whether diagnostic or prognostic) and rationale for developing or validating the multivariable prediction model, including references to existing models.	5
	3b	D;V	Specify the objectives, including whether the study describes the development or validation of the model or both.	5, 6
Methods				
Source of data	4a	D;V	Describe the study design or source of data (e.g., randomized trial, cohort, or registry data), separately for the development and validation data sets, if applicable.	7
	4b	D;V	Specify the key study dates, including start of accrual; end of accrual; and, if applicable, end of follow-up.	7
Participants	5a	D;V	Specify key elements of the study setting (e.g., primary care, secondary care, general population) including number and location of centres.	7
	5b	D;V	Describe eligibility criteria for participants.	7
	5c	D;V	Give details of treatments received, if relevant.	n/a
Outcome	6a	D;V	Clearly define the outcome that is predicted by the prediction model, including how and when assessed.	7, 8
	6b	D;V	Report any actions to blind assessment of the outcome to be predicted.	n/a
Predictors	7a	D;V	Clearly define all predictors used in developing or validating the multivariable prediction model, including how and when they were measured.	8, T2, ST1, ST4
	7b	D;V	Report any actions to blind assessment of predictors for the outcome and other predictors.	n/a
Sample size	8	D;V	Explain how the study size was arrived at.	7
Missing data	9	D;V	Describe how missing data were handled (e.g., complete-case analysis, single imputation, multiple imputation) with details of any imputation method.	8
Statistical analysis methods	10a	D	Describe how predictors were handled in the analyses.	8, 9
	10b	D	Specify type of model, all model-building procedures (including any predictor selection), and method for internal validation.	8, 9
	10c	V	For validation, describe how the predictions were calculated.	10, fig 1
	10d	D;V	Specify all measures used to assess model performance and, if relevant, to compare multiple models.	10
	10e	V	Describe any model updating (e.g., recalibration) arising from the validation, if done.	n/a
Risk groups	11	D;V	Provide details on how risk groups were created, if done.	n/a
Development vs. validation	12	V	For validation, identify any differences from the development data in setting, eligibility criteria, outcome, and predictors.	10, 11
Results				
Participants	13a	D;V	Describe the flow of participants through the study, including the number of participants with and without the outcome and, if applicable, a summary of the follow-up time. A diagram may be helpful.	12
	13b	D;V	Describe the characteristics of the participants (basic demographics, clinical features, available predictors), including the number of participants with missing data for predictors and outcome.	12, T1
	13c	V	For validation, show a comparison with the development data of the distribution of important variables (demographics, predictors and outcome).	T1
Model development	14a	D	Specify the number of participants and outcome events in each analysis.	12, T1
	14b	D	If done, report the unadjusted association between each candidate predictor and outcome.	n/a
Model specification	15a	D	Present the full prediction model to allow predictions for individuals (i.e., all regression coefficients, and model intercept or baseline survival at a given time point).	-
	15b	D	Explain how to the use the prediction model.	-
Model performance	16	D;V	Report performance measures (with CIs) for the prediction model.	15, T2, 16, 17, T3, 18
Model-updating	17	V	If done, report the results from any model updating (i.e., model specification, model performance).	n/a
Discussion				
Limitations	18	D;V	Discuss any limitations of the study (such as nonrepresentative sample, few events per predictor, missing data).	19
Interpretation	19a	V	For validation, discuss the results with reference to performance in the development data, and any other validation data.	19
	19b	D;V	Give an overall interpretation of the results, considering objectives, limitations, results from similar studies, and other relevant evidence.	20, 21
Implications	20	D;V	Discuss the potential clinical use of the model and implications for future research.	20
Other information				
Supplementary information	21	D;V	Provide information about the availability of supplementary resources, such as study protocol, Web calculator, and data sets.	Referenced throughout
Funding	22	D;V	Give the source of funding and the role of the funders for the present study.	21

Supplementary table 4 – TRIPOD Checklist: Prediction Model Development and Validation. T: Table, ST: supplementary table

Supplementary table 5 - Classifier scores per fold using leave-one-hospital-out cross-validation. CLF: Classifier, AUC: Area under the curve, TN: True negative, FP: False positive, FN: False negative, TP: True positive, PPV: Positive predictive value, NPV: Negative predictive value, LR: Logistic Regression, XGB: XGBoost, PM: Premorbid, CP: Clinical presentation, L&R: Laboratory and Radiology.

CLF	Feature set	Fold	AUC	TN	FP	FN	TP	Sensitivity	Specificity	PPV	NPV
LR	PM	0	0.779	106	39	9	15	0.625	0.731	0.278	0.922
		1	0.764	145	74	21	77	0.786	0.662	0.510	0.873
		2	0.694	169	42	28	22	0.440	0.801	0.344	0.858
		3	0.701	164	158	26	92	0.780	0.509	0.368	0.863
		4	0.894	79	26	0	24	1.000	0.752	0.480	1.000
		5	0.793	229	86	22	64	0.744	0.727	0.427	0.912
		6	0.854	68	29	1	15	0.938	0.701	0.341	0.986
		7	0.701	97	9	6	6	0.500	0.915	0.400	0.942
		8	0.727	144	93	25	63	0.716	0.608	0.404	0.852
LR	CP	0	0.638	70	75	8	16	0.667	0.483	0.176	0.897
		1	0.625	172	47	63	35	0.357	0.785	0.427	0.732
		2	0.714	106	105	12	38	0.760	0.502	0.266	0.898
		3	0.765	237	85	40	78	0.661	0.736	0.479	0.856
		4	0.694	69	36	11	13	0.542	0.657	0.265	0.863
		5	0.689	212	103	32	54	0.628	0.673	0.344	0.869
		6	0.698	61	36	4	12	0.750	0.629	0.250	0.938
		7	0.516	60	46	7	5	0.417	0.566	0.098	0.896
		8	0.660	156	81	35	53	0.602	0.658	0.396	0.817
LR	L&R	0	0.554	94	51	13	11	0.458	0.648	0.177	0.879
		1	0.714	71	148	7	91	0.929	0.324	0.381	0.910
		2	0.705	140	71	17	33	0.660	0.664	0.317	0.892
		3	0.686	228	94	51	67	0.568	0.708	0.416	0.817
		4	0.617	3	102	3	21	0.875	0.029	0.171	0.500
		5	0.759	212	103	24	62	0.721	0.673	0.376	0.898
		6	0.806	67	30	3	13	0.813	0.691	0.302	0.957
		7	0.657	12	94	2	10	0.833	0.113	0.096	0.857
		8	0.434	237	0	88	0	0.000	1.000	0.000	0.729
LR	PM + CP	0	0.779	98	47	6	18	0.750	0.676	0.277	0.942
		1	0.777	137	82	21	77	0.786	0.626	0.484	0.867
		2	0.745	153	58	19	31	0.620	0.725	0.348	0.890
		3	0.795	209	113	22	96	0.814	0.649	0.459	0.905
		4	0.871	75	30	4	20	0.833	0.714	0.400	0.949
		5	0.806	251	64	37	49	0.570	0.797	0.434	0.872
		6	0.894	67	30	3	13	0.813	0.691	0.302	0.957

Model	Features	#									
		7	0.678	90	16	7	5	0.417	0.849	0.238	0.928
		8	0.781	152	85	19	69	0.784	0.641	0.448	0.889
LR	All	0	0.621	96	49	13	11	0.458	0.662	0.183	0.881
		1	0.749	147	72	29	69	0.704	0.671	0.489	0.835
		2	0.726	124	87	10	40	0.800	0.588	0.315	0.925
		3	0.723	242	80	50	68	0.576	0.752	0.459	0.829
		4	0.702	52	53	4	20	0.833	0.495	0.274	0.929
		5	0.770	256	59	35	51	0.593	0.813	0.464	0.880
		6	0.827	61	36	3	13	0.813	0.629	0.265	0.953
		7	0.568	89	17	7	5	0.417	0.840	0.227	0.927
		8	0.741	208	29	51	37	0.420	0.878	0.561	0.803
LR	10 best	0	0.770	88	57	5	19	0.792	0.607	0.250	0.946
		1	0.797	140	79	17	81	0.827	0.639	0.506	0.892
		2	0.750	164	47	19	31	0.620	0.777	0.397	0.896
		3	0.787	197	125	17	101	0.856	0.612	0.447	0.921
		4	0.874	76	29	2	22	0.917	0.724	0.431	0.974
		5	0.825	249	66	27	59	0.686	0.790	0.472	0.902
		6	0.944	70	27	1	15	0.938	0.722	0.357	0.986
		7	0.778	95	11	6	6	0.500	0.896	0.353	0.941
		8	0.768	152	85	21	67	0.761	0.641	0.441	0.879
XGB	PM	0	0.736	116	29	12	12	0.500	0.800	0.293	0.906
		1	0.740	164	55	42	56	0.571	0.749	0.505	0.796
		2	0.672	0	211	0	50	1.000	0.000	0.192	0.000
		3	0.722	210	112	44	74	0.627	0.652	0.398	0.827
		4	0.902	84	21	4	20	0.833	0.800	0.488	0.955
		5	0.785	0	315	0	86	1.000	0.000	0.214	0.000
		6	0.806	74	23	7	9	0.563	0.763	0.281	0.914
		7	0.810	100	6	7	5	0.417	0.943	0.455	0.935
		8	0.731	169	68	37	51	0.580	0.713	0.429	0.820
XGB	CP	0	0.710	74	71	3	21	0.875	0.510	0.228	0.961
		1	0.735	158	61	31	67	0.684	0.721	0.523	0.836
		2	0.784	117	94	8	42	0.840	0.555	0.309	0.936
		3	0.738	207	115	30	88	0.746	0.643	0.433	0.873
		4	0.721	67	38	9	15	0.625	0.638	0.283	0.882
		5	0.734	241	74	40	46	0.535	0.765	0.383	0.858
		6	0.742	65	32	5	11	0.688	0.670	0.256	0.929
		7	0.694	75	31	6	6	0.500	0.708	0.162	0.926
		8	0.680	132	105	23	65	0.739	0.557	0.382	0.852
XGB	L&R	0	0.723	81	64	6	18	0.750	0.559	0.220	0.931
		1	0.719	129	90	28	70	0.714	0.589	0.438	0.822
		2	0.754	109	102	9	41	0.820	0.517	0.287	0.924
		3	0.691	213	109	45	73	0.619	0.661	0.401	0.826

	4	0.705	66	39	7	17	0.708	0.629	0.304	0.904
	5	0.751	196	119	23	63	0.733	0.622	0.346	0.895
	6	0.823	64	33	4	12	0.750	0.660	0.267	0.941
	7	0.787	86	20	5	7	0.583	0.811	0.259	0.945
	8	0.504	138	99	51	37	0.420	0.582	0.272	0.730
XGB PM + CP	**0**	0.771	84	61	5	19	0.792	0.579	0.238	0.944
	1	0.810	152	67	25	73	0.745	0.694	0.521	0.859
	2	0.774	144	67	16	34	0.680	0.682	0.337	0.900
	3	0.768	204	118	26	92	0.780	0.634	0.438	0.887
	4	0.867	0	105	0	24	1.000	0.000	0.186	0.000
	5	0.831	264	51	29	57	0.663	0.838	0.528	0.901
	6	0.868	70	27	2	14	0.875	0.722	0.341	0.972
	7	0.794	90	16	6	6	0.500	0.849	0.273	0.938
	8	0.767	140	97	18	70	0.795	0.591	0.419	0.886
XGB All	**0**	0.791	106	39	6	18	0.750	0.731	0.316	0.946
	1	0.823	68	151	0	98	1.000	0.311	0.394	1.000
	2	0.779	197	14	29	21	0.420	0.934	0.600	0.872
	3	0.775	227	95	42	76	0.644	0.705	0.444	0.844
	4	0.863	86	19	7	17	0.708	0.819	0.472	0.925
	5	0.832	273	42	37	49	0.570	0.867	0.538	0.881
	6	0.932	82	15	2	14	0.875	0.845	0.483	0.976
	7	0.820	100	6	7	5	0.417	0.943	0.455	0.935
	8	0.786	188	49	38	50	0.568	0.793	0.505	0.832
XGB 10 best	**0**	0.801	107	38	7	17	0.708	0.738	0.309	0.939
	1	0.806	66	153	2	96	0.980	0.301	0.386	0.971
	2	0.762	178	33	24	26	0.520	0.844	0.441	0.881
	3	0.786	223	99	35	83	0.703	0.693	0.456	0.864
	4	0.841	80	25	7	17	0.708	0.762	0.405	0.920
	5	0.820	271	44	38	48	0.558	0.860	0.522	0.877
	6	0.940	81	16	3	13	0.813	0.835	0.448	0.964
	7	0.847	101	5	7	5	0.417	0.953	0.500	0.935
	8	0.781	175	62	31	57	0.648	0.738	0.479	0.850

Classifiers	Feature set	AUC	Sensitivity	Specificity	PPV	NPV
LR	Premorbid	0.76 (0.75-0.77)	0.75 (0.73-0.78)	0.67 (0.65-0.70)	0.40 (0.38-0.42)	0.90 (0.90-0.91)
	Clinical Presentation	0.68 (0.65-0.71)	0.59 (0.50-0.68)	0.67 (0.60-0.74)	0.34 (0.30-0.38)	0.86 (0.85-0.87)
	Laboratory and Radiology	0.67 (0.66-0.69)	0.59 (0.56-0.61)	0.67 (0.64-0.71)	0.34 (0.32-0.36)	0.85 (0.84-0.86)
	Premorbid + Clinical Presentation	0.78 (0.77-0.79)	0.73 (0.66-0.79)	0.72 (0.68-0.76)	0.42 (0.39-0.46)	0.90 (0.89-0.92)
	All	0.59 (0.55-0.64)	0.29 (0.14-0.44)	**0.83 (0.75-0.92)**	0.35 (0.31-0.38)	0.80 (0.77-0.83)
	10 best	**0.81 (0.80-0.82)**	**0.79 (0.77-0.80)**	0.71 (0.69-0.73)	**0.44 (0.42-0.47)**	**0.92 (0.91-0.93)**
XGB	Premorbid	0.77 (0.76-0.79)	0.78 (0.75-0.81)	0.68 (0.66-0.70)	0.39 (0.37-0.42)	0.68 (0.44-0.92)
	Clinical Presentation	0.73 (0.72-0.74)	0.69 (0.67-0.72)	0.66 (0.64-0.68)	0.37 (0.36-0.39)	0.89 (0.87-0.92)
	Laboratory and Radiology	0.73 (0.71-0.74)	0.70 (0.67-0.72)	0.63 (0.60-0.66)	0.35 (0.33-0.38)	0.88 (0.84-0.92)
	Premorbid + Clinical Presentation	0.81 (0.80-0.82)	0.77 (0.75-0.79)	0.71 (0.70-0.73)	0.45 (0.43-0.47)	0.81 (0.62-1.00)
	All	**0.83 (0.81-0.84)**	**0.78 (0.75-0.80)**	**0.74 (0.72-0.77)**	**0.47 (0.45-0.49)**	0.91 (0.88-0.95)
	10 best	0.81 (0.80-0.82)	0.75 (0.72-0.77)	0.74 (0.71-0.76)	0.46 (0.43-0.49)	**0.91 (0.88-0.94)**

Supplementary table 6: Performance on internal validation. Performance is evaluated by using 10-fold random subsampling cross-validation. For each metric, the best performance per classifier is highlighted by bold text. LR performed best on all metrics except specificity when trained on the 10 selected features. XGB performed highest using all features on all metrics except negative predictive value. LR: Logistics regression, XGB: Extreme gradient boosting, AUC: Area under de curve, PPV: Positive predictive value, NPV: Negative predictive value


Supplementary Figure 1 – TRIPOD Checklist: Prediction Model Development and Validation. T: Table, ST: supplementary table

!! WARNING !!
This tool is NOT VALIDATED and should ONLY be used for research purposes!

|		
Age		years
Number of medications		count
History of Chronic Cardiac disease (not hypertension)		No=0 | Yes=1
Blood pH		pH
Blood Albumin		g/L
Urea Nitrogen		mmol/L
Lactate Dehydrogenase		mmol/L
Oxygen saturation		%
Oxygen saturation measured on		Room air=0 | Oxygen therapy=1

Get prediction

Supplementary Figure 2 – Screenshot of the calculator
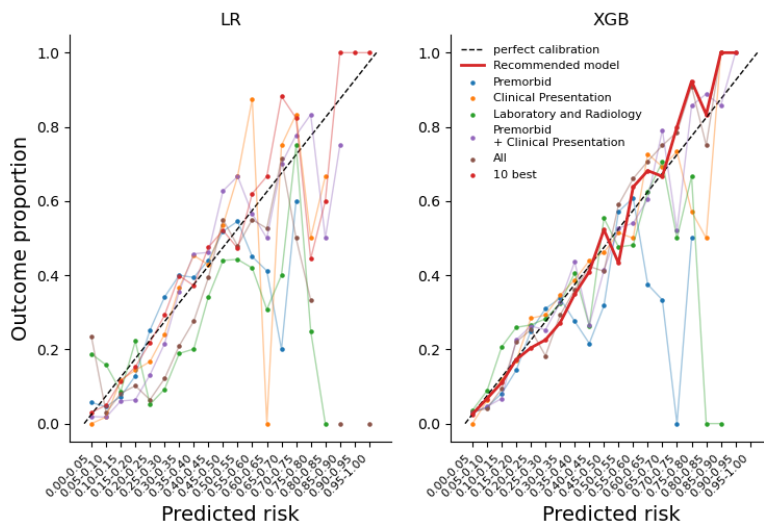
Supplementary Figure 3 – Model calibration. The recommended model, XGB trained on the 10 best features, is highlighted, and shows good calibration for all risk groups.
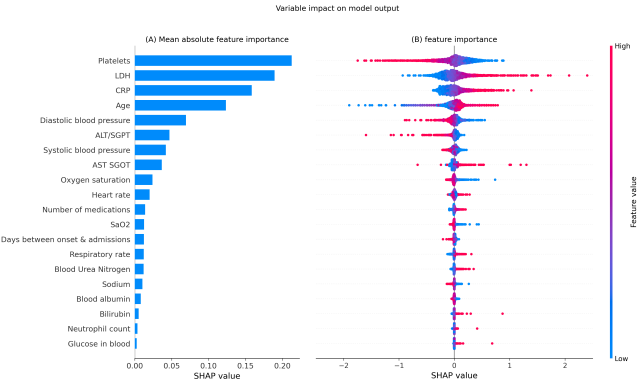
Supplementary Figure 4 – SHAP values for logistic regression
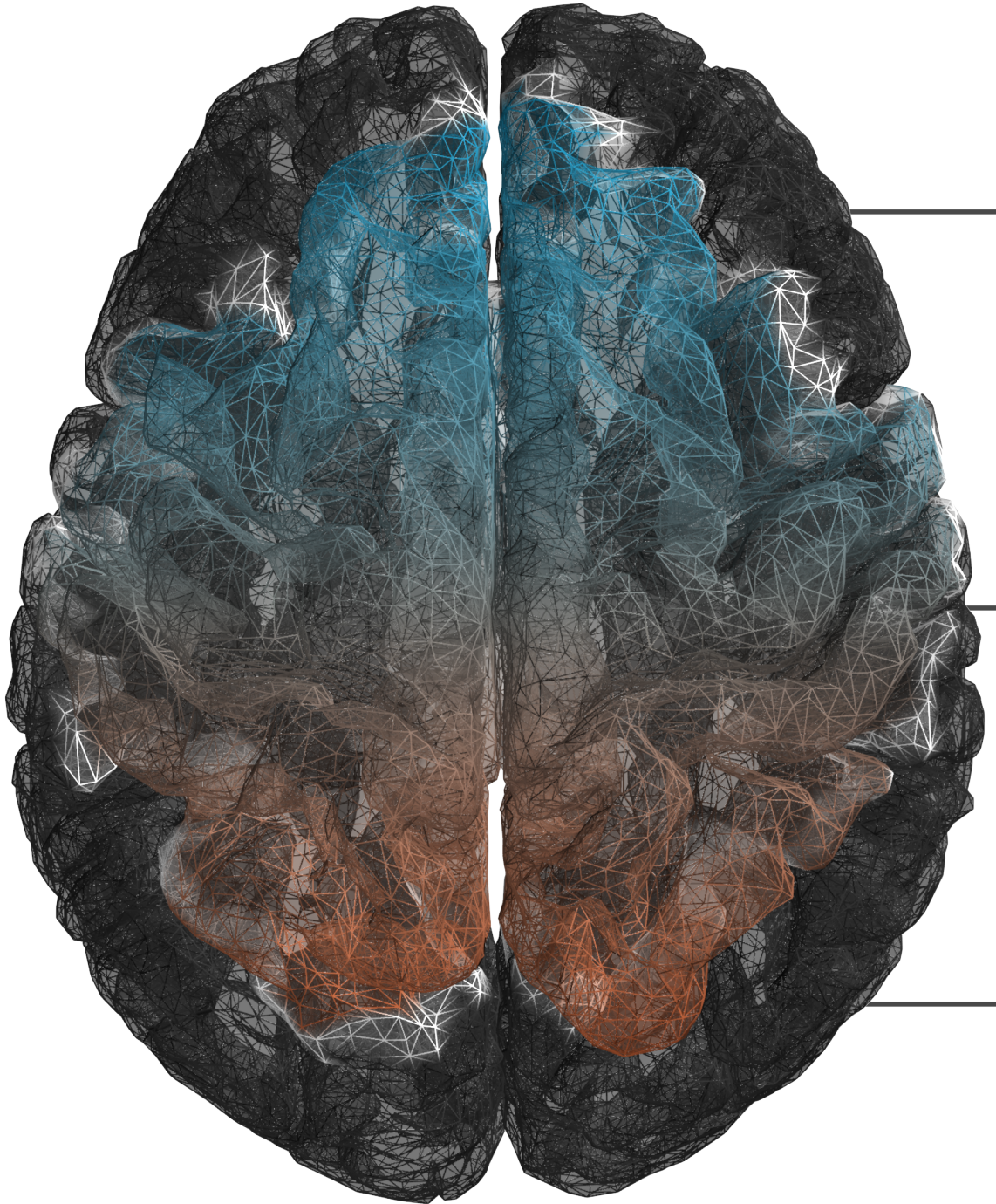
8
Discussion

This thesis presents a progressive exploration of decoding motor related activity using stereotactic-encephalography electrodes (sEEG). Throughout the chapters, a few core topics recur on the various aspects of decoding brain-wide motor representations with sEEG. Here, I will first expand on sEEG as a research vehicle. Then, I will evaluate our findings on motor-related neural activity and discuss potential representations. Furthermore, I will discuss the use of neural manifolds in sEEG and end with future implications on sEEG motor brain-computer interfaces.

8.1 Stereotactic encephalography as a research vehicle

Many types of recording modalities are available to record neural activity, all of which have different temporal and spatial resolutions. Ideally, the recording modality has a high spatial and temporal resolution, and records the whole brain simultaneously. Unfortunately, such a recording modality does not exists. In general, there is a trade-off between higher resolution and the size of the area covered by the electrodes. For example, hemodynamic methods may cover the whole brain, e.g. functional magnetic resonance imaging (fMRI), but are inherently limited in tem-

poral resolution by the hemodynamic response. Non-invasive methods recording electrical activity of the brain, like surface electroencephalography (EEG), cover the whole brain with high temporal resolution, but are limited in spatial resolution and frequency range: gamma and higher frequencies are strongly attenuated when passing through the skull and do not spread as far due to the $1/f$ decrease in power when the frequency increases. On the other side of the spectrum are the single or multi-unit electrodes (e.g. microelectrode arrays, MEAs or microwires), which are capable of recording individual spikes with very high spatial and temporal resolution. However, MEAs usually only cover a 4 x 4 mm area per array.

In the middle of this spectrum exist sEEG and electrocorticography (ECoG). ECoG grids capture local field potentials (LFPs) directly from the cortex. These grids capture neural activity from cortical areas with high spatial and temporal resolution, covering roughly 10mm^2. SEEG electrode have the unique property to capture from cortical and subcortical areas simultaneously. The spatial resolution is similar to ECoG, aggregating about 10.000 neurons in the recorded LFPs per electrode. Both recording methods are close enough to the neural sources to have access to high-frequency components as well. Lastly, sEEG electrodes are very similar to deep brain stimulation electrodes which boast safe and stable long-term implantations. Although there are no reports of long-term implantations of sEEG electrodes, in the context of BCIs, a similar safety profile in sEEG would be a welcome property compared to the instability of MEAs [1].

Together, these properties make sEEG an excellent research vehicle to explore global and previously hard to reach brain areas. In the context of BCIs, reports on decoding neural data using sEEG date back only to 2011 [2], highlighting the potential for new neuroscientific endeavors. For example, the sEEG coverage allow new studies to decode memory, decision-making [3] or navigation [4] processes in humans, as areas like the hippocampus, cingulate cortex and insula are regularly captured by sEEG implantations (Figure 1.3). Moreover, the broad coverage of sEEG electrodes enable large-scale network investigations that include interaction effects, as opposed to single area decoding. For example, chap-

ter 4 leverages the large-scale coverage of sEEG to describe global motor dynamics.

As sEEG electrodes penetrate deep into the brain, they inevitably cover many white matter areas as well. Contacts in white matter areas are generally assumed to hold little relevant information, and are thus often used as reference electrode. However, some reports [5, 6] and our internal analyses indicate that decodable information exists in these white matter contacts: removing these areas led to a decrease in decoding performance. However, there is no consensus whether this information originates from nearby grey matter areas [7] or from sources within white matter. For example, speculative sources may be 'leaked' activity from nodes of Ranvier or electrical activity from glia [8]. Unfortunately, sEEG lacks the precision to disentangle such small-scale sources. Moreover, the imaging strategy used in thesis to localize the brain area a contact is in also does not provide sufficient information to draw any conclusions from white matter areas. The imaging pipeline co-registers an pre-op magnetic resonance imaging (MRI) scan with a post-op computed tomography (CT) scan, and labels the anatomical location of each contact based on the Destrieux atlas [9]. This imagining pipeline provides detailed information about many grey matter areas, but does not provide detailed white matter labels, except for which hemisphere it resides in. White matter labels can be provided by other tools like diffusion tensor imaging (DTI) [10], but these require specialized MRI sequences that are not part of clinical epilepsy treatment. Including DTI scans would provide an important extra level of detail in sEEG research, as it would enable BCI studies to related activity patterns to white matter tracts. Without it, these type of studies cannot be conducted, and thus including DTI scans may be valuable to consider in future studies or treatments.

Although the brain-wide coverage of sEEG provides new opportunities, the varying electrode configurations per implantation poses new challenges for analyses. As sEEG implantations are part of the clinical treatment of medication-resistant epilepsy patients, the implantation locations are solely determined by clinical necessity. Coverage of the same region across participants is thus inconsistent, which makes systematic comparisons of the same area between participants challeng-

ing. Some areas are covered more regularly, like the superior temporal gyrus or hippocampus, but most other areas are not. Moreover, large structures can have the same anatomical label, meaning that the same label may not always indicate exactly the same area. For example, contacts in the hippocampus are labeled as `right-hippocampus` or `left-hippocampus`, which may be anywhere between the anterior and posterior edge. As already noted in the discussion of chapter 2, there are too few data to identify systematically involved areas. This led to the application of dimensionality reduction methods (Chapter 3, 4 and 5) to extract relevant information from all the electrodes. These methods will be further discussed in section 8.3.

In spite of the challenges, the sparse but global coverage of sEEG electrodes that includes cortical and subcortical structures simultaneously is a unique strength of this recording modality, making it well suited for within person and large-scale electrophysiological decoding approaches. From within this context, this thesis has provided new insight on brain-wide motor representations.

8.2 Motor representations throughout the brain

We uncovered global neural dynamics from distributed areas in chapter 4 and we were able to decode non-directional 3D hand-kinematics from distributed areas in chapter 5. In both studies, no particular area appeared to be the main driver of performance, except for the sporadic coverage of the motor cortex (particularly in chapter 5, Figure 5.3a). Correlations were widespread, although differences exists between areas. This is in line with literature [11], builds upon reports of brain-wide correlations between movement and spiking activity in mice [12–15], and expands to brain-wide correlations in humans.

It is an open question what these global motor correlations represent. So far, it seems like these correlations are related to any movement, both instructed and non-instructed [14, 16], and represent something non-directional. The widespread negative correlations with alpha-beta power and positive correlations with broadband high-gamma power observed in chapter 5, Figure 5.3b & c may indicate that these are related

to change of movement. Given the close relationship between acceleration and force, there might be a relationship between these correlations and the (estimated) force of movement. A few studies have reported successful decoding of force from sEEG [17, 18] or ECoG [19]. Branco et al. [20] report that a transient high-gamma response is strongly coupled with onset and offset of a grasp force tasks. A similar increase of high-gamma at onset is observed in Murphy et al. (2016) [18]. Although S1 and M1 were involved, Branco et al. report significant responses outside of the sensorimotor cortex, including supplementary motor cortex, posterior parietal cortex, cingulate motor areas and the premotor cortex.

In the context of goal-directed movement, alpha-beta desynchronization may reflect a change in global motor dynamics that enables the motor system to become active. An increase of high-gamma power at onset may then reflect an initial estimate of the required force, acceleration or effort to reach a goal, leading to the hypothesis that the size of the high-gamma peak is correlated with the distance to a goal. The global contributions of this high-gamma peak might then be involved in providing information to make this estimation. If this is the case, then integration centers like the supramarginal gyrus (SMG) should be involved. To this end, the strongest contributions of the first principal components seen in chapter 3, Figure 3.3 are clustered around the SMG, and Breault et al. (2019) [21] report that average power in the SMG positively correlated with the path length.

The decoder in chapter 5 was not able to decode any directional component from any kinematic. Other studies [22–24] do report significant decoding of directional movement components from non-motor areas, seemingly contradicting the results from chapter 5. The commonality between these studies is that they all use the classic center-out task. The decoder selected features based on the summed correlation with all kinematics, so it might be that correlations of specific directional components were too weak compared to the other kinematics, and thus not selected by the decoder. However, the discrepancy might be better explained by the fact that highly controlled experimental designs do not necessarily translate to designs that are more naturalistic. A weaker signal may be uncovered by averaging trials, but remain obscured in single

trial paradigms. This discrepancy highlights that decoders that continuously decode neural signals are essential for clinical applications that capture the full complexity of the motor system. Future research projects should therefore transition from highly controlled experiments to continuous and naturalistic designs.

Overall, the relatively recent availability of large-scale electrophysiological recordings has generated new questions about global motor related activity and its representations. To answer these questions, we may need to develop and/or apply new tools to gain new insights [25]. The methods used in chapter 4 use manifold learning approaches to uncover the underlying dynamics of global motor-related neural activity. These tools are gaining traction as they result in stable representations combined from many different electrodes. Multiple approaches exist to extract these hidden structures, which can be exploited by motor decoders.

8.3 Manifold learning as a tool to describe and decode movement

Recording data from brain-wide areas inevitably means that the sEEG electrodes capture many ongoing neural processes. However, only a subset of neural activity is relevant for the targeted behavior, while the other neural activity is irrelevant to the behavior or noise. Each contact contains a combination of behaviorally relevant neural activity, behaviorally irrelevant neural activity and noise, in different ratios. To disentangle the behaviorally relevant information from the rest, dimensionality reduction techniques can be applied to extract a low-dimensional representation of the behaviorally relevant information. The benefit of these methods is that they increase the signal-to-noise ratio, as well as reduce the dimensionality of the data. Principal component analysis is a well-known example, which extract principal components that are a linear combination of all contacts. Therefore, a single principal component captures behaviorally relevant activity from multiple sources and in essence describes a relationship between the contributing sources.

These relationships of neural activity are often called neural population dynamics or a neural manifold, and are effective methods to de-

code movement for BCIs [26–29]. In our work, we explicitly extracted these relationships by calculating the covariance matrices of the low-dimensional representation. Using the regularized sample covariance matrices for each trial in a class, we calculated the geometric class mean covariance matrix. In other words, we extracted the stereotypical dynamics per class. This resulted in a stable representation, which was similar enough between tasks and participant to cross decode significantly above chance.

Stability is an important property as new methods aim to apply manifolds to retain degrading BCI performance over time [29]. On a single or multi-neuron scale, the brain constantly changes: neurons migrate within the cortex, cells are dying and regenerating and the tuning of firing rates of single neurons can change over time. The neural signal is affected by tiredness as well as day-to-day variations. However, learned skills and behaviors remain remarkably stable over time. Perhaps this stability is ensured by retaining the relationships between groups of neurons, or in other words, the covariance structure. This has the potential to be an effective method, as the ablation study in chapter 4 showed barely any degradation in performance for up to 50% of signal loss at the optimal number of dimensions. Another example of stable relationships is the directional tuning in the motor cortex (as discussed in the introduction). While the underlying tuning constantly changes, the population vector remains stable in a preferred direction. Indeed, preserved covariance structures have been identified multiple times in multiple regions as well [30–33]. Natraj et al. (2021) [34] extends this to multiple scales. The neural covariance between multiple areas within a distributed network remained stable during all movements, whereas more specific movements within this manifold exhibit more specific covariance structures as well. The large-scale multi-area manifold described in Natraj et al. (2021) seems similar to the global motor dynamics described in chapter 4. The importance of stability of the neural dynamics is demonstrated by Sadtler et al. (2014) [35]. The authors learned the intrinsic manifold of a monkey by mapping neural activity into factors, which then mapped to cursor control in a center-out task. When the authors perturbed the mapping from factors to cursor output (within man-

ifold), the subject was able to adjust within sessions. On the other hand, an outside manifold perturbation, that is a perturbation of the mapping from the neural activity to the factors (i.e. a change of dynamics), took the subjects days to adjust to. The outside manifold perturbation forced the subject to adjust the neural dynamics, which, given its stability, are hard to change. Taken together, stability generated by persistent covariance structures may be a globally applied mechanism on multiple scales to ensure stable behavior over time.

So far, it seems like a few characteristics are related to neural manifolds in motor representations. First, on a large scale, there exists stable covariance structures that can change based on global brain state [30], for example from move to not-move (Chapter 4). Secondly, covariance structures arise at multiple scales, describing more fine-grained movements [30], e.g. general movement to grasping movement to specific hand movements [34]. Lastly, similar covariance structures capture similar movements [31, 34]. Regardless whether manifolds describe a function of the brain or not, they are a useful mathematical tool to describe complex neural networks and its communication. In light of the clinical BCI perspective, it may not be essential to entirely understand the underlying representation first, given a sufficiently reliable output is provided. For example, in chapter 5 we applied a preferential subspace identification algorithm [36] to separate neural activity into a parameterized number of behaviorally relevant and irrelevant information, and used these to continuously decode 3D hand kinematics. Although we have not identified what the latent states represent, it does show that sufficient information exists to consistently decode hand movement speed and acceleration.

Some considerations remain. First, the studies presented in this work and the studies referred to above all use linear algorithms to learn a manifold. Linear approaches are easier to apply and interpret, but it is unknown whether the underlying relationship is best described linearly or non-linearly. Few efforts have been presented to fit non-linear manifolds, e.g. by using recurrent neural networks [37–39]. An elegant approach is presented by Perkins et al. (2023) [40], where they choose from a library of predefined neural trajectories, resulting in fast and interpreta-

ble non-linear decoding with known constraints. Secondly, the optimal number of dimensions is unknown and may vary depending on the context of electrode configuration and decoding task. From this perspective, selecting the number of latent states is an optimization problem. In chapter 4, we determined that 10 dimensions was the most stable in an ablation study. However, we also observed that including more dimensions did increase decoder performance. Given the decoding goal, in this case stability or performance, the choice of parameter changes. When reporting the 'optimal' number of dimensions, the context should be taken into account. Moreover, complex modelling or decoding strategies are not necessarily better than simpler ones [40, 41].

In sum, the manifold learning field provides tools that may be exceptionally useful for the large-scale and varying sEEG recordings. They provide stable information on relationships between areas and motor-representations that can be used in neural decoders.

8.4 Translating sEEG to clinical applications.

SEEG-based BCI research is still relatively young, but has already proven to be a promising tool for exciting applications [42]. However, to capture the full complexity of motor control, sEEG motor BCI research should move to naturalistic closed-loop studies as soon as possible. Closing the loop will provide tangible feedback to both the user and researcher whether a signal or decoder is sufficiently powerful to provide a reliable output. For specific areas or between participant studies, other electrodes might provide better resolution to answer the scientific question. For example, exploring white matter activity would need single or multi-neuron recordings to disentangle potential sources. Moreover, sEEG provides opportunities to uncover important processes that may sufficiently support clinical BCIs that would justify additional implantations. However, sEEG electrodes are not implanted in the target population for BCI, increasing uncertainty whether the same processes can be decoded in the target population. If electrodes were implanted in the target population, the road from first decoding results to clinical implantation is still deceptively long. When looking at the speech decoding field, we see that

although astonishing performance has recently been demonstrated [43, 44], even then the road to end users is long [45]. Furthermore, it is not only a scientific and engineering challenge. Legislation, financial and neuroethical aspects, like device obsolescence, are challenges the field needs to overcome as well.

In spite of the current and future challenges, sEEG based neural decoding holds many undiscovered opportunities. The global coverage provides access to previously hard to reach areas, while at the same time calls for new approaches to understand the large-scale neural dynamics. Altogether, sEEG motor BCI research has the potential to lead to exciting new neuroscientific discoveries and improved BCI applications.

References

[1] Samuel C. Colachis et al. "Long-term intracortical microelectrode array performance in a human: a 5 year retrospective analysis". en. In: *Journal of Neural Engineering* 18.4 (Aug. 2021). Publisher: IOP Publishing, p. 0460d7. DOI: 10.1088/1741-2552/ac1add.

[2] Dean J. Krusienski and Jerry J. Shih. "Control of a Visual Keyboard Using an Electrocorticographic Brain–Computer Interface". In: (2011).

[3] Laura Marras et al. *Decoding Arbitrary and Informed Decisions from Intracranial Recordings in Humans*. en. Pages: 2023.06.01.543070 Section: New Results. June 2023. DOI: 10.1101/2023.06.01.543070.

[4] Jeremy Saal et al. "Towards hippocampal navigation for brain–computer interfaces". en. In: *Scientific Reports* 13.1 (Aug. 2023). Number: 1 Publisher: Nature Publishing Group, p. 14021. DOI: 10.1038/s41598-023-40282-7.

[5] Manuel R Mercier et al. "Evaluation of cortical local field potential diffusion in stereotactic electro-encephalography recordings: A glimpse on white matter signal". In: *NeuroImage* 147 (2017). Publisher: Elsevier, pp. 219–232. DOI: 10.1016/j.neuroimage.2016.08.037.

[6] Chad Bouton et al. "Decoding Neural Activity in Sulcal and White Matter Areas of the Brain to Accurately Predict Individual Finger Movement and Tactile Stimuli of the Human Hand". In: *Frontiers in Neuroscience* 15 (2021).

[7] Meredith J. McCarty et al. "The Listening Zone of Human Electrocorticographic Field Potential Recordings". en. In: *eNeuro* 9.2 (Mar. 2022). Publisher: Society for Neuroscience Section: Research Article: Methods/New Tools. DOI: 10.1523/ENEURO.0492-21.2022.

[8] Ana L. G. Mestre et al. "Extracellular Electrophysiological Measurements of Cooperative Signals in Astrocytes Populations". In: *Frontiers in Neural Circuits* 11 (2017).

[9] Christophe Destrieux et al. "Automatic parcellation of human cortical gyri and sulci using standard anatomical nomenclature". eng. In: *NeuroImage* 53.1 (Oct. 2010), pp. 1–15. DOI: 10.1016/j.neuroimage.2010.06.010.

[10]   Lauren J. O'Donnell and Carl-Fredrik Westin. "An introduction to diffusion tensor image analysis". In: *Neurosurgery clinics of North America* 22.2 (Apr. 2011), pp. 185–viii. DOI: `10.10 16/j.nec.2010.12.004`.

[11]   Ziyue Aiden Wang et al. *Not everything, not everywhere, not all at once: a study of brain-wide encoding of movement*. en. Pages: 2023.06.08.544257 Section: New Results. June 2023. DOI: `10.1101/2023.06.08.544257`.

[12]   International Brain Lab et al. *A Brain-Wide Map of Neural Activity during Complex Behaviour*. en. Pages: 2023.07.04.547681 Section: New Results. July 2023. DOI: `10.1101/2023.07.0 4.547681`.

[13]   Nicholas A. Steinmetz et al. "Distributed coding of choice, action and engagement across the mouse brain". en. In: *Nature* 576.7786 (Dec. 2019). Number: 7786 Publisher: Nature Publishing Group, pp. 266–273. DOI: `10.1038/s41586-019-1787-x`.

[14]   Carsen Stringer et al. "Spontaneous Behaviors Drive Multidimensional, Brain-wide Activity". In: *Science* 364.6437 (Apr. 2019), p. 255. DOI: `10.1126/science.aav7893`.

[15]   Peter Zatka-Haas et al. "Sensory coding and the causal impact of mouse cortex in a visual decision". In: *eLife* 10 (July 2021). Ed. by Martin Vinck, Joshua I Gold, and Karel Svoboda. Publisher: eLife Sciences Publications, Ltd, e63163. DOI: `10.7554/eLife.63163`.

[16]   Edward Zagha et al. "The Importance of Accounting for Movement When Relating Neuronal Activity to Sensory and Cognitive Processes". en. In: *Journal of Neuroscience* 42.8 (Feb. 2022). Publisher: Society for Neuroscience Section: TechSights, pp. 1375–1382. DOI: `10.1 523/JNEUROSCI.1919-21.2021`.

[17]   Xiaolong Wu et al. "Decoding Continuous Kinetic Information of Grasp from Stereo-electroencephalographic (SEEG) Recordings". en. In: *Journal of Neural Engineering* (2022). DOI: `10.1088/1741-2552/ac65b1`.

[18]   Brian A. Murphy et al. "Contributions of subsurface cortical modulations to discrimination of executed and imagined grasp forces through stereoelectroencephalography". In: *PLoS ONE* 11.3 (2016), pp. 1–21. DOI: `10.1371/journal.pone.0150359`.

[19]   Robert D. Flint et al. "Extracting kinetic information from human motor cortical signals". eng. In: *NeuroImage* 101 (Nov. 2014), pp. 695–703. DOI: `10.1016/j.neuroimage.2014 .07.049`.

[20]   Mariana P. Branco et al. "High-frequency band temporal dynamics in response to a grasp force task". eng. In: *Journal of Neural Engineering* 16.5 (Aug. 2019), p. 056009. DOI: `10.1088 /1741-2552/ab3189`.

[21]   MacAuley Smith Breault et al. "Non-motor Brain Regions in Non-dominant Hemisphere Are Influential in Decoding Movement Speed". In: *Frontiers in Neuroscience* 13.JUL (July 2019), pp. 1–13. DOI: `10.3389/fnins.2019.00715`.

[22]   Seyyed Moosa Hosseini and Vahid Shalchyan. "Continuous Decoding of Hand Movement From EEG Signals Using Phase-Based Connectivity Features". In: *Frontiers in Human Neuroscience* 16 (2022).

[23]   Aysegul Gunduz et al. "Differential roles of high gamma and local motor potentials for movement preparation and execution". In: *Brain-Computer Interfaces* 3.2 (Apr. 2016). Publisher: Taylor & Francis _eprint: https://doi.org/10.1080/2326263X.2016.1179087, pp. 88–102. DOI: `10.1080/2326263X.2016.1179087`.

[24] Etienne Combrisson et al. *Local field potentials in human motor and non-motor brain areas encode the direction of upcoming movements: An intracerebral EEG classification study*. en. Pages: 2023.09.07.556727 Section: New Results. Sept. 2023. DOI: 10.1101/2023.09.07.556727.

[25] Anne E. Urai et al. "Large-scale neural recordings call for new insights to link brain and behavior". en. In: *Nature Neuroscience* 25.1 (Jan. 2022). Number: 1 Publisher: Nature Publishing Group, pp. 11–19. DOI: 10.1038/s41593-021-00980-9.

[26] Mark M. Churchland et al. "Neural population dynamics during reaching". en. In: *Nature* 487.7405 (July 2012). Bandiera_abtest: a Cg_type: Nature Research Journals Number: 7405 Primary_atype: Research Publisher: Nature Publishing Group Subject_term: Motor cortex;Neuronal physiology;Population dynamics Subject_term_id: motor-cortex;neuronal-physiology;population-dynamics, pp. 51–56. DOI: 10.1038/nature11129.

[27] Juan A. Gallego et al. "Neural Manifolds for the Control of Movement". en. In: *Neuron* 94.5 (June 2017), pp. 978–984. DOI: 10.1016/j.neuron.2017.05.025.

[28] Cecilia Gallego-Carracedo et al. "Local field potentials reflect cortical population dynamics in a region-specific and frequency-dependent manner". In: *eLife* 11 (Aug. 2022). Ed. by Srdjan Ostojic and Ronald L Calabrese. Publisher: eLife Sciences Publications, Ltd, e73155. DOI: 10.7554/eLife.73155.

[29] Brianna M. Karpowicz et al. *Stabilizing brain-computer interfaces through alignment of latent dynamics*. en. Pages: 2022.04.06.487388 Section: New Results. Nov. 2022. DOI: 10.1101/2022.04.06.487388.

[30] Juan A. Gallego et al. "Cortical population activity within a preserved neural manifold underlies multiple motor behaviors". en. In: *Nature Communications* 9.1 (Oct. 2018). Number: 1 Publisher: Nature Publishing Group, p. 4233. DOI: 10.1038/s41467-018-06560-z.

[31] Mostafa Safaie et al. *Preserved neural population dynamics across animals performing similar behaviour*. en. Pages: 2022.09.26.509498 Section: New Results. Sept. 2022. DOI: 10.1101/2022.09.26.509498.

[32] Svenja Melbaum et al. "Conserved structures of neural activity in sensorimotor cortex of freely moving rats allow cross-subject decoding". en. In: *Nature Communications* 13.1 (Dec. 2022). Number: 1 Publisher: Nature Publishing Group, p. 7420. DOI: 10.1038/s41467-022-35115-6.

[33] Shreya Saxena et al. "Motor cortex activity across movement speeds is predicted by network-level strategies for generating muscle activity". In: *eLife* 11 (May 2022). Ed. by J Andrew Pruszynski and Joshua I Gold. Publisher: eLife Sciences Publications, Ltd, e67620. DOI: 10.7554/eLife.67620.

[34] Nikhilesh Natraj et al. "Compartmentalized dynamics within a common multi-area mesoscale manifold represent a repertoire of human hand movements". en. In: *Neuron* (Oct. 2021). DOI: 10.1016/j.neuron.2021.10.002.

[35] Patrick T. Sadtler et al. "Neural constraints on learning". en. In: *Nature* 512.7515 (Aug. 2014). Number: 7515 Publisher: Nature Publishing Group, pp. 423–426. DOI: 10.1038/nature13665.

[36] Omid G. Sani et al. "Modeling behaviorally relevant neural dynamics enabled by preferential subspace identification". en. In: *Nature Neuroscience* 24.1 (Jan. 2021). Number: 1 Publisher: Nature Publishing Group, pp. 140–149. DOI: 10.1038/s41593-020-00733-0.

[37]   Cátia Fortunato et al. *Nonlinear manifolds underlie neural population activity during behaviour*. en. Pages: 2023.07.18.549575 Section: New Results. July 2023. DOI: `10.1101/2023.07.18.549575`.

[38]   Omid G. Sani, Bijan Pesaran, and Maryam M. Shanechi. *Where is all the nonlinearity: flexible nonlinear modeling of behaviorally relevant neural dynamics using recurrent neural networks*. en. Pages: 2021.09.03.458628 Section: New Results. Sept. 2021. DOI: `10.1101/2021.09.03.458628`.

[39]   Steffen Schneider, Jin Hwa Lee, and Mackenzie Weygandt Mathis. "Learnable latent embeddings for joint behavioural and neural analysis". en. In: *Nature* 617.7960 (May 2023). Number: 7960 Publisher: Nature Publishing Group, pp. 360–368. DOI: `10.1038/s41586-023-06031-6`.

[40]   Sean M. Perkins et al. *Simple decoding of behavior from a complicated neural manifold*. en. Pages: 2023.04.05.535396 Section: New Results. Apr. 2023. DOI: `10.1101/2023.04.05.535396`.

[41]   Matthew S. Willsey et al. "Real-time brain-machine interface in non-human primates achieves high-velocity prosthetic finger movements using a shallow feedforward neural network decoder". en. In: *Nature Communications* 13.1 (Nov. 2022). Number: 1 Publisher: Nature Publishing Group, p. 6899. DOI: `10.1038/s41467-022-34452-w`.

[42]   Miguel Angrick et al. "Real-time synthesis of imagined speech processes from minimally invasive recordings of neural activity". en. In: *Communications Biology* 4.1 (Sept. 2021). Bandiera_abtest: a Cc_license_type: cc_by Cg_type: Nature Research Journals Number: 1 Primary_atype: Research Publisher: Nature Publishing Group Subject_term: Brain-machine interface;Neural decoding Subject_term_id: brain-machine-interface;neural-decoding, pp. 1–10. DOI: `10.1038/s42003-021-02578-0`.

[43]   Francis R. Willett et al. "A high-performance speech neuroprosthesis". en. In: *Nature* (Aug. 2023). Publisher: Nature Publishing Group, pp. 1–6. DOI: `10.1038/s41586-023-06377-x`.

[44]   Sean L. Metzger et al. "A high-performance neuroprosthesis for speech decoding and avatar control". en. In: *Nature* (Aug. 2023). Publisher: Nature Publishing Group, pp. 1–10. DOI: `10.1038/s41586-023-06443-4`.

[45]   Nick F. Ramsey and Nathan E. Crone. "Brain implants that enable speech pass performance milestones". en. In: *Nature* 620.7976 (Aug. 2023). Bandiera_abtest: a Cg_type: News And Views Number: 7976 Publisher: Nature Publishing Group Subject_term: Neuroscience, Medical research, Engineering, pp. 954–955. DOI: `10.1038/d41586-023-02546-0`.
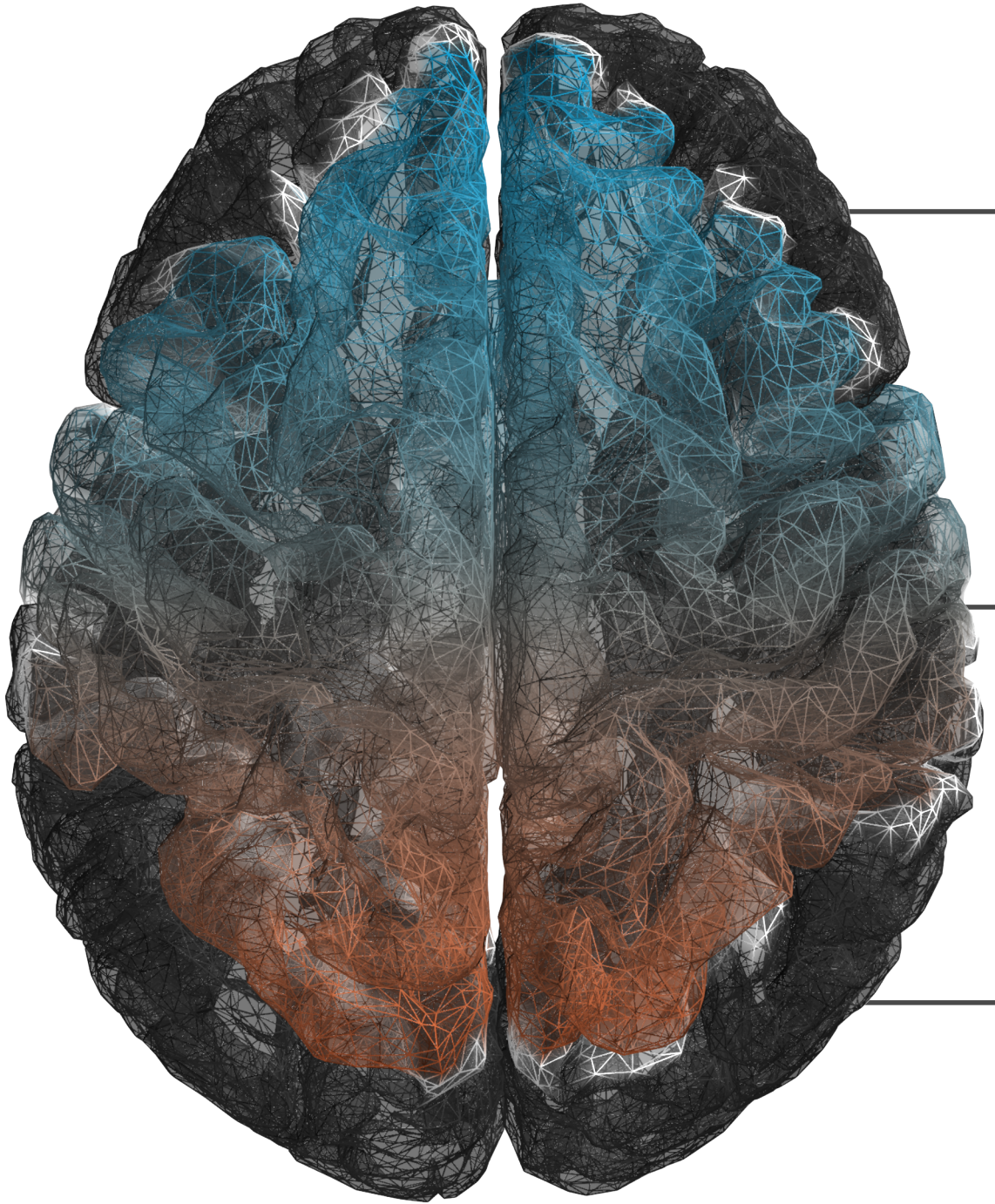
Impact

Movement is ubiquitous in life, and the results presented in chapter 2, 3, 4 & 5 suggest that movement-related neural activity is ubiquitous in the brain as well. Identifying the extent, understanding the neural basis, and decoding these global motor dynamics may lead to both scientific and societal impact.

Most immediate, we strengthen the scientific support to look beyond the motor cortex [1]. A broader perspective of motor decodable information may lead to a more comprehensive understanding of the full motor system. In the context of BCIs, this may uncover new implantation targets, increasing the available information for motor decoders. Moreover, motor-related activity can be decoded outside of the motor-cortex, making motor-BCIs available for users who have a damaged motor cortex. In an ideal future, neuroprostheses integrate seamlessly, perform real-time and decode (near) perfectly. To achieve this, all brain areas that contain motor-related information essential for decoding need to be captured. This set of areas is currently unknown, but given the narrow focus on the motor cortex, there might be unidentified (networks of) regions that improve motor decoders. A broader focus and decoding endeavors may uncover these areas.

A potential application of decoding non-motor areas is that global motor dynamics (chapter 4) may be beneficial for stabilizing decoders. One of the current problems experienced in motor decoders based on microelectrode arrays (MEA) is a decrease in performance over time, requiring regular calibration sessions. Stabilizing the decoder would reduce calibration sessions, increasing the potential for long-term at home use. From a manifold perspective, the reduction in performance can be viewed as a degradation of the underlying manifold due to changing signal in the electrodes [2]. Given the stability of the global motor dynamics to loss of signal (stable up to 50% of lost channels, as demonstrated in chapter 4, Figure 4.3), they might act like a stable anchor to retain more performance. Increasing long-term stability by decreasing

(re)calibration of decoders would increase the likelihood of clinical deployment of at home use of BCIs

That same stability may contribute to calibrationless decoders via a different pathway as well. We demonstrated a proof-of-concept of transfer learning with non-overlapping electrodes, which may be beneficial to improve or reduce calibration of training of decoders. If we are able to extract neural structures that are similar between users, then we may be able to pre-train models based on earlier recorded data. This way, a decoder may be used as a plug-and-play device. Given that the decoding performance was more reliant on the data or electrode locations of the target participant, no pre-selection or optimization is required for initializing a decoder for a new user.

So far, motor BCIs in this thesis have been discussed in the context of controlling some kind of assistive device. However, the same motor decoding methods might prove useful for other purposes. For example, changes in global motor dynamics may relate to symptom severity or disease progression in motor neuron diseases. Particularly in treatments where electrodes are implanted already for another clinical goal, like deep brain stimulation (DBS) in Parkinson's disease (PD), research to relate changes in global motor dynamics to clinical measures can be performed directly. Additionally, if changes in dynamics are related to symptom severity, then this change might be used as control signal to adaptive DBS.

Given the number of DBS implantations, 30.000 between 2002 and 2011 in the United States [3], the possible impact of new potential clinical measures like global motor dynamics can be widespread. Moreover, DBS treatments are expanding from PD to more neurological disorders and syndromes, including Tourette syndrome, pain, major depression and obsessive compulsive disorder [4], expanding the potential research potential and clinical impact even further.

References

[1] Juan A. Gallego, Tamar R. Makin, and Samuel D. McDougle. "Going beyond primary motor cortex to improve brain–computer interfaces". English. In: *Trends in Neurosciences* 45.3 (Mar. 2022). Publisher: Elsevier, pp. 176–183. DOI: 10.1016/j.tins.2021.12.006.

[2]   Brianna M. Karpowicz et al. *Stabilizing brain-computer interfaces through alignment of latent dynamics*. en. Pages: 2022.04.06.487388 Section: New Results. Nov. 2022. DOI: 10.1101/2 022.04.06.487388.

[3]   Brett E. Youngerman et al. "A decade of emerging indications: deep brain stimulation in the United States". In: *Journal of Neurosurgery* 125.2 (Aug. 2016). Publisher: American Association of Neurological Surgeons Section: Journal of Neurosurgery, pp. 461–471. DOI: 10.3 171/2015.7.JNS142599.

[4]   Andres M. Lozano et al. "Deep brain stimulation: current challenges and future directions". In: *Nature Reviews Neurology* 15.3 (2019). Publisher: Springer US, pp. 148–160. DOI: 10.103 8/s41582-018-0128-2.
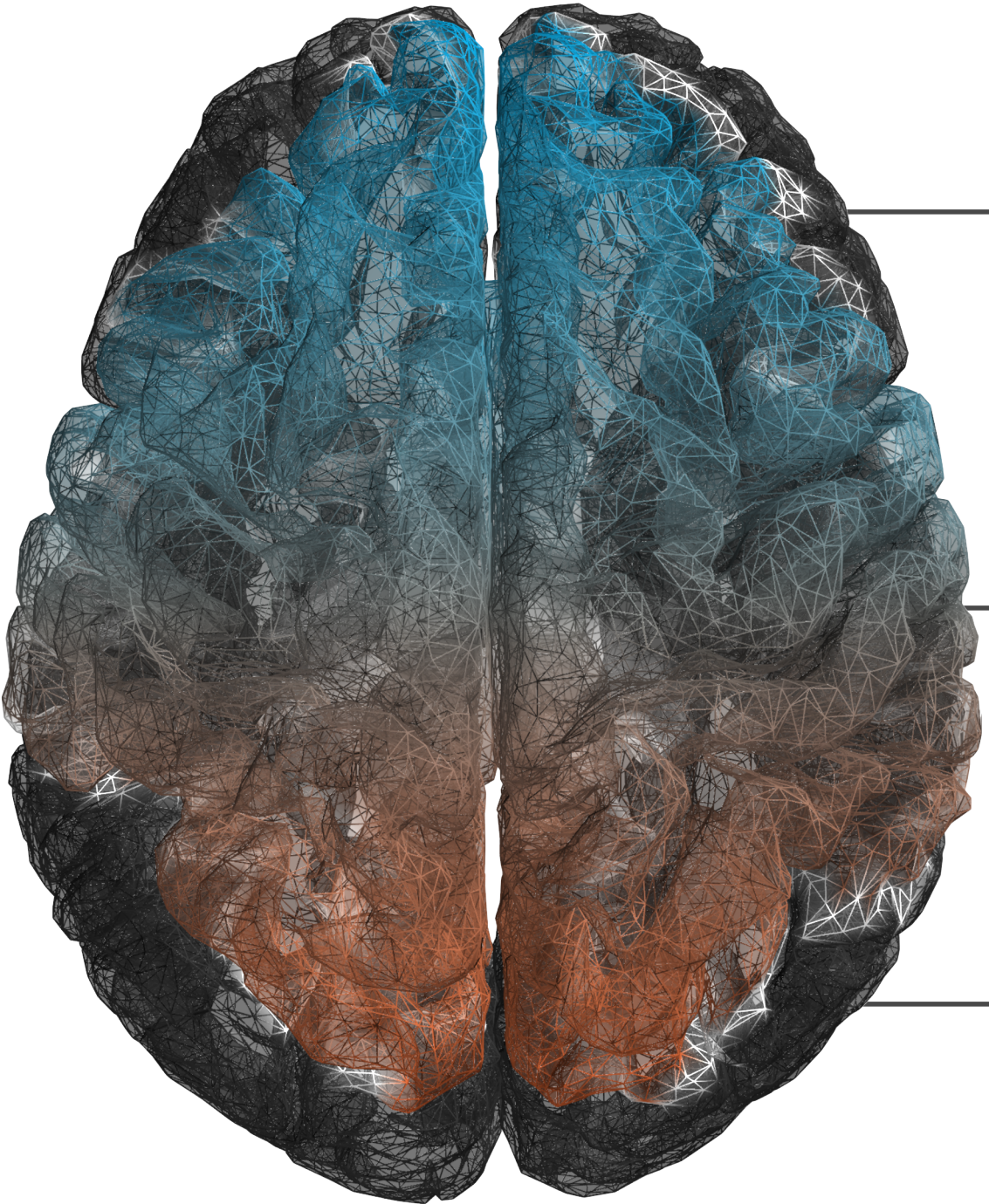
Summary

Nearly every choice you make eventually leads to a movement. You have to move to act on your decision, otherwise your decision will have little effect. Unfortunately, for some people movement is or becomes a challenge. Severe paralysis or progressive motor disease may increasingly limit a person's ability to interact and communicate with their surroundings. One of the most natural ways to increase an individual's independence and ability to move and communicate may be brain-computer interfaces (BCIs). A BCI records neural activity and translates it into a control signal for an assistive device. Many options exist to restore movement, such as motorized wheelchairs, mouse pointers for click-and-select and robotic arms or neural prostheses to restore reach and grasp function.

BCIs consists of two main components. First, neural data need to be recorded at one or more brain areas that contain motor related neural activity. Secondly, a neural decoder needs to translate the high-dimensional neural activity into a control signal. To achieve the first part, many BCIs use data recorded from the motor cortex: an area demonstrated to contain sufficient information to control robotic arms. However, recent discoveries in brain-wide recordings reveal that motor-related neural activity is correlated with movement throughout the brain, expanding from the local area of the motor cortex. These brain-wide signals provide new opportunities for motor decoders to reveal the neural content and improve decoding performance.

The works in this thesis investigate the neural content of these brain-wide activations by decoding movement from them. In chapter 2, we provide an initial demonstration that three classes (rest, left hand movement and right hand movement) can be decoded continuously from most electrode configurations. This led to two insights: first, the brain-wide coverage of stereotactic-electroencephalography (sEEG) electrodes captures sufficient information to predict movement in a continuous paradigm, meaning a prediction could be made 10 times per second.

This property is essential for future clinical applications because it allows for real-time control. Secondly, the performance was significantly above chance for almost all electrode configurations, meaning that movement related neural activity may be present in many different areas.

To further investigate these brain-wide motor related activities, in chapter 3 and 4 we explored the neural dynamics of a low-dimensional representation of global motor-related neural activity. By extracting the neural dynamics from a low dimensional representation of the motor-related neural activity, we were able to decode movement regardless of electrode placement. We named these pervasive dynamics 'global motor dynamics' and demonstrate that these were similar across tasks and across participants, even with non-overlapping electrodes configurations. Specifically, by training our decoder on executed movement, we were able to decode imagined movement. Similarly, by training our decoder on one participant, we were on average able to decode movement, based on the neural activity of another participant. Altogether, the results indicate that global motor dynamics are a brain-wide phenomenon and exhibits stable behavior.

We built on these results by expanding our discrete task to a more complex movement task. In chapter 5, we developed a decoder that aimed to decode continuous 3D hand kinematics from sEEG recordings. To do so, we designed a gamified experiment where the participant had to control a cursor and move it to a target within a 3D space. By using the preferential subspace identification algorithm, we were able to reconstruct non-directional hand movement speed and acceleration using delta activity, alpha-beta power and high-gamma power. As with the global motor dynamics in chapter 4, the decoder was able to decode hand speed trajectories significantly above chance for all participants.

Throughout this work and my PhD, we have recorded many datasets with many participants. To perform these experiments, we had to perform many manual actions and checks to start recordings. This resulted in long setup times and many errors, ultimately reducing the time spent on recording and the total amount of recorded data. To reduce this problem, we developed a recording platform called T-Rex (Chapter 6) that

automates setup and recording. T-Rex is designed to be flexible and is currently in use in three different hospitals with different recording environments. Overall, the implementation of T-Rex greatly reduced the number of errors and setup time, and increased the amount of data recorded.

To conclude, we demonstrate that global motor dynamics can be recorded throughout the brain, that these dynamics are similar between tasks and participants with non-overlapping electrodes, and contain enough information to decode non-directional hand kinematics. We highlight that sEEG provides a unique opportunity to explore the largely untapped potential of high spatial and temporal resolution recordings of brain-wide motor-related neural activity.

Finally, during this PhD, the COVID-19 pandemic spread around the world and impacted our lives as well. During this time, our hospital was on the verge of having insufficient beds to admit all COVID-19 patients. The intensive care unit from the hospital voiced the need for a clinical decision support system that could provide more information in a 'code black' situation: the moment where the clinician needs to choose between patients because there are insufficient beds. Therefore, I diverted my attention and resources to develop a model (chapter 7) that could predict the 21-day all-cause mortality of admitted patients based on admission data. The model outperformed controversial age-based rules. Fortunately, the clinical decision support system never needed to be applied in practice.
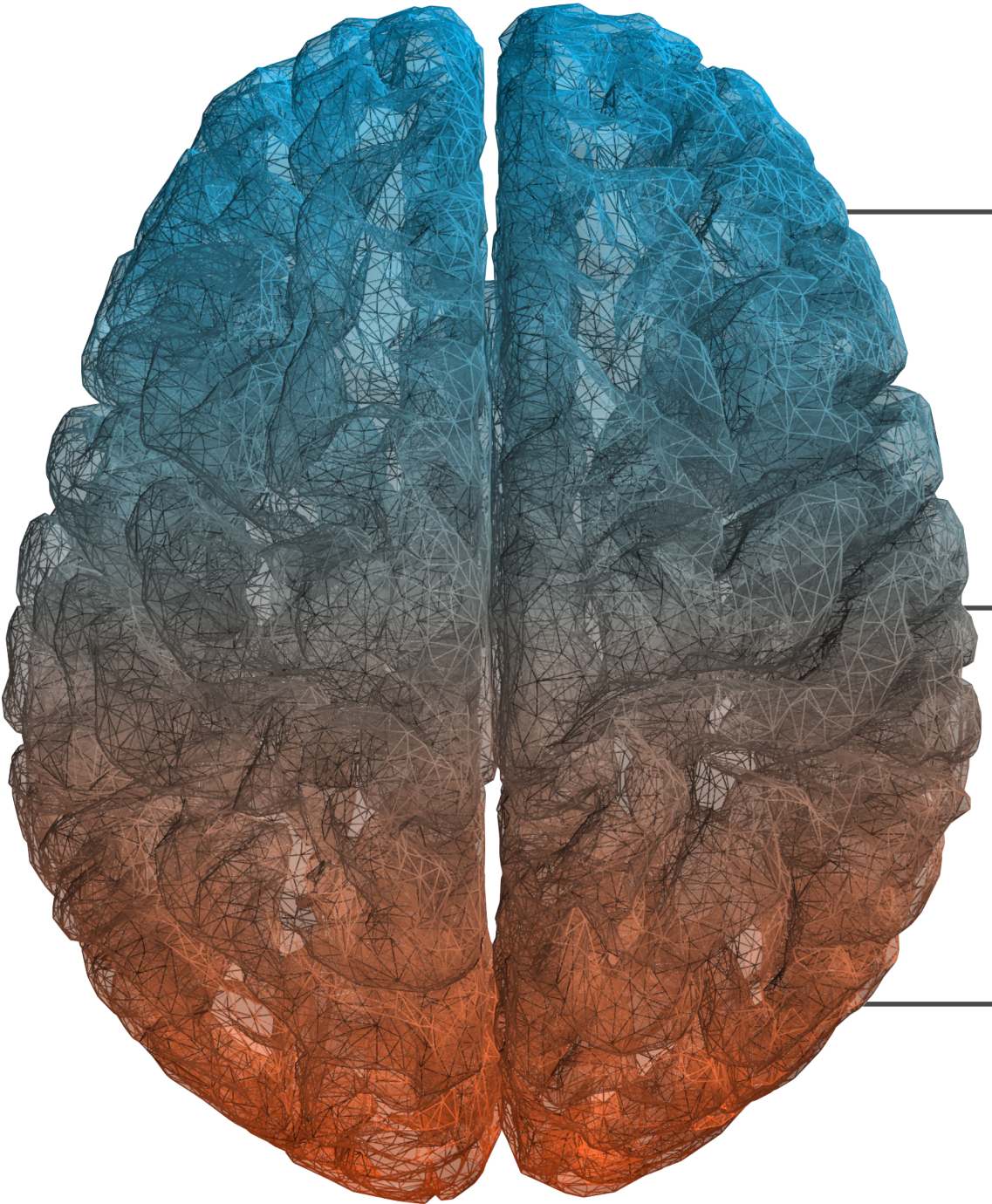
Appendix

Dutch Summary

Curriculum Vitae

Published Work

Acknowledgements

Samenvatting

Vrijwel elke keuze die je maakt zal uiteindelijk leiden tot een beweging. Om ervoor te zorgen dat jouw beslissing iets veranderd in jouw omgeving is het onvermijdelijk dat je een beweging moet maken. Voor de meeste mensen gebeurt dit moeiteloos en onbewust, maar voor sommige mensen is bewegen niet vanzelfsprekend. Een ernstige verlamming of progressieve motorische aandoening kan het bewegen ernstig beperken. Het raakt de functionele onafhankelijkheid van de persoon, waardoor diegene steeds meer zorg van zijn/haar omgeving nodig heeft. Het verbeteren van de functionele onafhankelijkheid is een van de belangrijkste aandachtspunten. Een van de meest natuurlijke manieren van controle van een hulpmiddel, zoals een robotarm, rolstoel of computercursor, zou gerealiseerd kunnen worden door middel van een Brain-computer interface (BCI). Deze technologie meet en vertaald hersensignalen direct naar een controle signaal waarmee het hulpmiddel wordt aangestuurd.

Om een BCI te ontwikkelen zijn er twee hoofdcomponenten van belang. Allereerst moeten het systeem hersensignalen kunnen meten in een of meerdere hersengebieden die activiteit bevatten met informatie over een (beoogde) beweging. Als tweede is er een model nodig dat deze zogenoemde motor-gerelateerde hersenactiviteit vertaald naar een controle signaal om het hulpmiddel aan te sturen. Voor de eerste component is er historisch gezien veel aandacht besteed aan de motor cortex, een hersengebied ongeveer tussen je oren dat genoeg informatie bevat voor de huidige BCI prototypes om een robotarm aan te sturen. Echter, recente ontdekkingen wijzen er op dat motor-gerelateerde hersenactiviteit door de hele hersenen gemeten kan worden. Het uitbreiden van de aandacht van de motor cortex naar de hele hersenen biedt nieuwe kansen, zoals betere modellen die ons meer kunnen vertellen over de informatie in deze motor-gerelateerde hersenactiviteit en een verbetering van de vertaling van motor-gerelateerde hersenactiviteit naar beweging.

De studies in deze thesis onderzoeken of en hoe we de hersenbreed gemeten motor-gerelateerde activiteit met machine learning modellen

kunnen vertalen naar beweging. In hoofdstuk 2 demonsteren we dat we drie verschillende staten, geen beweging, linkerhand beweging en rechterhand beweging, elke 100 milliseconden kunnen herleiden van de data van de meeste combinaties van geïmplanteerde elektrodes. Hieruit herleidde we twee inzichten: Ten eerste vangen de stereotactische elektro-encefalografische (sEEG) elektrodes in de meeste gevallen genoeg informatie om bewegingen continue te kunnen herleiden. Voor een toekomstig klinische toepassing is dit een essentiële voorwaarde. Ten tweede lukte het model om van bijna alle combinaties van sEEG elektrodes significant beter dan kans te voorspellen welke beweging de proefpersoon (niet) maakte. Dit betekend dat motor-gerelateerde hersenactiviteit in vele verschillende hersengebieden te meten is.

Om deze hersenbrede motor-gerelateerde activiteit verder te onderzoeken hebben we in hoofdstuk 3 en 4 gekeken naar de onderliggende patronen. Door deze patronen te identificeren en de veranderingen van deze patronen te analyseren konden we voorspellen of de deelnemer wel of niet bewoog, onafhankelijk van waar de elektrodes geplaatst waren. Dit patroon hebben we 'Global Motor Dynamics' genoemd, oftewel de dynamiek van motor-gerelateerde hersenactiviteit door de hele hersenen gemeten. In hoofdstuk 4 laten we zien dat Global Motor Dynamics vergelijkbaar zijn tussen verschillende taken (ingebeelde en uitgevoerde bewegingen) en verschillende proefpersonen, zelfs als de locaties van de geïmplanteerde elektrodes niet overeenkomen. Specifiek betekent dat dat we a.d.h.v. de hersenactiviteit van proefpersoon A kunnen voorspellen of proefpersoon B wel of niet bewoog. Samengenomen laten de resultaten zien dat Global Motor Dynamics een patroon is dat door de hele hersenen aanwezig lijkt te zijn en dat het stabiele voorspellende patronen behelst.

Voortbouwend op deze resultaten waren we geïnteresseerd of we ook een complexere bewegingstaak konden voorspellen. In hoofdstuk 5 hebben we een model gemaakt dat kinematica van drie dimensionale handbewegingen kan reconstrueren op basis van sEEG metingen. Voor dit onderzoek hebben we een speciaal spelletje ontwikkeld waarbij de deelnemers een cursor moest verplaatsen in een kleine 3D ruimte. Door gebruik van het 'preferential subspace algoritme' konden we de snelheid

en versnelling van de hand continu te voorspellen. Hiervoor gebruikte we delta, alpha-beta en high-gamma frequenties gemeten in de hersenactiviteit. Net als bij de resultaten van hoofdstuk 4 kon het model de handsnelheid en -versnelling significant boven kans voorspellen voor alle deelnemers aan ons onderzoek.

Tijdens de onderzoeken in deze thesis en van collega's zijn er vele verschillende data sets verzameld met verschillende experimenten. Om deze experimenten uit te voeren was het nodig om veel stappen handmatig uit te voeren en te controleren. Hierdoor was er grote kans op fouten en duurde het opzetten, starten en stoppen van experimenten lang, terwijl er maar een korte periode was dat we data konden verzamelen. Om de werklast en kans op fouten te verminderen hebben een meetsysteem ontwikkeld genaamd T-Rex (hoofdstuk 6), dat het grootste deel van het opzetten, starten en stoppen van experimenten automatiseert. T-Rex is ontworpen om flexibel te zijn, waardoor T-Rex al gebruikt wordt in drie medische centra met verschillende IT-infrastructuur. Tot dusver heeft de implementatie van T-Rex het aantal fouten aanzienlijk verminderd, evenals de tijd die we spenderen aan opstellen van de experimenten. Uiteindelijk heeft het gebruik van T-Rex ervoor gezorgd dat we meer data kunnen verzamelen.

Concluderend laat het werk in deze thesis zien dat Global Motor Dynamics gemeten kunnen worden door vrijwel de hele hersenen en dat dit patroon vergelijkbaar is tussen verschillende taken en personen, zelf als de elektrodes op verschillende plekken geïmplanteerd zijn. De dynamiek van de onderliggende patronen bevat genoeg informatie om de hand snelheid en versnelling op elk moment te voorspellen. Deze thesis onderstreept dat de hoge kwaliteit metingen met sEEG unieke kansen biedt om het potentieel te ontsluiten van hersenbreed gemeten motorgerelateerde activiteit.

Afsluitend, tijdens mijn promotietraject ging de wereld gebukt onder de COVID-19 pandemie met alle gevolgen van dien. Tijdens de eerste infectiegolven zat het ziekenhuis aan haar grens van het aantal beschikbare ziekenhuisbedden voor nieuwe COVID-19 patiënten. Vanuit de intensive care was er plotseling een grote vraag naar een ondersteunend systeem dat de beslissing bij een zogenoemde 'code zwart' kon verbeteren:

de situatie waarbij er niet genoeg bedden zijn en een keuze gemaakt moest worden tussen patiënten. Om mijn maatschappelijke steentje bij te dragen heb ik mijn aandacht en middelen ingezet om een model te ontwikkelen (hoofdstuk 7) dat de overleving kans over 21 dagen van nieuwe COVID-19 patiënten kon voorspellen, gebaseerd op data beschikbaar bij opname. Het ontwikkelde model voorspelde beter dan controversiële, maar door noodzaak gedwongen op leeftijd-gebaseerde regels gebruikt in enkele Europese ziekenhuizen. Uiteindelijk zijn we vooral blij dat dit ondersteuningssysteem in de praktijk nooit nodig is geweest.

Curriculum Vitae

Maarten Christiaan Ottenhoff was born in Eindhoven on august 3, 1994. He received his Athenaeum degree in July 2012 at the Lorentz Casimir Lyceum in Eindhoven. Following his passion in sports, he moved to Amsterdam to pursue a Bachelors degree in Human Movements Sciences at the Vrije Universiteit. After a theoretical bachelor project on the cause and effect of overtraining, and an experimental project on non-invasively recording action potentials on the spinal cord using high-density EMG-grids, he followed his newly found interest in a more technical direction and pursued a Master Artificial Intelligence at the Vrije Universiteit. During this time, Maarten discovered the field of Brain-computer interface. Using the opportunity of an open topic project during his masters, he attempted to build his first brain-computer interface with a commercial-grade non-invasive neural headset. During his Master Education, Maarten teached high-school students in Physics, Math and Biology for StudentPlus, and provided at-home technical support for Studentaanhuis.nl. Furthermore, he had a position as People Analytics engineer at Healthy Workers, a small start-up aiming to improve employee well-being. In his last year, he worked as data-scientist at Annual Insight, developing models to predict product prices at auctions and creating dashboard for healthcare suppliers.

After obtaining his Master degree in 2019, he started his PhD on motor brain-computer interfaces in the Neural interfacing lab at Maastricht University under supervision of Dr. Christian Herff, Dr. Pieter Kubben and Prof. Dr. Yasin Temel. During this PhD, he gained both theoretical and experimental knowledge on decoding movement using sEEG electrodes. During this 4.5 years of research, Maarten has presented at multiple international conferences, and visited the Neural Systems Engineering & Information Processing Lab at the University of Southern California, Los Angeles, led by Prof. Dr. Maryam Shanechi, during these 4 month visit he gained in-depth knowledge on dynamical models and manifold learning. Furthermore, his experimental work gained interest

from his peers, leading to an invitation at Charité Hospital, Berlin, to present and install his developed hand-tracking experiment. Aside from his scientific work, Maarten has written articles for the general public for NeurotechX and OpenBCI, and made an appearance on the scientific show Atlas on Dutch National Television. He also peer-reviewed multiple articles and supervised multiple Bachelors and Master students.

Currently, Maarten aims to pursue his scientific career by finding a post-doc where he can work with participants implanted for BCI research.

Published work

Published
2021

- **Ottenhof, M.C.**, Ramos, L.A., Potters, W. et al. on behalf of The Dutch COVID-PREDICT research group (2021) - Predicting mortality of individual patients with COVID-19: a multicentre Dutch cohort. BMJ Open.
  Published

- Aries M.J.H., van den Berg J.P., Beudel, M. ..., **Ottenhoff M.C.** et al. (2021) - Clinical course of COVID-19 in the Netherlands: an overview of 2607 patients in hospital during the first wave. Nederlands Tijdschrift voor de Geneeskunde.
  Published

- Angrick, M. **Ottenhoff, M.C.**, Diener, L. et al. (2021) - Real-time synthesis of imagined speech processes from minimally invasive recordings of neural activity. Nature Communications Biology.
  Published

- Angrick, M. **Ottenhoff, M.C.**, Goulis, S. et al. (2021) - Speech Synthesis from Stereotactic EEG using an Electrode Shaft Dependent Multi-Input Convolutional Neural Network Approach. Engineering in Medicine and Biology Conference.
  Published

- **Ottenhoff, M.C.**, Goulis, S., Wagner, L. et al. (2021) - Continuously Decoding Grasping Movements using Stereotactic Depth Electrodes. Engineering in Medicine and Biology Conference.
  Published

2022

- Angrick, M. **Ottenhoff, M.C.**, Diener, L. et al. (2022) - Towards Closed-Loop Speech Synthesis from Stereotactic EEG: A Unit Selection Approach. International Conference on Acoustics, Speech and Signal processing (ICASSP).
  Published

- Verwoert, M., **Ottenhoff, M.C.**, Goulis, S. et al. (2022) - Dataset of Speech Production in intracranial Electroencephalography. Scientific Data.
  Published

- Kohler, J. **Ottenhoff, M.C.**, Goulis, S. et al. (2022) - Synthesizing Speech from Intracranial Depth Electrodes using an Encoder-Decoder Framework. Neurons Behavior Data analysis and Theory.
  Published

2023

- Saal, J., **Ottenhoff, M.C.**, Kubben P. et al. (2023) - Towards hippocampal navigation for brain–computer interfaces. Scientific Reports.
  Published

- Amigó-Vega*, J., **Ottenhoff, M.C.**, Verwoert, M. et al. (2022) - T-Rex: sTandalone Recorder of EXperiments; An easy and versatile neural recording platform. JMIR Neurotechnology. **Both authors contributed equally.*
  Published

- **Ottenhoff, M.C.**, Verwoert, M., Goulis, S. et al. (2023) - Decoding executed and imagined grasping movements from distributed non-motor brain areas using a Riemannian decoder. Frontiers in Neuroscience.
  Published

Preprints

- Marras, L., Verwoert, M., **Ottenhoff, M.C.** et al. (2023) - Decoding Arbitrary and Informed Decisions from Intracranial Recordings in Humans. BioRxiv.
  Under review

- **Ottenhoff, M.C.**, Verwoert, M., Goulis, S. et al. (2023) - Global motor dynamics - Invariant neural representations of motor behavior in distributed brain-wide recordings. BioRxiv.
  Under review

Acknowledgments

Science thrives on collaboration, mentorship and support, and my own scientific path does so no less. Throughout these 4.5 years, I have had the privilege to work and meet many incredible people, and all the scientific conversations, ideas, and (non-)workplace banter has given me great joy and inspiration. Thus, I would like to take this opportunity to voice my appreciation via this non-comprehensive list of people that have contributed in one way or the other.

First and foremost, my supervisory team: **Prof. Dr. Yasin Temel, Dr. Pieter Kubben and Dr. Christian Herff**. **Yasin**, we spraken elkaar niet vaak, en dat is een goed goed teken! Dat betekend dat de supervisie op rolletjes liep. Tijdens onze eerste kennismaking heb je de vier fases van een PhD uiteengezet (ik was al gewaarschuwd door collega's). Een nuttige voorbereiding op het hele traject, want alle fases zijn inderdaad voorbij gekomen. **Pieter**, je enthousiasme, optimisme en doorpakkendheid is aanstekelijk. Grootste plannen waar anderen niet eens aan zouden beginnen pak jij met twee handen aan. Mailtje hier, belletje daar, formuliertje hier en het was gefixt. Het ondernemershap is inspirerend en verfrissend binnen de trage universiteit en in onze gesprekken kwam datzelfde terug. Alles wat nodig was kon geregeld worden. Je open blik op projecten, support en "can-do" mentaliteit waren enorm waardevol en leerzaam. **Christian**, every supervisor should have the drive and ability that you have to get the best out of your PhD students. You have given me confidence from my very first project and pushed me out of my comfort-zone. Not only have you taught me how to science, you also made sure to kick-start my career as a scientist. I greatly enjoyed your kind, patient and down-to-earth supervision and personality and also deeply appreciated your direct communication when work was below the expected standard (the appreciation came after 5 minutes of personal frustration of course). All in all, I can now say with confidence that you do not need a thick skin to work with you. I am absolutely sure we'll be working together again throughout our careers.

Maxime, je kritische blik en aandacht voor detail heeft menig project van goed naar beter gebracht. Precies waar ik niet zo goed in ben, details, kon jij eindeloos over doorgaan. Hoe vaak ik niet gefrustreerd ja zat te knikken als je weer eens kritiek had over iets (in mijn ogen) onbenulligs, diep van binnen wetende dat je wéér gelijk had. Van jouw scherpe oog voor detail heb ik veel geleerd! Ik bewonder je betrokkenheid en zorgzaamheid voor anderen, jij wil zeker weten dat het goed gaat met anderen. Het was een plezier om samen te werken, te klagen over werk en samen ons kantoor in het gareel te houden. **Joaquin**, I think we would have made excellent office buddies. Even though remote, it was a great pleasure to work together, especially on the technical stuff. Your perseverance in the whole Timeflux project is admirable and has benefited the lab immensely. But most importantly, it was great fun to nerd out on some new gadget or overly complicated note-taking system or strategy. I am glad I can still make you laugh with the fact that I can run really fast. I am sure that, one day, you will estimate the duration

of your project correctly. Let's celebrate together when it happens! **Jeroen**, van jouw vriendelijkheid en positiviteit kan de hele wereld nog wat leren. Als iedereen aan het klagen was over weet-ik-veel-wat, wist jij het weer vanuit de positieve andere kant te bekijken. De steun aan anderen en de rust in je doen-en-laten maken je een onzettend fijn mens om mee samen. Ik voelde me dan ook vereerd toen ik je me uitnodigde om op (werk)bezoek te komen in Berlijn. Ik heb genoten om je collega te zijn en samen op het (festival)terras te zitten. Ik weet zeker dat we elkaar nog vaak tegen zullen komen. **Margot**, we hebben elkaar ontmoet toen ik nog een kleine kangaroe en jij een kleine papegaai was in het Vondelpark in Amsterdam. Via jou heb ik deze PhD gevonden, dus ben jij een onmisbaar onderdeel van deze thesis! Je nuchtere kijk op eigenlijk alles was vaak broodnodig en ik verwonder me nog steeds over hoe jij altijd op de hoogte was van alles in de gangen van divisie drie.

One of the main reason to come to the office was to have fun with all my colleagues. To all my Neural Interfacing Lab colleagues throughout my phd, **Maria, Carlos, Daria, Berkhan, Jeremy, Laura, Sophia & Sophocles**, you have made my time so much more enjoyable. Even though we all have our own independent projects, science is teamwork and you have made it into the great team that we have right now. In the office, I regularly go the far-away sink to fill by bottle, just to have an excuse to peek into all the offices and see who is there. To all my hallway buddies: **Mathilde, Rick, Britt, Philippos, Renzo, Katherine, Chris** (Lunch?), **Dean, Glenn, Perla, Jackson, Rose, Lonne, Martijn, Jana**, you were an essential part of that. All the lunches, discussions, coffees (many!), conferences, real-life mario kart, festivals, vrimibo's (including the full vrimibo experience in one hour, **Rose**) and (christmas) parties would not be fun without you!

My USC friends, it was a great experience visiting your lab. My apologies to **Omid** who had to put up with my endless questions. The discussions, lunches and game nights were excellent. **Lucine**, I am still amazed by the spectacular waterfall we saw at the end of our walk. You made sure I had a soft landing during my arrival and your friendliness, care for others, focus and dedication still inspires me. **Christian** and **Nitin**, we should play some more games if we get the chance.

Paranimf **Thomas**, vlak nadat ik was begonnen in Maastricht, heb ik deze arme stakker en z'n vriendin onderdak geboden toen ze letterlijk dakloos waren. En nu zijn we vrienden. Shit... Maar goed, wel gelachen! Excuses voor iedereen die onze eindeloze gespreken over sport hebben moeten aanhoren. Voor werk al even laten weten dat er koffie gedronken moet worden, want we moeten even opscheppen over de training van de avond ervoor. En tussendoor even slap ouwehoeren over van alles en nog wat met een vocabulair dat voor 50 procent bestaat uit het repertoire van Ronald Goedemondt. Samen hardlopen, samen fietsen, samen van de ene naar de andere kant van Schotland, samen met Anouk en Marjet (kerst)borrels, samen met matrassen van de trap af en samen klagen over werk, het was altijd leuk, altijd gezellig. Zonder deze vriendschap had ik deze thesis nooit afgeschreven! Het was ontzettend fijn om bij jou en Anouk te landen toen Marjet en ik naar Maastricht verhuisde. Het heeft onze tijd zo veel leuker gemaakt.

Paranimf **Nick**, begonnen op de waterscouting (uh, ik bedoel zeilen) en later nog huisgenoten op de Nassaukade in Amsterdam. De vele avonturen die we daar hebben

meegemaakt zijn niet op de noemen. De uit de hand gelopen vrijdagmiddag borrels, huisavonden en festivals waren altijd legendarisch en zorgde voor de nodige ontspanning tijdens stressvolle tijden. Je enthousiasme, ambitie en betrokkenheid maken dat ik en anderen graag bij je in te buurt zijn. Maar het meest bewonder ik nog je gave om iedereen die je ooit gezien hebt, jaren later nog te herkennen! Samen zijn we ook onderdeel van **Hic vestibulum**, het onofficiële eerste dispuut van Heeze, de parel van Brabant! Samen met **Thijs, Driek, Michiel, Rens, Wouter & Sjors**, hebben we de nodige kroegen op z'n kop gezet. Over werk beginnen kon ik wel door de jaren heen, maar dan zag ik al snel glazige ogen ontstaan. En dat is maar goed ook :). Als ik vanuit Amsterdam of Maastricht terug naar Eindhoven ging om op pad te gaan met dit bij elkaar geraapte zooitje voelde het elke keer als thuiskomen en was het zonder uitzondering altijd een groot plezier. Helaas waren menige maandagen daardoor wel een stuk minder productief. Recentelijk nog ons 10-jarig jubileum gehad, nog minstens 10 te gaan!

De onvoorwaardelijke steun, rust en aanmoediging die ik van familie en vrienden door de jaren heb mogen ontvangen is onbetaalbaar. **Wim, Erica, Cathelijne, Stefan, Wilma, Theo, Daan, Ronald, Stefanie, Cato, Guus, Wout, Evelien, Wies, Jet**, zonder jullie zou ik niet zijn waar ik nu ben, en zou ik ook niet komen waar ik heen wil.

En als laatste natuurlijk **Marjet**, nu ik dit schrijf mijn verloofde, en als je dit leest mijn vrouw. *Achter elke academicus staat een sterke partner die heel erg haar best doet om niet verveelt te kijken.* Ik zie hoe je je best doet om te luisteren als ik weer een oeverloos betoog begin te mijmeren over een hersenkronkel van werk. Het maakt ook niet uit, ook al snap je het niet altijd, je begrijpt het wel altijd. Zonder die onvoorwaardelijke steun en je vertrouwen in mij, zou deze thesis hier nu niet liggen. Ik heb er geen woorden voor hoe dankbaar ik ben dat je ervoor zorgt dat ik kan doen wat ik wil doen. Ik kan niet wachten op wat we allemaal nog mee gaan maken. Ik hou van je.